

AD-A145 621

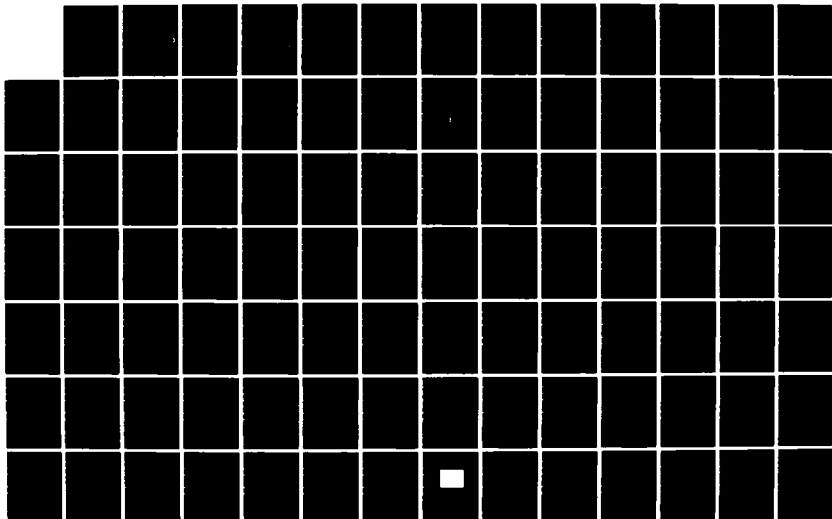
HARMONIC EMISSION FROM HIGH POWER GYROTRON OSCILLATORS
(U) AIR FORCE INST OF TECH WRIGHT-PATTERSON AFB OH
J L BYRRLY MAY 84 AFIT/CI/NR-84-43T

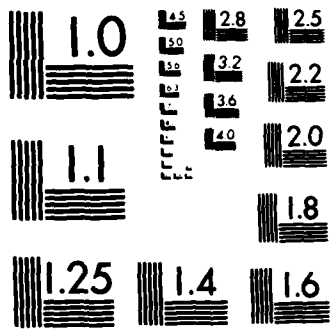
1/2

UNCLASSIFIED

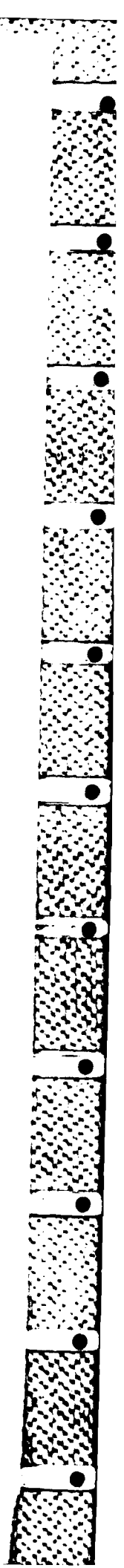
F/G 12/1

NL





MICROCOPY RESOLUTION TEST CHART
NATIONAL BUREAU OF STANDARDS-1963-A



UNCLASS

SECURITY CLASSIFICATION OF THIS PAGE (When Data Entered)

1

REPORT DOCUMENTATION PAGE

READ INSTRUCTIONS BEFORE COMPLETING FORM

1. REPORT NUMBER AFIT/CI/NR 84-43T		2. GOVT ACCESSION NO.	3. RECIPIENT'S CATALOG NUMBER
4. TITLE (and Subtitle) Harmonic Emission From High Power Gyrotron Oscillators		5. TYPE OF REPORT & PERIOD COVERED THESIS/DISSERTATION	
7. AUTHOR(s) Joseph Lawrence Byerly		6. PERFORMING ORG. REPORT NUMBER	
9. PERFORMING ORGANIZATION NAME AND ADDRESS AFIT STUDENT AT: Massachusetts Institute of Technology		8. CONTRACT OR GRANT NUMBER(s)	
11. CONTROLLING OFFICE NAME AND ADDRESS AFIT/NR WPAFB OH 45433		10. PROGRAM ELEMENT, PROJECT, TASK AREA & WORK UNIT NUMBERS	
14. MONITORING AGENCY NAME & ADDRESS (if different from Controlling Office)		12. REPORT DATE May 1984	
		13. NUMBER OF PAGES 148	
		15. SECURITY CLASS. (of this report) UNCLASS	
		15a. DECLASSIFICATION/DOWNGRADING SCHEDULE	

16. DISTRIBUTION STATEMENT (of this Report)
APPROVED FOR PUBLIC RELEASE; DISTRIBUTION UNLIMITED

DTIC ELECTE
SEP 17 1984
S D
B

17. DISTRIBUTION STATEMENT (of the abstract entered in Block 20, if different from Report)

18. SUPPLEMENTARY NOTES
APPROVED FOR PUBLIC RELEASE: IAW AFR 190-1/

Lynn Wolaver
LYNN E. WOLAVER
Dean for Research and Professional Development
AFIT, Wright-Patterson AFB OH

19. KEY WORDS (Continue on reverse side if necessary and identify by block number)

20. ABSTRACT (Continue on reverse side if necessary and identify by block number)
ATTACHED

AD-A14F 621

DTIC FILE COPY

AFIT RESEARCH ASSESSMENT

The purpose of this questionnaire is to ascertain the value and/or contribution of research accomplished by students or faculty of the Air Force Institute of Technology (AU). It would be greatly appreciated if you would complete the following questionnaire and return it to:

AFIT/NR
Wright-Patterson AFB OH 45433

RESEARCH TITLE: Harmonic Emission From High Power Gyrotron Oscillators

AUTHOR: Joseph Lawrence Byerly

RESEARCH ASSESSMENT QUESTIONS:

1. Did this research contribute to a current Air Force project?

a. YES b. NO
2. Do you believe this research topic is significant enough that it would have been researched (or contracted) by your organization or another agency if AFIT had not?

a. YES b. NO
3. The benefits of AFIT research can often be expressed by the equivalent value that your agency achieved/received by virtue of AFIT performing the research. Can you estimate what this research would have cost if it had been accomplished under contract or if it had been done in-house in terms of manpower and/or dollars?

a. MAN-YEARS _____ b. \$ _____
4. Often it is not possible to attach equivalent dollar values to research, although the results of the research may, in fact, be important. Whether or not you were able to establish an equivalent value for this research (3. above), what is your estimate of its significance?

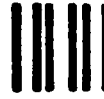
a. HIGHLY SIGNIFICANT b. SIGNIFICANT c. SLIGHTLY SIGNIFICANT d. OF NO SIGNIFICANCE
5. AFIT welcomes any further comments you may have on the above questions, or any additional details concerning the current application, future potential, or other value of this research. Please use the bottom part of this questionnaire for your statement(s).

NAME	GRADE	POSITION
ORGANIZATION	LOCATION	

STATEMENT(s):

FOLD DOWN ON OUTSIDE - SEAL WITH TAPE

AFIT/NR
WRIGHT-PATTERSON AFB OH 45433
OFFICIAL BUSINESS
PENALTY FOR PRIVATE USE: \$300



NO POSTAGE
NECESSARY
IF MAILED
IN THE
UNITED STATES

BUSINESS REPLY MAIL

FIRST CLASS PERMIT NO. 73296 WASHINGTON D.C.

POSTAGE WILL BE PAID BY ADDRESSEE

AFIT/ DAA

Wright-Patterson AFB OH 45433



FOLD IN

HARMONIC EMISSION FROM HIGH POWER
GYROTRON OSCILLATORS

by

JOSEPH LAWRENCE BYERLY
B.S., United States Air Force Academy
(1976)

SUBMITTED IN PARTIAL FULFILLMENT
OF THE REQUIREMENTS OF THE
DEGREE OF

MASTER OF SCIENCE
IN PHYSICS

at the

MASSACHUSETTS INSTITUTE OF TECHNOLOGY
May 1984

© Massachusetts Institute of Technology 1984

Signature of Author Joseph L. Byerly
Department of Physics

May 11, 1984

Certified by Richard J. Temkin
Richard J. Temkin
Thesis Supervisor

Accepted by _____
George F. Koster
Chairman, Graduate Committee

HARMONIC EMISSION FROM HIGH POWER GYROTRON OSCILLATORS

by

JOSEPH LAWRENCE BYERLY

Submitted to the Department of Physics
on May 11, 1984 in partial fulfillment of the requirements
for the Degree of Master of Science in Physics

ABSTRACT

Experimental and theoretical results are presented for the second harmonic emission ($\omega \approx 2\omega_c$, where ω_c is the electron cyclotron frequency) from a pulsed, high power gyrotron designed for high frequency fundamental ($\omega \approx \omega_c$) operation. The gyrotron produces more than 100 kW of output power at 140 GHz in the $TE_{0,3,1}$ mode at the fundamental. Eight second harmonic modes were observed in gyrotron operation between 4.0 and 6.0 tesla with 65 kV beam voltage and up to five amps of beam current. The two strongest modes were the $TE_{11,2,1}$ at 241 GHz which produced approximately 25 kW of output power at 7% efficiency and the $TE_{9,2,1}$ with ≈ 15 kW at 209 GHz. These represent the highest power measured for high frequency (> 100 GHz) gyrotron operation at a harmonic.

The theoretical investigation involved a linear theory for determining threshold oscillation conditions and two nonlinear theories for efficiency calculations. For the gyrotron resonator which is excited at the fundamental in the $TE_{0,3,1}$ mode at 140 GHz, there are 36 different modes in the frequency range 203-303 GHz which could be excited at $\omega \approx 2\omega_c$ for a magnetic field between 4.0-6.0 tesla. The linear theory results predicted 28 of these second harmonic resonator modes to be above threshold for operation at 65 kV and five amps. Minimum starting currents for the strongest second harmonic modes were calculated to be 0.5 A, which is of the same order as starting currents for fundamental modes. The calculations using both slow and fast time scale nonlinear theories predicted overall efficiencies of $\approx 20\%$. This is only a factor of two lower than the theoretical fundamental mode efficiencies. The relatively high second harmonic efficiencies arise because these modes have higher Q factors which compensate for the reduced gain at the harmonics.

The measured harmonic emission was less than the theoretical predictions both in terms of number of modes observed and the overall efficiencies. A number of possible explanations for the discrepancy were considered. At most magnetic field values there was some radiation at the fundamental and the second harmonic signal was weak or nonexistent. The two strong second harmonic modes appeared at magnetic field values where there was no fundamental oscillation. This seemed to indicate that oscillation at the fundamental was suppressing the weaker and missing second harmonic modes. A qualitative consideration of the mode competition between the fundamental and second harmonic supports this interpretation of mode suppression.

The present study indicates that second harmonic emission can achieve high power levels at very high frequencies with reasonable efficiencies. Using available superconducting magnets and second harmonic operation, high power emission well into the submillimeter (> 600 GHz) appears feasible.

Thesis Supervisor: Dr. Richard J. Temkin

Title: Leader, Millimeter Source Group, MIT Plasma Fusion Center

ACKNOWLEDGEMENTS

I am indebted to a number of people whose selfless efforts made this thesis possible. Foremost is Dr. Richard Temkin for his freely offered knowledge, guidance and encouragement through the entire course of my work with the gyrotron group at MIT.

Dr. Bruce Danly made clear the difficult aspects of the nonlinear theory and developed a computer code which significantly reduced the effort required in efficiency calculations. He also conducted the major portion of the experimental investigation. Dr. Kenneth Kreischer provided significant contributions to my knowledge of gyrotron theory, including particularly useful explanations of the linear theory and associated computer code. I am grateful for the technical help provided by William J. Mulligan during the experimental work and for the assistance provided by John Schutkeker in running the fast time scale computer code.

Finally, I wish to thank my wife, Heidi, for her tireless patience and understanding throughout my studies at MIT.

Accession For	
NTIS GRA&I	<input checked="" type="checkbox"/>
DTIC TAB	<input type="checkbox"/>
Unannounced	<input type="checkbox"/>
Justification	
By	
Distribution/	
Availability Codes	
Dist	Avail and/or Special
A-1	



Table of Contents

Abstract	2
Acknowledgements	3
List of Figures	5
List of Tables	6
Chapter 1 — Introduction	7
1.1 — Historical Development of the Gyrotron	8
1.2 — The MIT Gyrotron	15
1.3 — Motivation for an Harmonic Emission Study	18
Chapter 2 — Theory	21
Description of the Gain Mechanism	22
Definitions of Q and η	24
2.1 — The Electromagnetic Field Structure in an Open Resonator	26
Application of the CAVRF Code	27
Using CAVRF for the Gaussian Approximation to $f(z)$	32
2.2 — The Linear Theory of the Gyrotron	34
Description of the Linear Analysis	35
Derivation of the Gaponov Result	38
Application of the Linear Theory	41
2.3 — The Nonlinear Theory of the Gyrotron	52
Derivation of the Slow Time Scale Equations	53
Application of the Slow Time Scale Theory	59
Fast Time Scale Efficiency Calculations	69
2.4 — $\omega_c \rightarrow 2\omega_c$ Efficiency Scaling	76
Chapter 3 — Description of the Experiment	82
3.1 — The Magnetic Field Scan to Detect Harmonic Emission	83
3.2 — Frequency Determination by Harmonic Mixing	91
3.3 — Starting Current Determination	96
3.4 — Output Power Level Measurements	97
Chapter 4 — Discussion of the Results	107
4.1 — Finite Beam Width Effects	109
4.2 — Mode Competition	124
Chapter 5 — Higher Harmonics	130
Chapter 6 — Conclusions and Recommendations	137
6.1 — Summary and Further Conclusions	138
6.2 — Recommendations for Further Study	142
References	144

List of Figures

Chapter 1

Fig 1.1a — Gyrotrons Operating at the Fundamental	11
Fig 1.1b — Gyrotrons Operating at Higher Harmonics	14
Fig 1.2 — Schematic Diagram of the MIT Gyrotron	17

Chapter 2

Fig 2.1 — CAVRF Output Field Magnitude and Cavity Radius vs. Longitudinal Coordinate	28
Fig 2.2a — Second Harmonic Starting Currents for the 0,3,1 Cavity	43
Fig 2.2b — Second Harmonic Starting Currents for the Whispering Gallery Cavity	45
Fig 2.3a — $\omega \approx 2\omega_c$ Linear Code Plot of the of the 0,3,1 Cavity Mode Spectrum	50
Fig 2.3b — $\omega \approx 2\omega_c$ Linear Code Plot of the Whispering Gallery Cavity Mode Spectrum	51
Fig 2.4a — $\omega \approx 2\omega_c$ Isoefficiency Curves — Nusinovich and Erm — 1972 Integration Length of $-\frac{\sqrt{3}}{2}\mu \leq \zeta \leq +\frac{\sqrt{3}}{2}\mu$	62
Fig 2.4b — $\omega \approx 2\omega_c$ Isoefficiency Curves — Nusinovich and Erm — 1975 Integration Length of $-\sqrt{3}\mu \leq \zeta \leq +\frac{\sqrt{3}}{2}\mu$	62
Fig 2.5 — $\omega_c \rightarrow 2\omega_c$ Efficiency Estimation	80

Chapter 3

Fig 3.1 — Experimental Arrangement for the Magnetic Field Scan	84
Fig 3.2 — Fundamental and Second Harmonic Diode Pulse Shapes	87
Fig 3.3a — Fundamental Emission	88
Fig 3.3b — Second Harmonic Emission	89
Fig 3.4 — Schematic Diagram of the Harmonic Mixer System	92
Fig 3.5a — Dispersive Fourier Transform Spectroscopy Reflectivity Plot of the 4 inch Scientech Calorimeter	100
Fig 3.5b — Dispersive Fourier Transform Spectroscopy Reflectivity Plot of the 1 inch Scientech Calorimeter	101

Chapter 4

Fig 4.1 — $TE_{4,4,1}$ Mode Starting Current as a Function of r_e	112
Fig 4.2 — I_{ST} vs. r_e for the $TE_{11,2,1}$, $TE_{8,3,1}$ and $TE_{3,5,1}$ Modes	119
Fig 4.3 — $TE_{1,6,1}$ Mode Starting Current as a Function of r_e	122
Fig 4.4 — $\omega_c \leftrightarrow 2\omega_c$ Mode Competition	127

List of Tables

Chapter 2

Table 2.1a — 0.3,1 Cavity $\omega \approx 2\omega_c$ CAVRF Results	30
Table 2.1b — Whispering Gallery Cavity $\omega \approx 2\omega_c$ CAVRF Results	31
Table 2.2a — 0.3,1 Cavity $\omega \approx 2\omega_c$ Starting Currents	43
Table 2.2b — Whispering Gallery Cavity $\omega \approx 2\omega_c$ Starting Currents	45
Table 2.3a — 0.3,1 Cavity $\omega \approx 2\omega_c$ Efficiency Calculations Nusinovich and Erm — 1972, Integration Length of $-\frac{\sqrt{3}}{2}\mu \leq \zeta \leq +\frac{\sqrt{3}}{2}\mu$	64
Table 2.3b — Whispering Gallery Cavity $\omega \approx 2\omega_c$ Efficiency Calculations Nusinovich and Erm — 1972, Integration Length of $-\frac{\sqrt{3}}{2}\mu \leq \zeta \leq +\frac{\sqrt{3}}{2}\mu$	65
Table 2.4a — 0.3,1 Cavity $\omega \approx 2\omega_c$ Efficiency Calculations Nusinovich and Erm — 1975, Integration Length of $-\sqrt{3}\mu \leq \zeta \leq +\frac{\sqrt{3}}{2}\mu$	66
Table 2.4b — Whispering Gallery Cavity $\omega \approx 2\omega_c$ Efficiency Calculations Nusinovich and Erm — 1975, Integration Length of $-\sqrt{3}\mu \leq \zeta \leq +\frac{\sqrt{3}}{2}\mu$	67
Table 2.5a — 0.3,1 Cavity $\omega \approx 2\omega_c$ Efficiency Calculations Fast Time Scale Particle Integrator Integration Length of $-\frac{\sqrt{3}}{2}\mu \leq \zeta \leq +\frac{\sqrt{3}}{2}\mu$	73
Table 2.5b — 0.3,1 Cavity $\omega \approx 2\omega_c$ Efficiency Calculations Fast Time Scale Particle Integrator Integration Length of $-2\sqrt{3}\mu \leq \zeta \leq +2\sqrt{3}\mu$	74
Table 2.6 — 0.3,1 Cavity $\omega \approx 2\omega_c$ Efficiency Calculations Comparison	75

Chapter 3

Table 3.1 — Observed Second Harmonic Emission	95
Table 3.2 — Second Harmonic Power Measurements	105

Chapter 4

Table 4.1 — Adiabatic Theory Beam Radius Calculations for Observed Second Harmonic Modes	114
Table 4.2 — Adjusted 0.3,1 Cavity $\omega \approx 2\omega_c$ Starting Currents Including Finite Beam Width Factor	115

Chapter 5

Table 5.1 — 0.3,1 Cavity $\omega \approx 3\omega_c$ Starting Currents	132
Table 5.2 — 0.3,1 Cavity $\omega \approx 4\omega_c$ Starting Currents	133
Table 5.3 — 0.3,1 Cavity $\omega \approx 3\omega_c$ Efficiency Calculations Nusinovich and Erm — 1972, Integration Length of $-\frac{\sqrt{3}}{2}\mu \leq \zeta \leq +\frac{\sqrt{3}}{2}\mu$	135

Chapter 1

Introduction

Within the past two decades, the gyrotron has rapidly developed as an efficient source of high frequency microwave radiation. A worldwide effort of experimental gyrotron designs has produced a wide range of operating parameters including output power levels in excess of a megawatt, pulse lengths from microseconds to continuous (cw), and wavelengths from several centimeters to well into the submillimeter. The technology and demand for gyrotrons is such that they are now available commercially.

Increasing with the performance level of gyrotrons is the list of proposed applications. Among these are high frequency radar, particle accelerators, spectroscopy of biological materials, and as a scattering source for plasma diagnostics. But the most impressive application thus far has been in electron cyclotron resonance heating (ECRH) experiments in magnetically confined fusion devices. Significant bulk plasma heating increases have been recorded in the Soviet Union [1] and gyrotrons for ECRH have become an integral part of many experimental fusion machines in the United States. The ECRH demands of a commercially

viable fusion reactor have driven the long term gyrotron goals to long pulse, high efficiency, with megawatt power levels in the 100-300 GHz frequency range. As stated previously, each of these goals alone has been realized, but no gyrotron exists today which incorporates all of them.

1.1 — Historical Development of the Gyrotron

Microwave devices in the 1950's all had similar limitations which precluded design and operation in the millimeter and submillimeter regime. Internal component dimensions were directly related to the wavelength (λ) of the output radiation. Systems such as the travelling wave tube (TWT) or magnetron required a periodic structure on the order of λ and klystrons had electrodes with dimensions less than λ . Obviously, radiation wavelengths of a few millimeters or less required a new mechanism for amplification.

Such a mechanism was first theorized in 1958 by R. Q. Twiss [2]. An astrophysicist, Twiss surmised that under certain conditions, electromagnetic radiation traversing a magnetized, relativistic plasma would be amplified. In 1959, Schneider [3] using quantum mechanics and A. V. Gaponov [4] employing a classical treatment, separately reached a similar conclusion concerning the possibility of gain from relativistic electrons gyrating in a magnetic field. Hirshfield and Wachtel [5] provided the first experimental confirmation of the gain mechanism in 1964.

The amplified radiation from the theorized interaction was necessarily near the Doppler shifted cyclotron resonance. With ω representing the angular frequency and \vec{k} the wave vector of the radiation, the condition may be stated

$$\omega - \vec{k} \cdot \vec{v} \approx n\omega_c \quad (1.1)$$

where n is an integer representing the harmonic number, \vec{v} the drift velocity and ω_c is the relativistic electron gyrofrequency. That is

$$\omega_c = \frac{eB}{\gamma m_e} \quad (1.2)$$

with e and m_e the electron charge and rest mass, B the magnetic field strength and γ is the relativistic factor given by

$$\gamma = \frac{1}{\sqrt{1 - \beta^2}} \quad (1.3)$$

where $\beta = v/c$ is the velocity normalized to the speed of light (c). Appropriately enough, devices employing this amplification mechanism were called *electron cyclotron masers* (ECM) or *cyclotron resonance masers* (CRM), the latter term appearing extensively in Soviet literature.

Theoretical and experimental work continued throughout the 1960's with a massive effort taking place in the Soviet Union. Many possible configurations of electron beam and magnetic field were considered. However, the most promising was a helical, annular electron beam from a magnetron injection gun transiting an open resonator near cutoff, aligned with a static magnetic field. This combined the capability to confine an intense, monoenergetic electron beam with the decided advantage of simplicity of design and construction. By operating near the cutoff frequency of the resonator cavity, the $\vec{k} \cdot \vec{v}$ term is small so that high efficiency can be achieved with electron beams having a large velocity spread. The term gyrotron was first used by Gaponov [6] for devices of this description. The name gyrotron has since acquired the additional restrictive meaning of weakly relativistic electron beam voltages, such that $\beta^2 \ll 1$.

In the latter half of the 1960's, interest in this class of free electron device was minimal in the west, but the Soviet effort continued with significant theoretical advances. In particular, a nonlinear theory developed Gaponov, Petelin, and Yulpatov [7] and reduced to a particularly tractable form by Nusinovich and Erm [8], allowed gyrotron efficiency calculations and thus optimization of device parameters including resonator cavity profile. The results of the theoretical work became evident in the early 1970's when Soviet experimentalists provided impressive milestones of achievement. These results sparked renewed interest in gyrotron research in the west.

A diagram of the status of gyrotron research to date is shown in Figures 1.1a and 1.1b. Figure 1.1a considers only gyrotrons operating at the fundamental ($n = 1$) while Figure 1.1b depicts the results at higher harmonics ($n > 1$). Both graphs show achievements in terms of frequency and output power with separate symbols for various degrees of pulsed operation. For these figures, operation with pulse duration of less than 10 msec was considered short pulse, while greater than 50 msec is shown as long pulse.

Examination of Figure 1.1a reveals the tradeoff between long pulse length and high output power at high frequency. The highest output power in cw operation is the 342 kW Varian [9] result at 28 GHz. Varian [10] and Hughes [11] have both produced 200 kW, 60 GHz gyrotrons. The Hughes version is long pulsed and the Varian design is capable of cw operation. It should be mentioned that chart space in Figure 1.1a did not allow inclusion of the increasing number of commercial ventures in this low frequency, long pulse regime. In particular, Thomson-CSF [12]

and Nippon Electric Company (NEC) [13] have produced ~ 200 kW gyrotrons for long pulse operation at 35 GHz. Toshiba has also constructed 22 and 70 GHz gyrotrons [14]. The Soviet contribution in this area of operation are gyrotrons presently used to heat the Kurchatov T-10 Tokamak [15]. These devices operate at 85 GHz with an average output power of 200 kW in pulses of up to about 50 msec.

Increasing the frequency of cw operation has resulted in significant decreases in the output power available. As shown in Figure 1.1a, the highest frequency yet achieved in cw operation at the fundamental is 150 GHz with 22 kW of output power reported by Andronov et al. [16]. This surpassed the 1974 result described by Zaytsev [17] of a cw gyrotron capable of 12 kW at 107 GHz.

Short pulsed operation greatly increases the operating space, both in terms of power and frequency. The 1 MW power level was first exceeded by a gyrotron operating in short pulses at the fundamental in 1978 as reported by Andronov [16]. These results included the achievement of 1.25 MW at 45 GHz and 1.1 MW at 100 GHz. Experiments by Gol'denberg which were reported by Flyagin [18] recently exceeded this power level. Using a 90 kV, 50 A electron beam with a 10 μ sec pulse length, 1.4 MW of output power was achieved at 100 GHz. The same paper described experiments well into the submillimeter by Luchinin and Nusinovich, which are represented in Figure 1.1a by the six points beyond 300 GHz with power levels from 20 to 130 kW. These dramatic results were produced by using pulsed magnets capable of 23 tesla.

The final points in Figure 1.1a represent short pulsed results, but were designed for extension to the cw and ECRH applications. Wall loading effects on the resonator cavity were considered and continuous magnets were used. A gyrotron at the Naval Research Laboratory (NRL) [19] achieved 340 kW of output power at 35 GHz with an incredible 53% efficiency. The MIT gyrotron [20] produced 175 kW of power at 140 GHz in operation at the fundamental. This represents the highest power at high frequency (> 100 GHz) in a low ohmic loss resonator mode which is compatible with scaling up to long pulse or cw operation.

High power gyrotrons operating at harmonics of the cyclotron frequency are shown in Figure 1.1b. All of the results depicted are second harmonic ($n = 2$) except for one third harmonic result which is labelled.

A large part of the Soviet experimental effort in the early 1970's used gyrotrons designed for operation at the second harmonic. In 1974, Kisel [21] obtained 10 kW of cw power and 30 kW in pulsed operation at 34 GHz. The next month, Zaytsev [17] published results of 7 kW at 154 GHz in pulsed operation, with 2.4 kW at 157 GHz and 1.5 kW at 326 GHz in cw operation. Recent Soviet harmonic gyrotron investigations by Zapevalov reveal a marked increase in power and efficiency by using a stepped profile cavity. In 1979 [22], pulsed operation at 25 GHz produced 500 kW. The latest Zapevalov results [23] include a pulsed second harmonic gyrotron emitting 150 kW of output power at 34 GHz, and third harmonic pulsed operation producing 100 kW of power at 55 GHz. This last result represents a remarkable 10% efficiency at the third harmonic.

There have been few investigations of high power, high frequency harmonic operation outside of the Soviet Union. The Harry Diamond Laboratories in conjunction with NRL [24] completed a design effort for a 240 GHz, ~ 10 kW gyrotron, but initial experimental results have yet to produce the expected efficiencies. Some work has been carried out in the People's Republic of China (PRC), including 30 kW of power at 37 GHz [25]. Thomson-CSF [12] has recently reported on initial studies of a second harmonic gyrotron which has produced ~ 30 kW at 70 GHz. The only other high power, second harmonic operation of a gyrotron is the MIT result [26], which is the basis for this thesis. As depicted in Figure 1.1b, the 25 kW of output power at 241 GHz achieved in the present study is a singular achievement for harmonic operation. In the future, it may be possible to extend these results to higher power and frequency.

1.2 -- The MIT Gyrotron

The MIT results cited in the previous section were produced by a gyrotron which has been in operation since 1982 at the Francis Bitter National Magnet Laboratory on the MIT campus. The design and initial results were reported in [27]. Recent results describing enhanced efficiency and improved diagnostics are found in [20].

Figure 1.2 is a schematic diagram of the device. The overall axisymmetric geometry is typical of most gyrotron designs. To the left in Figure 1.2 is the electron gun which produces an annular electron beam. The beam travels to the right entering the magnetic compression region and through the resonator cavity. Exiting the resonator and high magnetic field region, the beam is deposited on

the collector which also serves as an oversized output waveguide for the generated RF. The microwave radiation passes through a fused quartz output window which allows the entire resonator tube section to be kept under vacuum, normally less than 4×10^{-8} torr.

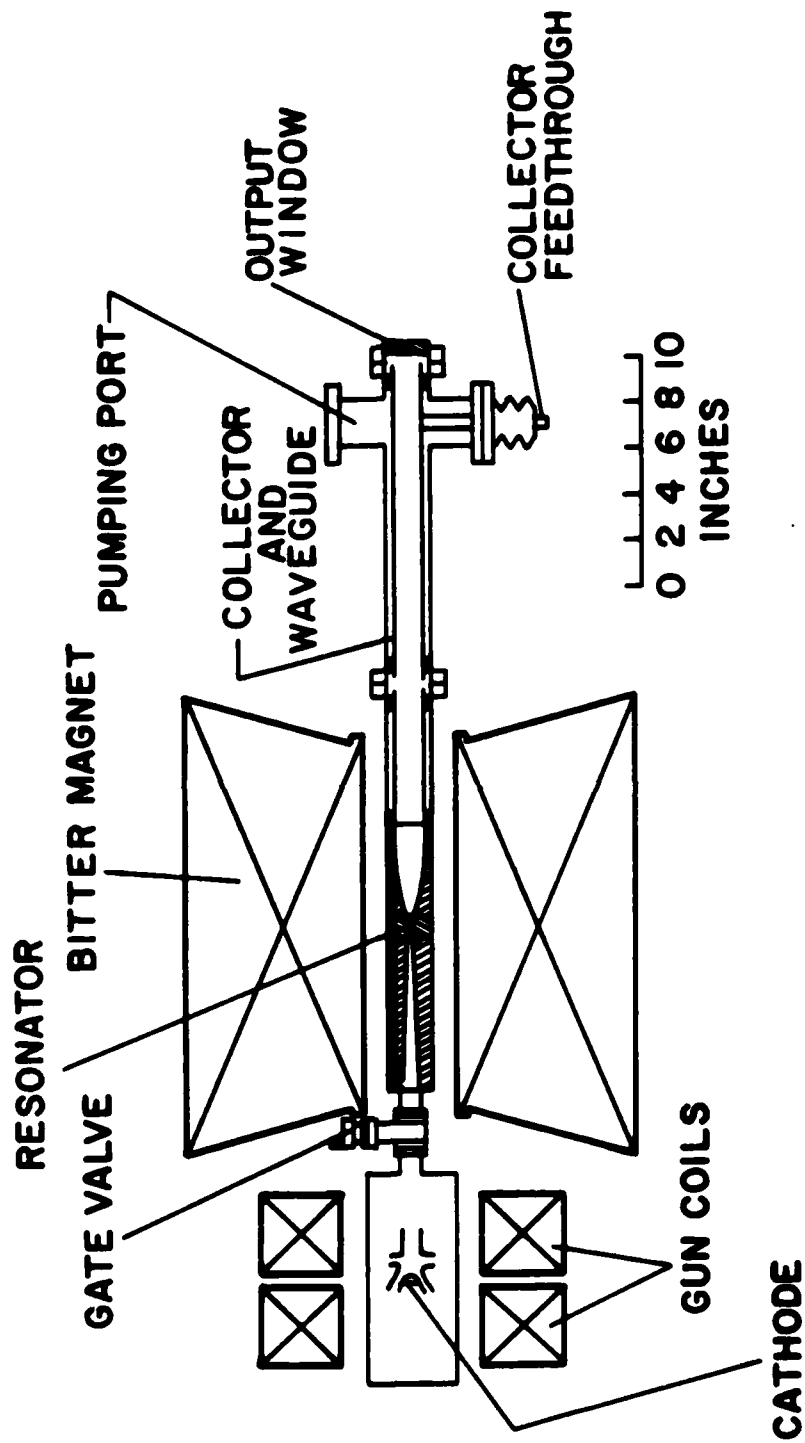
The electron gun is a magnetron injection type constructed by Varian Associates [28] which produces a nonlaminar flow of electrons. The designed ratio of perpendicular to parallel velocities (v_{\perp}/v_{\parallel}) with respect to the main magnetic field is 1.49. Beam cathode voltages of up to 80 kV have been used producing beam currents of up to 10 A.

The Bitter magnet which produces the main solenoidal field is a copper core, water cooled magnet capable of generating fields in excess of 10 T in cw operation. Additionally, two coils capable of generating 0.2 T are located symmetrically about the electron gun cathode region to allow minor changes in the magnetic compression and beam quality. These are labelled "gun coils" in Figure 1.2.

The resonator cavity is a section of cylindrical waveguide with a downtaper on the beam input end and an uptaper to the output waveguide on the other end. The input section downtaper is intended to keep the microwave radiation from leaking back towards the electron gun.

The same resonator produced both the 140 GHz, 175 kW fundamental result and the 241 GHz, 25 kW second harmonic result shown in Figures 1.1a and 1.1b. The cavity was designed for fundamental operation in the $TE_{0,3,1}$ mode with a straight section length of 6λ and a radius of 0.348 cm. The theoretical diffractive Q (Q_D) of the cavity was 1500 at the fundamental. For cw applicability, the cavity

Fig 1.2 — Schematic Diagram of the MIT Gyrotron



M.I.T. 140 GHZ GYROTRON

wall loading was constrained to 2 kW/cm^2 and the electron beam was placed to interact with the second radial maximum of the electromagnetic field. This unique feature reduces space charge forces in the beam which could degrade efficiency.

The gyrotron operates in a pulsed mode with a pulse length of $1 \mu\text{sec}$ and a repetition rate of 4 Hz . Nominal beam voltage and current for the investigation described by this paper were 64.3 kV and 5 A . The electron beam guiding center radius in the resonator was designed for 0.182 cm , but adjustments to the gun coils affecting the magnetic compression yield 0.197 cm as a more realistic figure. These values are mentioned now, since they are important parameters in the theories discussed in Chapter 2.

1.3 -- Motivation for an Harmonic Emission Investigation

Harmonic emission from high power gyrotrons demands investigation from two overall distinct points of view. The first is that gyrotrons designed for harmonic operation are viable for some applications. The second is that harmonic emission can produce serious effects on a gyrotron intended for operation at the fundamental.

Examining these in order, Soviet experimentalists have designed gyrotrons for harmonic operation and achieved impressive results. Analytic theories discussed in Chapter 2 predict reasonable efficiencies ($\sim 20\%$) at the second harmonic for a gyrotron operating with the parameters of the present device. The major advantage of harmonic operation is the lowering of the magnetic field requirement. Since in a gyrotron, $\omega \approx n\omega_c$ and $\omega_c \sim B$, going to second harmonic operation effectively halves the magnetic field required to produce the same frequency. Efficient, high

harmonic operation therefore leads to the possibility of using permanent magnets at some time in the future.

Achieving high efficiency in high harmonic operation was the goal of three recent studies. Experiments by Hirshfield [29] on a CRM employing a solid beam Pierce gun have produced emission at up to the ninth harmonic at wavelengths from 8 mm to less than 1 mm. The theoretical interpretation presented by the same author in an earlier paper [30] and supported by these results, is that coupling at the beam boundary excites Bernstein modes on the beam. Lau [31] has proposed a device called a gyro-magnetron which has a corrugated resonator wall similar to a magnetron. Emission would occur predominantly at the cyclotron harmonic corresponding to the number of vanes in the cavity. A mildly relativistic, annular electron beam would still be employed. Finally, McDermott et al. [32] have reported on a gyrotron with a unique axis-encircling electron beam. Initial results have produced multi-kW power levels from the eleventh harmonic at 65 GHz.

The second major reason for studying harmonic emission is to understand its effects on a gyrotron designed for operation at the fundamental. Unrestrained harmonic oscillation could possibly damage tube components such as the output window. Mode competition between the desired fundamental mode and parasitic harmonic modes could result in degraded efficiency.

Finally, megawatt designed gyrotrons in the future will necessitate the use of highly overmoded resonators. A study of the harmonic emission permits the inves-

tigation of an overmoded cavity. For example, the MIT gyrotron has a resonator diameter of $\sim 3\lambda$ at the fundamental and therefore $\sim 6\lambda$ at the second harmonic.

This paper details an harmonic emission study on the MIT gyrotron. Chapter 2 presents linear and nonlinear theories and applies them to predict the second harmonic modes that should be excited and their efficiency. Chapter 3 describes the experimental investigation to identify harmonic emission, measure starting current and output power. Chapter 4 discusses the results and offers explanations for discrepancies between theory and experiment. Chapter 5 considers the possibility of higher harmonic emission with $n > 2$ and Chapter 6 concludes with a summary and recommendations for further study.

Chapter 2

Theory

All quantitative theories regarding gyrotron operation must consider the coupled problems of the Lorentz force dominated electron dynamics and the electromagnetic fields described by Maxwell's equations. The complete solution considering specific device geometries is quite intractable, even using numerical methods. Therefore, the major differences in gyrotron theories are in their assumptions and their degrees of completeness. The linear theory is useful in determining the start of oscillation conditions. The nonlinear theory is required to predict the output power of an oscillator, and therefore is needed in efficiency calculations.

This chapter will outline the basic development of both the linear and nonlinear theories of the gyrotron. These theories will then be applied specifically to the MIT gyrotron to predict its performance at second harmonic operation. Two separate resonator cavities will be discussed. The first is described in Section 1.2 of this paper and will be referred to as the 0,3,1 cavity. All of the experimental work described in later chapters used this resonator. The second cavity which was designed for operation at the fundamental in the $TE_{6,1,1}$ mode, will be referred

to as the whispering gallery cavity. Extensive experimental work is planned for this resonator in the future. The chapter concludes by using a nonlinear theory to make an efficiency scaling approximation from the fundamental to the second harmonic.

— *Description of the Gain Mechanism* —

The radiation producing interaction in gyrotrons can be understood by elementary arguments using a classical description. The discussion presented here follows the development in an undergraduate physics text by Bekefi and Barrett [33]. The simplified geometry to be considered is a beam of monoenergetic electrons travelling in helical paths about static magnetic field lines. The electrons encounter an oscillating electromagnetic field in the resonator cavity, which for the purposes of this schematic can be considered unperturbed by the presence of the electron beam.

Entering the interaction region, the electrons have random phases in the plane perpendicular to the direction of the magnetic field. The transverse component of the high frequency RF field in the resonator will tend to accelerate some of the electrons and decelerate others. Variations in the field across the Larmor orbit are ignored here, so this discussion is only applicable at the fundamental. Those electrons which are accelerated initially by the electric field will increase in mass by the relativistic factor γ . The increase in γ will decrease the cyclotron frequency since $\omega_c \sim 1/\gamma$. These electrons will be retarded in phase relative to those not initially accelerated. Conversely, electrons which are decelerated by the electric field will have a resultant decrease in γ , an increase in ω_c , and therefore advance

in phase. Azimuthal electron bunching will occur, with relativistic mass effects providing the bunching mechanism.

Simplified conditions for gain may be derived [34] by now viewing the electron bunch as a single negative charge orbiting at ω_c near synchronism with the RF field, oscillating at ω . If the cyclotron frequency is slightly greater than ω , then after several periods of oscillation the electron bunch will be positioned such that it is accelerating and gaining energy at the expense of the field. However, if ω_c is slightly less than ω , then after several periods the bunch will be decelerated, giving up energy to the RF field. In simple terms, the gyrotron depends on relativistic electrons for azimuthal bunching and a gyrofrequency such that $\omega_c < \omega$ for gain.

This description details the interaction at the fundamental of the cyclotron frequency. To generalize to the n^{th} harmonic, the finite Larmor radius must be included and the electron must be perturbed by the field n times in one gyro orbit. The field may be represented by an n^{th} order multipole expansion and the beam interaction involves the n^{th} derivative of the field. The simplified gain condition becomes $\omega - n\omega_c \ll \omega$.

The azimuthal bunching described above is the electron cyclotron maser instability generally associated with CRM's. Additionally, there is the possibility of axial bunching of the electrons leading to what is termed a Weibel-type instability [35]. The axial bunching arises from the Lorentz force interaction between the electrons and the RF magnetic field and is not at all dependent on relativistic effects. Chu and Hirshfield [36] have shown that the two bunching mechanisms compete with each other, so that depending on the particular device, one will dominate. In

an earlier paper, Hirshfield [37] concluded that the azimuthal bunching dominates in fast wave interactions. Since a gyrotron operates near cutoff, the wave vector components satisfy

$$k_{\perp}^2 \gg k_{\parallel}^2. \quad (2.1)$$

Here k_{\perp} and k_{\parallel} represent the component magnitudes of \vec{k} in the directions perpendicular and parallel to the static magnetic field respectively. Thus the Doppler shift term $k_{\parallel}v_{\parallel}$ is small and the fast wave condition

$$\omega/k_{\parallel} \gg c \quad (2.2)$$

is satisfied. Therefore the axial bunching is ignored in most gyrotron theories. It has been shown [38] by similar arguments that the electron beam interacts with TM modes with substantially lower efficiency than with TE modes. For this reason, TM modes are generally not considered and will not be discussed in this paper.

— Definitions of Q and η —

It is useful at this point to introduce some parameters which appear throughout CRM theories in power balance relationships. The diffractive Q (Q_D) is related to the stored energy in the cavity (U) and the RF output power (P_{out}) by

$$Q_D = \frac{\omega U}{P_{\text{out}}}. \quad (2.3)$$

Since some energy is extracted by ohmic losses, a similar relationship exists between the ohmic Q (Q_{ohm}) and the power that is used in wall heating (P_{ohm}). The overall quality factor (Q) includes both diffractive and ohmic losses.

$$\frac{1}{Q} = \frac{1}{Q_D} + \frac{1}{Q_{\text{ohm}}} \quad (2.4)$$

The output efficiency η of a gyrotron is defined by $\eta = P_{\text{out}}/P_{\text{in}}$ where P_{in} represents the beam power given by $P_{\text{in}} = IV_c$. Here I is the beam current and V_c the cathode voltage. As with the Q factors, consideration of the fact that some of the RF energy heats the walls instead of travelling out the waveguide leads to the definition of the electronic efficiency $\eta_{e\ell}$. Both power loss mechanisms are included in $\eta_{e\ell}$ by the expression $\eta_{e\ell} = (P_{\text{out}} + P_{\text{ohm}})/P_{\text{in}}$. The output efficiency may be written in terms of $\eta_{e\ell}$ by

$$\eta = \left(1 - \frac{Q}{Q_{\text{ohm}}}\right) \eta_{e\ell}. \quad (2.5)$$

Since only TE modes will be considered and the static magnetic field can do no work on the electrons, only the perpendicular velocity (v_{\perp}) of the electrons can contribute energy to the field. The parallel electron velocity (v_{\parallel}) remains constant throughout the cavity to the extent that the RF magnetic field may be ignored. The final efficiency to be defined, η_{\perp} , accounts for the fact that only the transverse beam energy may be converted to electromagnetic field energy. Equation (2.6) expresses the relationship between $\eta_{e\ell}$ and η_{\perp} .

$$\eta_{e\ell} = \frac{1}{1 + (v_{\parallel}/v_{\perp})^2} \eta \quad (2.6)$$

As a final set of useful definitions, the normalized velocities are $\beta_{\perp} = v_{\perp}/c$ and $\beta_{\parallel} = v_{\parallel}/c$. They are related to β introduced in Chapter 1 by $\beta^2 = \beta_{\perp}^2 + \beta_{\parallel}^2$. The relativistic γ written in terms of β in equation (1.3) may be calculated by

$$\gamma = 1 + \frac{V_c^2}{511} \quad (2.7)$$

when V_c is in kilovolts.

2.1 — The Electromagnetic Field Structure in an Open Resonator

All of the theories to be considered require some knowledge of the RF field structure in the cavity. The complete solution of this problem in actual gyrotron operation involves a coupled system of equations relating the perturbing effect of the electron beam on the cavity fields and the RF field effects on the particle dynamics. A reasonable first approximation is the cold cavity electromagnetic field solution disregarding the presence of the electron beam. The CAVRF computer code [39] developed at the Naval Research Laboratory provides such a solution.

The gyrotron resonator is basically a section of irregular waveguide aligned with the magnetic field. The solution to Maxwell's equations without source terms in a perfectly conducting, nonuniform waveguide had been considered previously, but Vlasov et al. [40] provided an approach specifically applicable to gyrotrons. In [39], Fliflet and Read continue with this development, rederiving the applicable equations and discussing the numerical methods employed in creating the CAVRF program.

In outlining the CAVRF solution technique, the longitudinal axis parallel to the magnetic field will be the z -direction. The longitudinal profile function of the field $f_s(z)$ satisfies the one dimensional wave equation

$$\frac{d^2 f_s}{dz^2} + \kappa_s^2(\omega, z) f_s = 0. \quad (2.8)$$

In equation (2.8), κ_s is the complex equivalent to k and the "s" subscripts denote that the quantities are mode dependent. The radiation boundary conditions which

ensure that the fields are decaying exponentially in the cutoff input section of the cavity and are travelling waves in the output section are

$$\left[\frac{df_s}{dz} - i\kappa_s f_s \right]_{z=z_{in}} = 0 \quad \text{and} \quad \left[\frac{df_s}{dz} + i\kappa_s f_s \right]_{z=z_{out}} = 0. \quad (2.9)$$

Here z_{in} and z_{out} refer to the coordinate positions of the input and output ends of the cavity.

The solutions to equation (2.8) with the boundary conditions (2.9) yield complex eigenfrequencies. The real part of the eigenfrequency is related to the actual frequency of radiation (ν) in the standard manner.

$$\nu = \frac{\text{Re } \omega}{2\pi} \quad (2.10)$$

The imaginary part can be used to determine the diffractive Q of the resonator by the relation

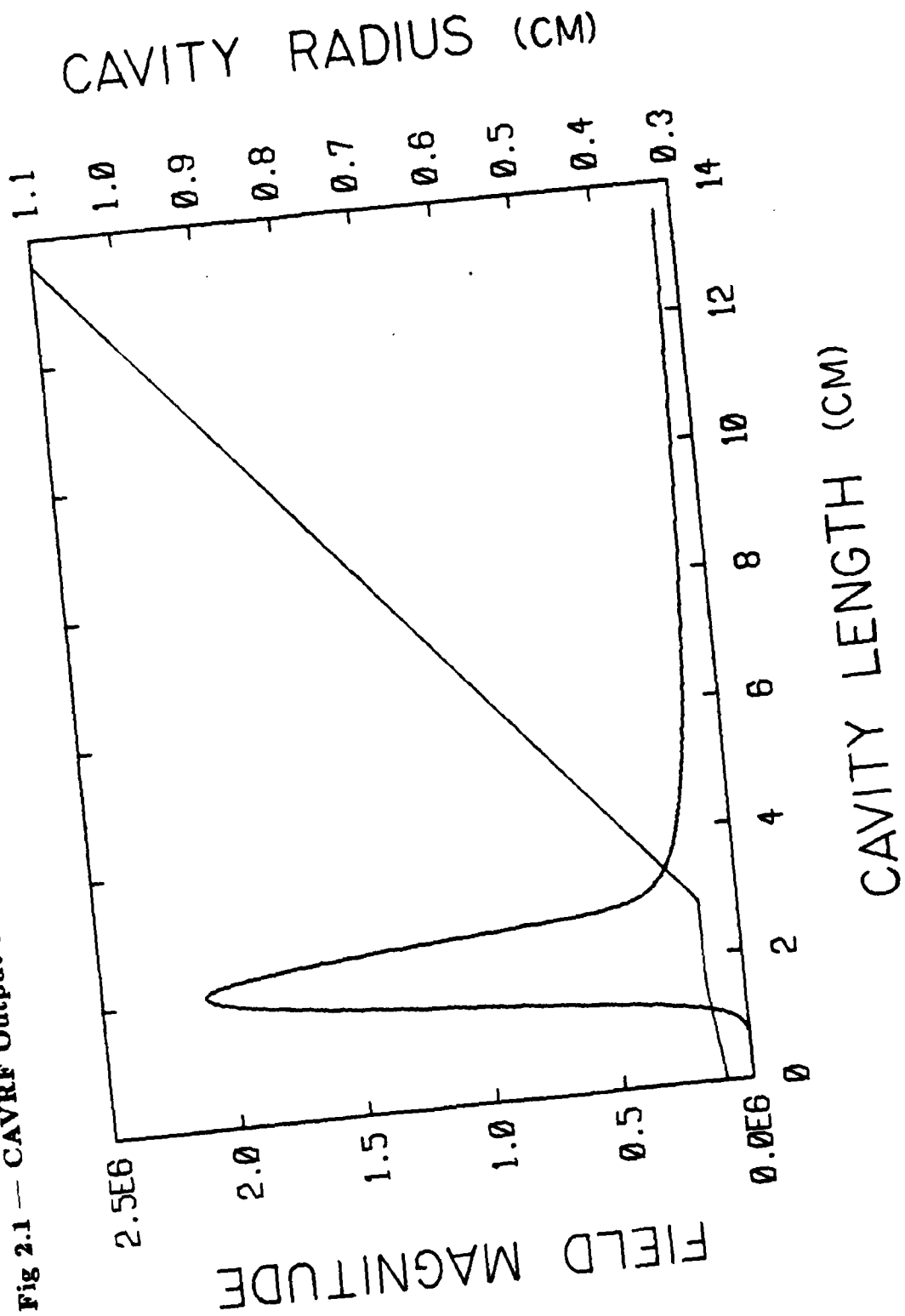
$$Q_D = \frac{\text{Re } \omega}{2(\text{Im } \omega)}. \quad (2.11)$$

The CAVRF program separates equation (2.8) into real and imaginary parts and numerically integrates the resulting pair of coupled second order differential equations. The eigenfrequency is found by an iterative procedure based on the method of steepest descent. The code requires the actual cavity dimensions as inputs and yields frequency, diffractive Q , and the magnitude and phase of f_s as a function of z .

Application of the CAVRF Code

Figure 2.1a shows a plot of the normalized field magnitude as a function of cavity length using an actual CAVRF output. The result depicted is for the

Fig 2.1 — CAVRF Output Field Magnitude and Cavity Radius vs. Longitudinal Coordinate



TE_{11,2,1} mode using the 0,3,1 cavity dimensions. Since this cavity was designed to oscillate at 140 GHz in the TE_{0,3,1} mode, it has a frequency of 241 GHz in the TE_{11,2,1} mode. Superimposed over the field magnitude plot are straight line segments representing the 0,3,1 cavity radius as a function of z . The radial dimension scale on the right is not the same as the longitudinal scale on the horizontal axis.

The CAVRF code remains sufficiently accurate only for resonator cavities which have a smoothly varying radius along z . Abrupt changes in the cavity radius violate the "weakly irregular" condition which permits separation of variables in solving the Helmholtz equation. Both the 0,3,1 and whispering gallery cavity profiles should satisfy the smoothly varying stipulation. The downtaper on the input end is 0.15° for the 0,3,1 cavity and 0.5° for the whispering gallery cavity. Both resonators have output uptaper angles of 4°.

The data presented in Tables 2.1a and 2.1b was generated by the CAVRF code. Table 2.1a represents all the possible TE _{$m,p,1$} modes which could oscillate at the second harmonic between 4.0 and 6.0 tesla in the 0,3,1 cavity. Table 2.1b includes all the second harmonic TE _{$m,p,1$} modes in the whispering gallery cavity over the same magnetic field range. Using the TE _{m,p,q} notation, only $q = 1$ modes were considered. Temkin [41] has shown that $Q_D \sim q^{-2}$ for high Q_D cavities, so higher axial modes ($q > 1$) would have substantially reduced diffractive Q 's. It will be evident later in this chapter that these lower Q_D modes will require significantly higher beam currents for the start of oscillation condition and will produce much lower efficiencies. In the overmoded cavities under consideration, these higher order q modes should not be present.

Table 2.1a — 0,3,1 Cavity $\omega \approx 2\omega_c$ CAVRF Results

MODE	FREQUENCY (GHz)	Q_D	\hat{k}_{\parallel} (cm^{-1})
TE _{1,5,1}	203.72	3310	1.537
TE _{13,1,1}	204.61	3350	1.538
TE _{6,3,1}	209.26	3510	1.545
TE _{9,2,1}	209.51	3520	1.545
TE _{4,4,1}	218.78	3870	1.559
TE _{14,1,1}	218.94	3880	1.559
TE _{2,5,1}	224.03	4080	1.566
TE _{10,2,1}	225.40	4140	1.568
TE _{0,5,1}	225.71	4150	1.568
TE _{7,3,1}	226.52	4180	1.569
TE _{15,1,1}	233.24	4460	1.578
TE _{5,4,1}	237.24	4630	1.583
TE _{11,2,1}	241.17	4800	1.587
TE _{8,3,1}	243.55	4910	1.590
TE _{3,5,1}	243.75	4920	1.591
TE _{1,6,1}	246.86	5060	1.594
TE _{16,1,1}	247.51	5090	1.595
TE _{6,4,1}	255.37	5450	1.603
TE _{12,2,1}	256.84	5530	1.605
TE _{9,3,1}	260.39	5700	1.609
TE _{17,1,1}	261.76	5770	1.610
TE _{4,5,1}	263.01	5830	1.611
TE _{2,6,1}	267.35	6040	1.616
TE _{0,6,1}	268.76	6120	1.617
TE _{13,2,1}	272.42	6310	1.621
TE _{7,4,1}	273.22	6360	1.622
TE _{18,1,1}	275.99	6490	1.624
TE _{10,3,1}	277.07	6660	1.625
TE _{5,5,1}	281.89	6820	1.630
TE _{3,6,1}	287.33	7120	1.635
TE _{14,2,1}	287.92	7140	1.635
TE _{1,7,1}	289.95	7260	1.637
TE _{19,1,1}	290.20	7280	1.637
TE _{8,4,1}	290.84	7320	1.638
TE _{11,3,1}	293.60	7470	1.640
TE _{6,5,1}	300.46	7680	1.652
TE _{15,2,1}	303.35	7690	1.660

Table 2.1b — Whispering Gallery Cavity $\omega \approx 2\omega_c$ CAVRF Results

<i>MODE</i>	<i>FREQUENCY (GHz)</i>	Q_D	$\hat{k}_{ }$ (cm^{-1})
TE_{9,1,1}	203.52	689	2.306
TE_{3,3,1}	215.53	755	2.350
TE_{1,4,1}	222.35	798	2.375
TE_{6,2,1}	222.90	796	2.377
TE_{10,1,1}	223.58	804	2.380
TE_{4,3,1}	240.82	909	2.436
TE_{11,1,1}	243.56	926	2.444
TE_{7,2,1}	245.56	936	2.449
TE_{2,4,1}	250.07	962	2.462
TE_{0,4,1}	252.97	981	2.470
TE_{12,1,1}	263.48	1050	2.500
TE_{5,3,1}	265.53	1070	2.504
TE_{8,2,1}	267.96	1080	2.511
TE_{3,4,1}	276.86	1140	2.532
TE_{1,5,1}	282.12	1180	2.545
TE_{13,1,1}	283.35	1180	2.548
TE_{6,3,1}	289.78	1230	2.561
TE_{9,2,1}	290.13	1230	2.561

The possible modes for the given magnetic field range were found by scaling ν_{mp} from a fundamental mode where ν_{mp} represents the p^{th} root of $J'_m(x) = 0$. Here $J'_m(x)$ is the derivative with respect to argument of the Bessel function of order m . The cavity dimensions required as CAVRF input values could not be measured to the desired accuracy, so the CAVRF output frequencies for the second harmonic modes were scaled by the ratio of experimentally measured frequency to CAVRF frequency of a known fundamental mode. The accuracy of the experimental technique discussed in Chapter 3 allowed five significant digits in the scaled CAVRF frequencies tabulated in Tables 2.1a and 2.1b. Since Q_D was not determined experimentally at the fundamental with sufficient accuracy, the direct CAVRF output values of Q_D at the second harmonic are presented in the tables.

— Using CAVRF for the Gaussian Approximation to $f(z)$ —

The final columns in Tables 2.1a and 2.1b are labelled \hat{k}_1 , which represents a parameter required for theories discussed later in this chapter. The field magnitude profile plotted in Figure 2.1 resembles a Gaussian function with some degree of imagination. This Gaussian approximation is used in several theories by substituting the function

$$f(z) = e^{-(2z/L_{\text{eff}})^2} \quad (2.12)$$

for the actual cold cavity $f_c(z)$ solved for by CAVRF. Here L_{eff} represents the effective cavity length, or the full width of the Gaussian function at the $1/e$ point. This is related to the tabulated value of \hat{k}_1 by

$$L_{\text{eff}} = 2/\hat{k}_1 \quad (2.13)$$

The mechanics of calculating the $\hat{k}_{||}$ values involved running CAVRF with 975 data points along the z -axis for sufficient accuracy. The highest three field magnitude values and corresponding z -coordinates were locally fit to a parabola to determine the maximum point and its z -coordinate (z_{\max}). A parabola was then fit to the three points closest to the $1/e$ value of the maximum on the input side, and the z -coordinate ($z_{1/e}$) was determined. The input side was used because the efficiency is known to depend strongly on the RF field profile on the input side and only weakly on the profile on the output side. The $\hat{k}_{||}$ value was then calculated by

$$\hat{k}_{||} = \frac{1}{z_{\max} - z_{1/e}}. \quad (2.14)$$

This value is close but not necessarily the same as the parallel wave number $k_{||}$ expressed as

$$k_{||} = \sqrt{(\omega/c)^2 - k_{\perp}^2}. \quad (2.15)$$

In typical cylindrical resonator geometries,

$$k_{\perp} = \nu_{mp}/r_c \quad (2.16)$$

where r_c is the cavity radius. This implies k_{\perp} is a function of z . As shown in Figure 2.1, the fields are generally confined to the straight, central region of the cavity. In practical calculations of $k_{||}$, it suffices to use the straight section radius in equation (2.16). The condition $k_{\perp}^2 \ll k^2$ implies $(\omega/c)^2 - k_{\perp}^2 \approx k_{||}^2$. For this reason, equation (2.15) is not very useful unless (ω/c) and k_{\perp} are known to unrealistic accuracies. The parameter $\hat{k}_{||}$ described above actually provides a more

reasonable estimation of k_{\parallel} . Unless stated otherwise in this paper, \hat{k}_{\parallel} will be used whenever a value of k_{\parallel} is required.

The CAVRF results provide an adequate starting point estimation of the electromagnetic fields in the resonator. However, gyrotron performance theories require consideration of the energy exchange between the electrons and the fields. The linear theory will serve as a first step in this regard.

2.2 — The Linear Theory of the Gyrotron

To define the linear regime of CRM operation, the electron beam current density \vec{J} is in general not only the unperturbed beam density \vec{J}_0 , but a sum of terms describing the coupling between the beam and electromagnetic fields. That is, $\vec{J} = \vec{J}_0 + c_1 \mathcal{E}(\hat{\mathcal{E}}) + c_2 \mathcal{E}^2(\hat{\mathcal{E}}) + c_3 \mathcal{E}^3(\hat{\mathcal{E}}) + \dots$ where \mathcal{E} is the field amplitude and $\hat{\mathcal{E}}$ a unit vector in the direction of $\vec{\mathcal{E}}$. For small field values, the second order and higher terms may be neglected, reducing \vec{J} to terms linear in \mathcal{E} . Using the output power relation $P_{\text{out}} \sim \int_V \vec{J} \cdot \vec{\mathcal{E}}$, it follows that in the linear limit, $\eta \sim \mathcal{E}^2$.

The small field amplitude condition restricts the range of applicability to the threshold of mode oscillation. The primary application of the linear theory is the calculation of the starting current I_{T} , which is the minimum beam current required for mode initiation. This allows the determination of which modes should be excited at a specific set of experimental operating conditions including beam current I , cathode voltage V_c , and magnetic field value B . The utility of the linear theory is enhanced because it generally results in analytic expressions, as opposed to the nonlinear theory which must be solved numerically.

There have been a number of formulations of the linear theory, differing mainly in their scope of applicability. In 1965, Hirshfield [37] developed a theory for the $TE_{0,1,1}$ mode at the fundamental. Chu's treatment [42], restricted to the azimuthally symmetric $TE_{0,p,q}$ modes, extends the theory to cyclotron harmonics. Temkin et al. [43] derived an expression for I_{τ} at the fundamental for arbitrary $TE_{m,p,q}$ modes. All of these methods assumed a sinusoidal longitudinal distribution of the RF field. The most comprehensive Soviet investigation was performed by Petelin and Yulpatov [44], but a particularly simple yet meaningful expression was reported by Gaponov [45] which will be used extensively later in this section. The Gaponov equation assumes a Gaussian field distribution and yields I_{τ} at the magnetic field value corresponding to the minimum I_{τ} .

This section will outline the development of the linear theory as formulated by Kreischer and Temkin [46]. Their treatment encompasses all TE modes including harmonics, and any longitudinal field profile. Additionally, an arbitrary distribution of electron velocities may be included. In the appropriate limits, their expressions reduce to those results cited earlier. This will be demonstrated explicitly in the case of the Gaponov equation.

— Description of the Linear Analysis —

Several assumptions are necessary in the Kreischer formulation of the linear theory. These include the same condition required by CAVRF that the cavity radius be slowly varying along the z -axis. The electron beam should be weakly relativistic, since the theory only retains the relativistic factor γ in the denominator of ω_c . Space charge effects are neglected as is the interaction between the electrons

and the RF magnetic field. This latter statement eliminates consideration of axial bunching and TM modes as discussed previously.

The derivation is based on the combined Vlasov and Maxwell equations as a foundation for describing the beam and electromagnetic field interaction. Maxwell's equations are solved by a Slater expansion of the fields in terms of orthonormal modes. When the cavity is at equilibrium, the power balance equation may be written

$$\frac{\omega_s}{Q_s} = \frac{1}{\epsilon_0} \operatorname{Re} \left[\frac{1}{\mathcal{P}_s} \int_V d^3r \mathbf{J} \cdot \bar{\mathcal{E}}_s \right] \quad (2.17)$$

where \mathcal{P}_s represents the time independent Slater expansion coefficient for the mode s . The "s" subscripts on ω , Q , and \mathcal{E} indicate that they are also mode dependent. This equation follows from the total Q generalization of equation (2.3). In this case the stored energy $U = (\epsilon_0 \mathcal{P}_s^2 / 2)$ and the total power extracted from the beam is the interaction integral $\frac{\mathcal{P}_s}{2} \int_V \bar{\mathbf{J}} \cdot \bar{\mathcal{E}}_s$. Since (2.17) is applicable at equilibrium, it is representative of the oscillation threshold conditions. Solving the equation for the current yields I_{τ} .

The Vlasov equation is linearized in terms of the fields and electron distribution function. The zero order equation is subtracted from the perturbed equation, and the resulting expression is solved for the perturbed electron distribution function \hat{f}_1 by the method of characteristics. The $\bar{\mathbf{J}}$ in equation (2.17) may then be solved for by the equation

$$\bar{\mathbf{J}} = -e \int d\bar{v} \bar{v} N \hat{f}_1(\bar{v}) . \quad (2.18)$$

The integration in equation (2.18) is over velocity and N is the spatial beam density. The general interaction integral that results from these calculations is quite complicated, involving several geometric factors and functions which are determined by the longitudinal field profile. The general expression will not be presented here.

The derivation at the fundamental assumes that the electron interacts with the field value at the gyrocenter. To extend the theory to include higher harmonics, the field value on the Larmor orbit must be used. To accomplish this, the scalar potential is expanded in terms of four coordinates. These are the cylindrical coordinates azimuthal angle and radius (r_e) of the guiding center, as well as the phase and Larmor radius (r_L) of the electron about the gyrocenter. The transverse field is then determined from the scalar potential and the rest of the derivation remains the same as for the fundamental. Again, the general case will not be shown, but instead the specialized result for an infinitely thin, azimuthally symmetric, annular electron beam with radius r_e is presented.

$$L_{\omega} = \frac{e_e \omega_p^2 2^{\tau} m_e k^2 v}{2\pi Q e G_D} \left(\frac{dJ_n(k, r_L)}{d(k, r_L)} \right)^2 \quad (2.19)$$

$$n \int dv \int dv \hat{f}_0 \left(\frac{v}{v} \right) \left[F_0 - \frac{1}{2} \left(\frac{\omega_e v^2}{k v c^2} \right) \frac{dF_0}{dx} \right]$$

In equation (2.19), \hat{f}_0 is the unperturbed electron distribution, v is the average parallel velocity and all of the mode subscripts have been dropped. The function F_0 depends on the longitudinal field profile function $f(z)$ and may be calculated in terms of the Fourier transform of f with the independent variable x . This x is

known as the detuning parameter and is a measure of the off-resonance condition.

Explicitly, x is defined by

$$x = \frac{n\omega_c - \omega}{k_{\parallel}v_{\parallel}} \quad (2.20)$$

and it may be considered a normalized value of B .

The G_D factor measures the effectiveness of the interaction between the electron beam and the fields. It is evaluated as $G_D = J_{m \pm n}^2(k_{\perp}r_e)$. The “ \pm ” sign is necessary because there is a double degeneracy in the modes with azimuthal mode index $m \neq 0$. This corresponds to two senses of azimuthal rotation of the mode. There is a lack of symmetry in the problem due to the specific direction of rotation of the electrons about the magnetic field lines. Correspondingly, the Bessel function values of $J_{m+n}^2(k_{\perp}r_e)$ and $J_{m-n}^2(k_{\perp}r_e)$ may differ greatly yielding significantly different values of $I_{\pm\tau}$. The degeneracy is not resolved in the azimuthally symmetric ($m = 0$) modes which are standing waves in the azimuthal direction. Mathematically this is realized by $J_{\pm n}^2(k_{\perp}r_e) = J_{\mp n}^2(k_{\perp}r_e)$, thus yielding the same $I_{\pm\tau}$ regardless of sign.

Derivation of the Gaponov Result

Any arbitrary distribution of velocities may be treated in equation (2.19) by specifying \hat{f}_{\pm} . In the case of no velocity spread, \hat{f}_{\pm} becomes the delta function $\hat{f}_{\pm} = \frac{1}{2\pi v_{\parallel\pm}} \delta(v_{\parallel\pm} - v_{\parallel\pm 0}) \delta(v_{\perp\pm} - v_{\perp\pm 0})$, and $\tilde{v}_{\pm} = v_{\pm 0}$. The integral in the denominator of equation (2.19) may now be evaluated.

$$I_{\pm\tau} = \frac{e_0 \gamma m_e \omega \mathcal{P}^{-2}(k_{\parallel}v_{\parallel\pm 0})^2}{e J_{m \pm n}^2(k_{\perp}r_e)} \quad (2.21)$$

$$nQ \left[\frac{1}{2} \left(\frac{\omega_c v_{\parallel\pm 0}^2}{k_{\parallel} v_{\parallel\pm 0} c^2} \right) \frac{dF_{\pm}}{dx} + F_{\pm} \right] \left(\frac{dJ_n(k_{\perp}r_e)}{d(k_{\perp}r_e)} \right)^2$$

Equation (2.21) is now appropriate for a gyrotron magnetron injecton gun producing a perfectly thin, annular electron beam with no velocity spread. To proceed further, the longitudinal field distribution must be specified. By assuming the Gaussian function for $f(z)$ from equation (2.12) and evaluating the expression above at the x value corresponding to the minimum $I_{\perp T}$, the Gaponov equation [45] will result.

As shown in [46], the stored energy \mathcal{P}^2 for a Gaussian profile is

$$\mathcal{P}^2 = \left(\frac{\pi}{2}\right)^{1/2} \frac{L_{\text{eff}}}{2k_{\perp}^2} \left[\nu_{m\perp}^2 - m^2 \right] J_m^2(\nu_{m\perp}). \quad (2.22)$$

Specifying a Gaussian also determines F_c and its derivative with respect to x .

$$F_c = \frac{\pi}{2} e^{-(x/2)^2} \implies \frac{dF_c}{dx} = -\frac{\pi}{2} x e^{-(x/2)^2} \quad (2.23)$$

Dropping the "c" subscripts on ν_{\parallel} and ν_{\perp} , and substituting in expressions (2.22) and (2.23), the equation for $I_{\perp T}$ becomes

$$I_{\perp T} = \frac{e_0 \gamma m_e}{e} \left(\frac{\pi}{2}\right)^{1/2} \left(\frac{L_{\text{eff}} \omega k^2 v^2}{2k_{\perp}^2}\right) \frac{\left[\nu_{m\perp}^2 - m^2 \right] J_m^2(\nu_{m\perp})}{J_{m \pm n}^2(k_{\perp} r_L)} e^{-(x/2)^2} \left[\frac{x}{2} \left(\frac{n\omega}{k v}\right) \beta_{\perp}^2 - n \right] \left(\frac{dJ_n(k_{\perp} r_L)}{d(k_{\perp} r_L)}\right)^2. \quad (2.24)$$

The approximations applicable to gyrotrons, $k^2 \approx k_{\perp}^2$ and $\omega \approx n\omega_c$, permit the substitution $k_{\perp} r_L \approx n\beta_{\perp}$. The small argument approximation for the Bessel function may be used in the weakly relativistic limit to yield

$$\left(\frac{dJ_n(k_{\perp} r_L)}{d(k_{\perp} r_L)}\right)^2 \approx \left(\frac{dJ_n(n\beta_{\perp})}{d(n\beta_{\perp})}\right)^2 \stackrel{n\beta_{\perp} \text{ small}}{\approx} \frac{1}{4} \left(\frac{n^n}{n!}\right)^2 \left(\frac{\beta_{\perp}}{2}\right)^{2(n-1)} \quad (2.25)$$

As discussed in Section 2.1, for the Gaussian $k_{\parallel} = \hat{k}_{\parallel} = L_{\text{eff}}/2$. This relationship with the near cutoff and near resonance approximations allow

$$\left(\frac{L_{\text{eff}} \omega k_{\parallel}^2 v_{\parallel}^2}{2k_{\perp}^2} \right) \approx \frac{c^3}{\pi} \left(\frac{\lambda}{L_{\text{eff}}} \right) \beta_{\parallel}^2 \quad \text{and} \quad \left(\frac{n\omega_c}{k_{\parallel} v_{\parallel}} \right) \approx \frac{\pi}{\beta_{\parallel}} \left(\frac{L_{\text{eff}}}{\lambda} \right). \quad (2.26)$$

Prior to making these substitutions, the normalized cavity length μ and the beam interaction term G will be introduced. These definitions appear in numerous Soviet papers including [8] and [45].

$$\mu \equiv \pi \frac{\beta_{\perp}^2}{\beta} \left(\frac{L_{\text{eff}}}{\lambda} \right) \quad (2.27)$$

$$G \equiv \frac{J_{m \pm n}^2(k_{\perp} r_e)}{[\nu_{mp}^2 - m^2] J_m^2(\nu_{mp})} \quad (2.28)$$

Using equations (2.25) - (2.28), the expression for I_{sT} becomes

$$I_{sT} = \frac{\left[\frac{4\epsilon_0 m_e c^3}{e\sqrt{2\pi}} \right] \gamma \beta_{\parallel}^2}{Q \left(\frac{L_{\text{eff}}}{\lambda} \right) \left(\frac{n^n}{n!} \right)^2 \left(\frac{\beta_{\perp}}{2} \right)^{2(n-1)} G e^{-(x/2)^2} \left[-\frac{x\mu}{2} - n \right]} \quad (2.29)$$

The detuning value which produces the minimum starting current (x_{min}) is determined by taking the derivative of equation (2.29) with respect to x and setting it equal to zero. The resulting value is given by

$$x_{\text{min}} = - \left[\left(\frac{n}{\mu} \right) + \sqrt{\left(\frac{n}{\mu} \right)^2 + 1} \right]. \quad (2.30)$$

Only minor cosmetic changes remain to convert (2.29) to the exact form of the Gaponov equation. These include defining "x Gaponov" (x_g) as

$$x_g \equiv -(x_{\text{min}}/2) - \frac{1}{2} \left[\left(\frac{n}{\mu} \right) - \sqrt{\left(\frac{n}{\mu} \right)^2 + 1} \right], \quad (2.31)$$

and multiplying numerator and denominator by 10^{-3} . Evaluating the numerical factors and physical constants in MKS units yields 2.16 amps when multiplied by the 10^{-3} . It appears that Gaponov combined the 2.16 and γ to get 2.3, which is accurate at $V_c \approx 32$ kV. The following equation is the Gaponov result with definitions (2.27), (2.28) and (2.31).

$$I_{sT}(A) = \frac{(2.3) \beta^2}{(Q \cdot 10^{-3}) \left(\frac{L_{\text{eff}}}{\lambda} \right) \left(\frac{n^n}{n!} \right)^2 \left(\frac{\beta_{\perp}}{2} \right)^{2(n-1)} G e^{-2x_c^2} \mu x_c n} \quad (2.32)$$

— Application of the Linear Theory —

The denominator of the expression above contains the total Q , which may be calculated by equation (2.4). The diffractive Q is obtained from the CAVRF results of Tables 2.1a and 2.1b. Equation (2.33) below yields Q_{ohm} for the cylindrical geometry resonators under consideration.

$$Q_{\text{ohm}} = \frac{r_o}{\delta} \left(1 - \frac{m^2}{\nu_{mp}^2} \right) \quad (2.33)$$

Here r_o is the radius and δ the skin depth of the conducting cavity wall. To present order of magnitude examples of Q_{ohm} for the 0.3.1 cavity, the "volume" modes (radial mode index $p \geq 3$) all had $Q_{\text{ohm}} > 20,000$. The $TE_{m,2,1}$ modes with $m \gg p = 2$ had $Q_{\text{ohm}} \approx 16,000$ and the whispering gallery modes ($TE_{m,1,1}$ with $m \gg 1$) had $Q_{\text{ohm}} \approx 6,000$. These values of Q_{ohm} combined with the values of Q_D ranging from 3310-7680, imply that with the possible exception of the whispering gallery modes with $p = 1$, $Q \approx Q_D$. This serves to justify the previous neglect of higher order axial modes since $I_{sT} \sim Q^{-1} \approx Q_D^{-1} \sim q^2$. With the given

range of Q values, $TE_{m,p,2}$ should have approximately four times the starting current as $TE_{m,p,1}$.

All of the factors appearing in equation (2.32) may now be calculated by the data produced from CAVRF and the specific experimental conditions. The frequency and \hat{k}_{\parallel} from Tables 2.1a and 2.1b yield L_{eff} and λ . An operating voltage of $V_c = 64.3$ kV and the MIT electron gun design value of $(\beta_{\perp}/\beta_{\parallel}) = 1.49$, produces $\beta_{\perp} = 0.383$ and $\beta_{\parallel} = 0.256$. These values permit the calculation of μ by equation (2.27) and x_c by specifying the harmonic number $n = 2$ in equation (2.31). The frequency from CAVRF also appears indirectly in the calculation of Q , by the $\nu^{-\frac{1}{2}}$ dependence of the skin depth δ appearing in equation (2.33) for Q_{ohm} .

The remaining factor in the Gaponov equation (2.32) is the beam interaction parameter G defined by (2.28). The k_{\perp} in the argument of the Bessel function in the numerator of (2.28) is determined by equation (2.16). The specific wall radius values used were $r_o = 0.348$ cm for the 0.3.1 cavity and $r_o = 0.250$ cm for the whispering gallery cavity. Both cavity calculations used a beam guiding center radius of $r_c = 0.197$ cm. The degeneracy in G discussed earlier for the non-azimuthally symmetric modes requires an additional term in the mode notation. In this paper, $TE_{m,p,q(+)}$ refers to the positive sense of rotation and therefore a G calculated with $J_{m+n}^2(k_{\perp} r_c)$, while $TE_{m,p,q(-)}$ is the opposite with G resulting from $J_{m-n}^2(k_{\perp} r_c)$. The azimuthally symmetric modes will remain $TE_{0,p,q}$.

Starting currents were calculated by equation (2.32) for all the modes listed in Tables 2.1a and 2.1b. The results are depicted in graphical form in Figures 2.2a and 2.2b and the actual values are listed in Tables 2.2a and 2.2b.

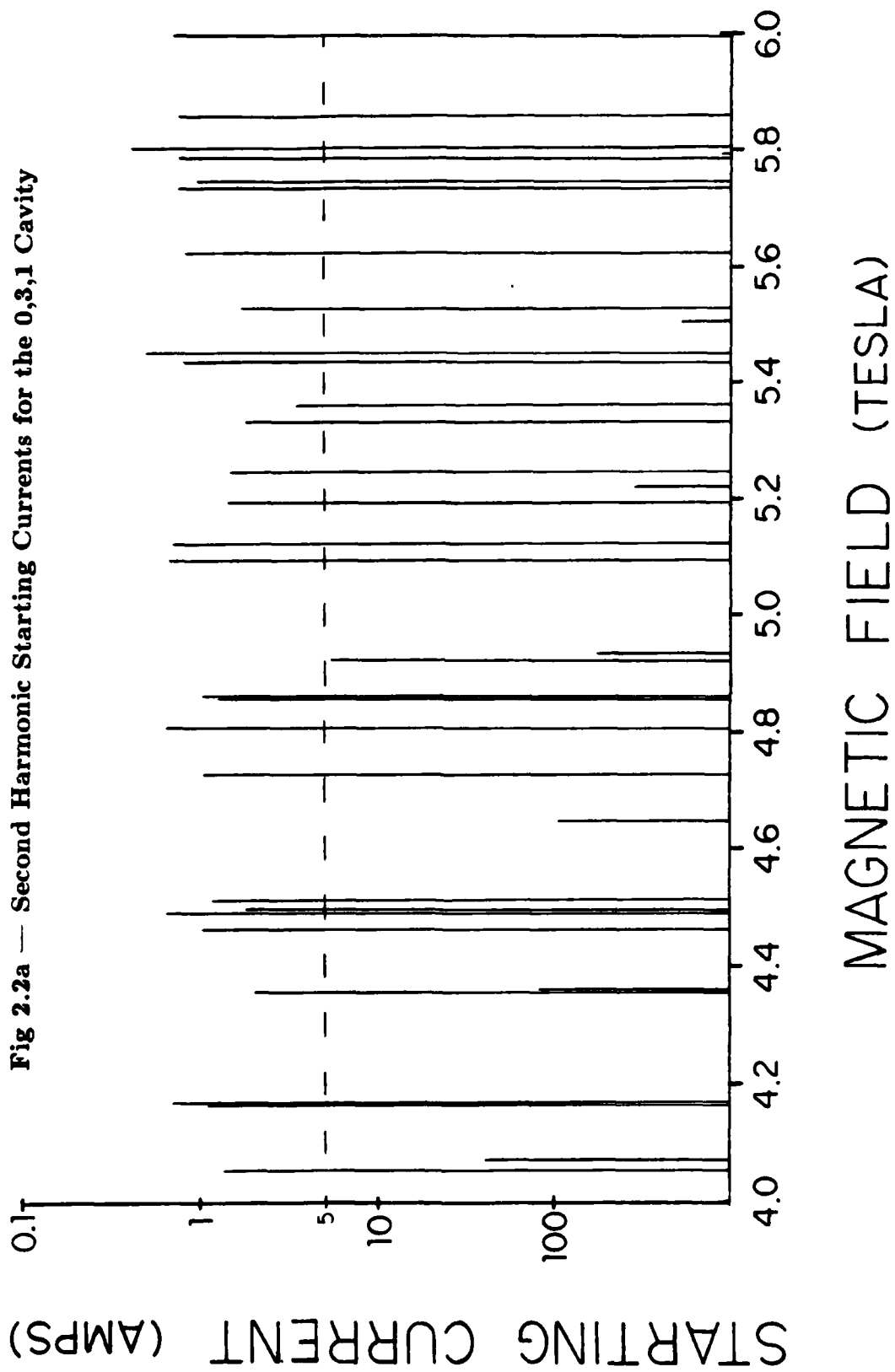


Table 2.2a — 0,3,1 Cavity $\omega \approx 2\omega_c$ Starting Currents

MODE	B (tesla)	Q	L_{eff}/λ	I_{ST} (amps)
TE _{1,5,1(+)}	4.054	2910	8.845	1.4
TE _{13,1,1(-)}	4.072	2120	8.876	41.
TE _{6,3,1(+)}	4.165	3000	9.035	1.1
TE _{9,2,1(-)}	4.170	2880	9.044	0.72
TE _{4,4,1(+)}	4.356	3320	9.364	2.1
TE _{14,1,1(-)}	4.360	2312	9.369	83.
TE _{2,5,1(+)}	4.462	3500	9.545	1.1
TE _{10,2,1(-)}	4.489	3280	9.592	0.66
TE _{0,5,1}	4.496	3560	9.603	1.9
TE _{7,3,1(+)}	4.512	3480	9.630	1.2
TE _{15,1,1(-)}	4.647	2500	9.861	110.
TE _{5,4,1(+)}	4.727	3870	10.00	1.1
TE _{11,2,1(-)}	4.806	3680	10.14	0.66
TE _{8,3,1(-)}	4.854	3970	10.22	1.3
TE _{3,5,1(+)}	4.858	4120	10.22	1.1
TE _{1,6,1(+)}	4.921	4240	10.33	5.6
TE _{16,1,1(-)}	4.934	2680	10.35	180.
TE _{6,4,1(+)}	5.092	4440	10.62	0.68
TE _{12,2,1(-)}	5.121	4090	10.68	0.71
TE _{9,3,1(+)}	5.193	4480	10.80	1.5
TE _{17,1,1(-)}	5.220	2850	10.85	300.
TE _{4,5,1(+)}	5.245	4760	10.89	1.5
TE _{2,6,1(-)}	5.332	4940	11.04	1.8
TE _{0,6,1}	5.361	5000	11.09	3.5
TE _{13,2,1(-)}	5.434	4500	11.21	0.81
TE _{7,4,1(+)}	5.450	5030	11.24	0.50
TE _{18,1,1(-)}	5.506	3000	11.34	660.
TE _{10,3,1(+)}	5.528	5000	11.37	1.7
TE _{5,5,1(-)}	5.625	5420	11.54	0.78
TE _{3,6,1(-)}	5.734	5670	11.73	0.75
TE _{14,2,1(-)}	5.746	4910	11.75	0.97
TE _{1,7,1(-)}	5.787	5780	11.82	0.77
TE _{19,1,1(-)}	5.792	3150	11.83	890.
TE _{8,4,1(+)}	5.804	5630	11.85	0.41
TE _{11,3,1(-)}	5.860	5510	11.94	0.76
TE _{6,5,1(-)}	5.998	5970	12.13	0.72

Fig 2.2b — Second Harmonic Starting Currents for the Whispering Gallery Cavity

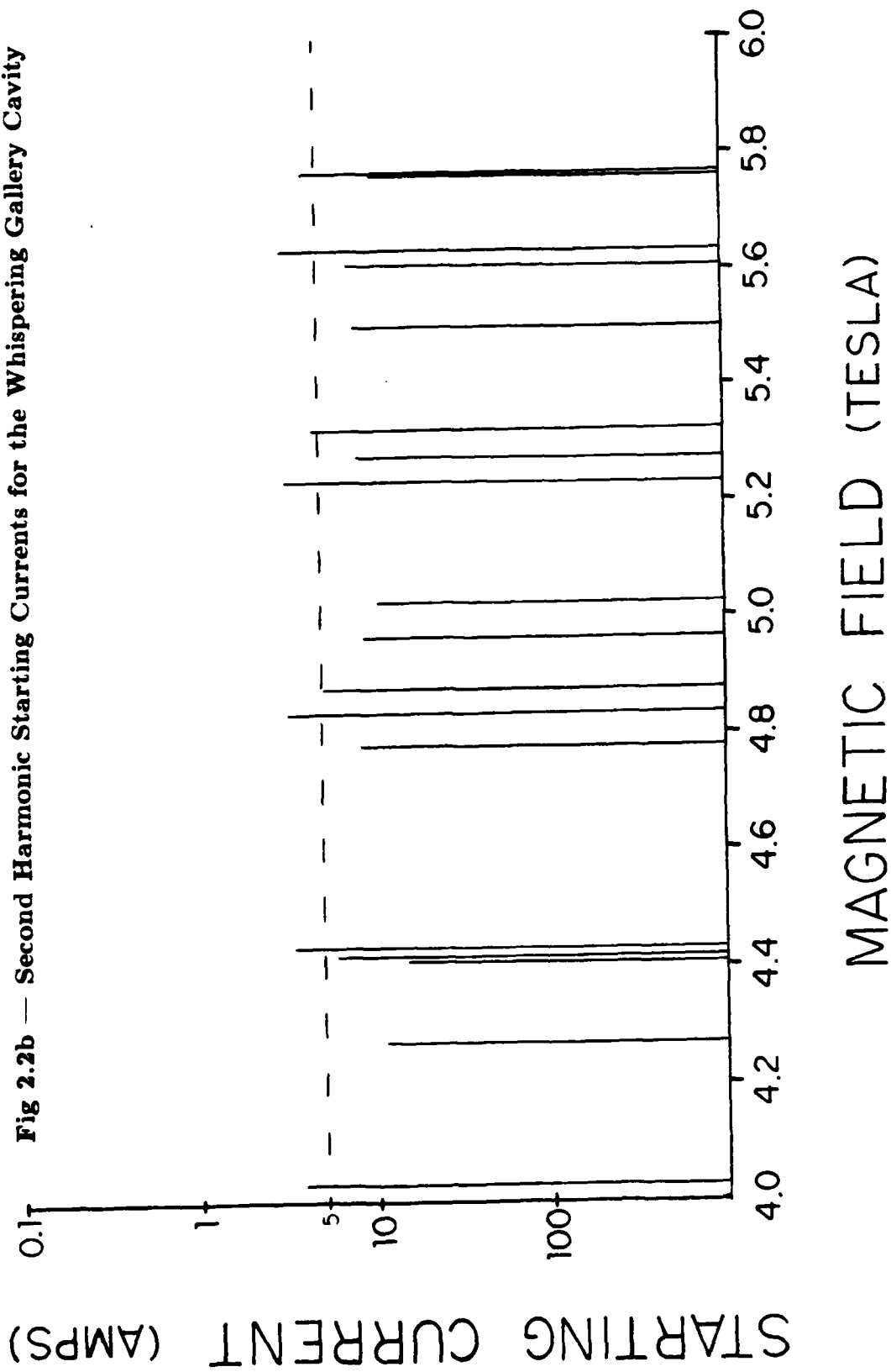


Table 2.2b — Whispering Gallery Cavity $\omega \approx 2\omega_c$ Starting Currents

<i>MODE</i>	<i>B (tesla)</i>	<i>Q</i>	<i>L_{eff}/λ</i>	<i>I_{ST} (amps)</i>
TE_{9,1,1}(-)	4.029	606	5.887	4.0
TE_{3,3,1}(-)	4.270	722	6.118	11.
TE_{1,4,1}(-)	4.407	764	6.244	15.
TE_{6,2,1}(+)	4.418	751	6.257	6.1
TE_{10,1,1}(-)	4.431	693	6.266	3.6
TE_{4,3,1}(-)	4.777	863	6.596	8.6
TE_{11,1,1}(-)	4.832	780	6.648	3.4
TE_{7,2,1}(+)	4.873	875	6.690	5.3
TE_{2,4,1}(-)	4.963	915	6.776	9.0
TE_{0,4,1}	5.021	933	6.832	11.
TE_{12,1,1}(-)	5.232	866	7.032	3.3
TE_{5,3,1}(-)	5.274	1000	7.075	8.4
TE_{8,2,1}(+)	5.322	1000	7.120	4.7
TE_{3,4,1}(-)	5.501	1080	7.296	8.1
TE_{1,5,1}(-)	5.607	1110	7.396	7.5
TE_{13,1,1}(-)	5.632	952	7.420	3.2
TE_{6,3,1}(-)	5.761	1150	7.550	10.
TE_{9,2,1}(+)	5.768	1120	7.556	4.3

In the figures, each vertical line represents an individual mode plotted at the B field value corresponding to x_{\min} . Equation (2.30) determined x_{\min} , and for all modes the value of $x_{\min} \approx -1.1$. This is a result of the one under the square root sign being the dominant term since $\mu \gg n$. The x_{\min} value is converted to B by equations (2.20) and (1.2). The vertical axis has an inverted log scale so the modes with the lowest starting currents appear as the longest lines. The horizontal dashed line represents the experimental operating current of 5 amps. Modes extending above this line should be above threshold. Space did not permit labelling each mode, but correlating the B and I_{sT} values in the accompanying tables allows individual mode identification.

The values presented in Tables 2.2a and 2.2b include the two parameters Q and L_{eff}/λ which were used in equation (2.32). The accuracy in the starting current calculation limits the tabulated values of I_{sT} to two significant digits. Only one sense of mode rotation is listed in the tables. Values of I_{sT} were computed for both “(-)” and “(-)” modes, the result appearing in the tables representing the mode with the lowest I_{sT} . Generally the two calculations yielded values which differed by at least an order of magnitude. The mode with the higher I_{sT} would be in the excitation range of the mode with the lower starting current, and therefore the higher I_{sT} mode should not be present. The 0,3,1 cavity $\text{TE}_{1,5,1}$ was the only mode with the same “(+)” and “(-)” I_{sT} values to two significant figures. The fourth digit resolved the issue in favor of the $\text{TE}_{1,5,1(+)}$ mode, but it would not be considered a reliable distinction.

Examination of Figure 2.2a reveals the overmoded nature of the 0,3,1 cavity. There are 36 modes with $B(x_{\min})$ values between 4.0 and 6.0 tesla. Of these, 28 modes are predicted by the Gaponov equation to be above threshold. The exceptions are the whispering gallery modes, with starting currents ranging from 41 to 890 amps, and the $TE_{1,6,1(+)}$ with $I_{sT} = 5.6$ amps. There are 14 modes listed with a predicted starting current of less than an amp. This would point to the possibility of $TE_{m,p,2}$ modes by the simple scaling of Q values, but the mode density is prohibitive.

By contrast, the whispering gallery cavity spectrum is fairly sparse as seen in Figure 2.2b. This was a design consideration to reduce mode competition at the fundamental. The reduced wall radius limits the number of possible modes to 18 in the 4.0 and 6.0 tesla range. Only seven modes appear above threshold on the plot, those being the whispering gallery modes and two other "surface" modes, the $TE_{8,2,1(+)}$ and the $TE_{9,2,1(+)}$. The range of I_{sT} values is much more limited in this case, with the lowest starting current belonging to the $TE_{13,1,1}$ with 3.2 amps, and the highest starting current corresponding to the $TE_{1,4,1}$ at 15 amps. Although the clean spectrum would appear to allow $q = 1$ modes, the higher starting currents eliminate the possibility. Scaling the $TE_{13,1,1}$ to the $TE_{13,1,2}$ yields $I_{sT} \approx 12$ amps.

The misleading aspect of Figures 2.2a and 2.2b, is the representation of each mode as a delta function in B . In reality, each mode may be excited over a range of B as predicted by equation (2.29) prior to specifying $x = x_{\min}$. There are actually large regions of mode overlap. The B value in Figures 2.2a and 2.2b

at x_{\min} is representative of where the mode should be found experimentally, but this is not precisely accurate. The x_{\min} does not coincide with optimum efficiency which will be discussed in Section 2.3.

The final consideration of the linear theory will provide a more reasonable view of the mode spectrum. This is a computer code developed by Kreischer [47] which provides plots of starting current values as a function of the magnetic field. The program is based on the formulation outlined in this section, restricted to the thin annular electron beam with no velocity spread. An arbitrary longitudinal profile may be chosen and the code allows for higher harmonics. Equation (2.21) is evaluated over the desired range of x after $f(z)$ and n have been specified.

Figures 2.3a and 2.3b are the linear code computer plots of the second harmonic 0.3.1 and whispering gallery cavity spectra over the 4.0 to 6.0 tesla range. The vertical scale is now linear from 0 to 10 amps. The Gaussian field profile was chosen and $n = 2$. To satisfy the computer program input requirements in considering all possible modes, some averaging of several equation parameters such as Q_{dim} and L_{eff} was required. This procedure and the approximations made in the derivation of the Gaponov equation account for the minor L_T differences between Figures 2.2 and 2.3.

The broad range of mode excitation is now evident for the 0.3.1 cavity in Figure 2.3a. Again space on the plot did not allow naming all of the modes, but several of the more isolated and lower starting current modes are labelled. As an example of the discussion concerning the domination of one rotating mode over the opposite rotation, both the $\text{TE}_{4,4,1(-)}$ and $\text{TE}_{4,4,1(+)}$ modes are shown at

Fig 2.3a — $\omega \approx 2\omega_c$ Linear Code Plot of the 0,3,1 Cavity Mode Spectrum

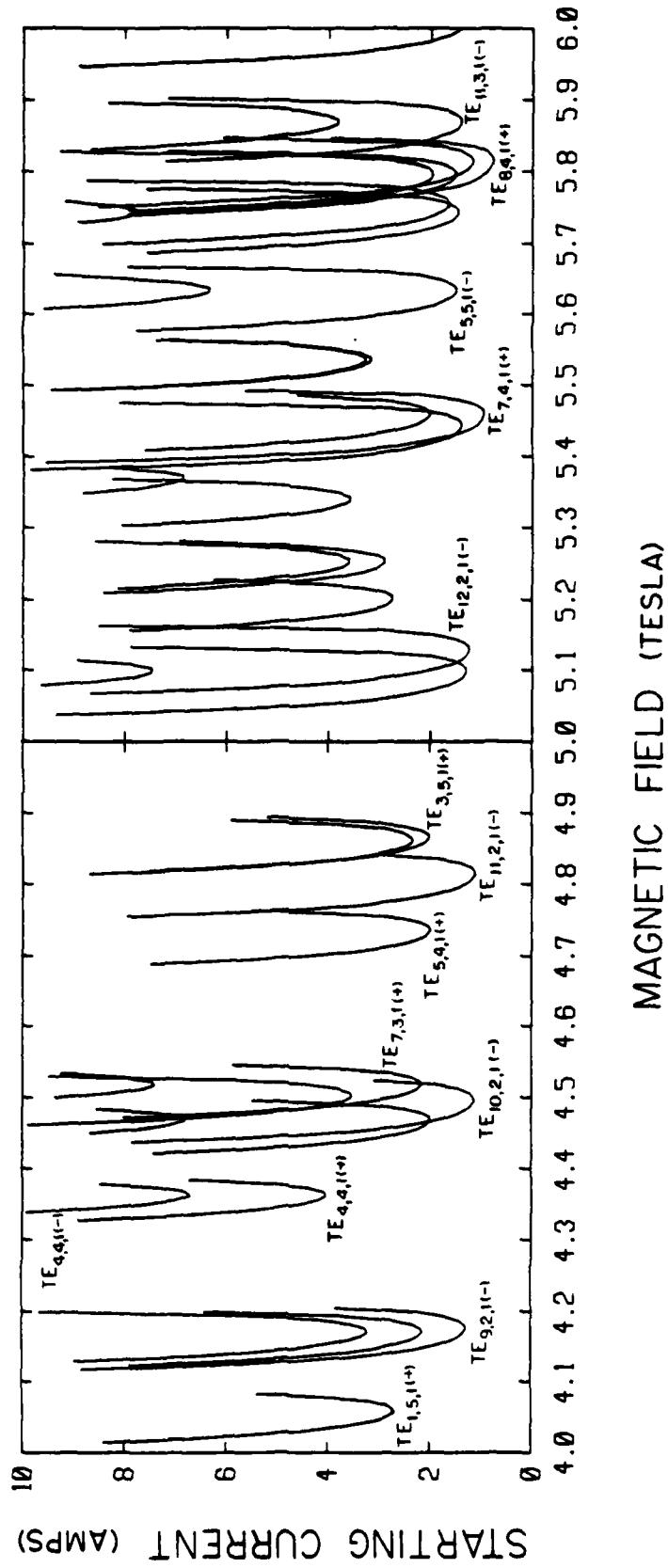
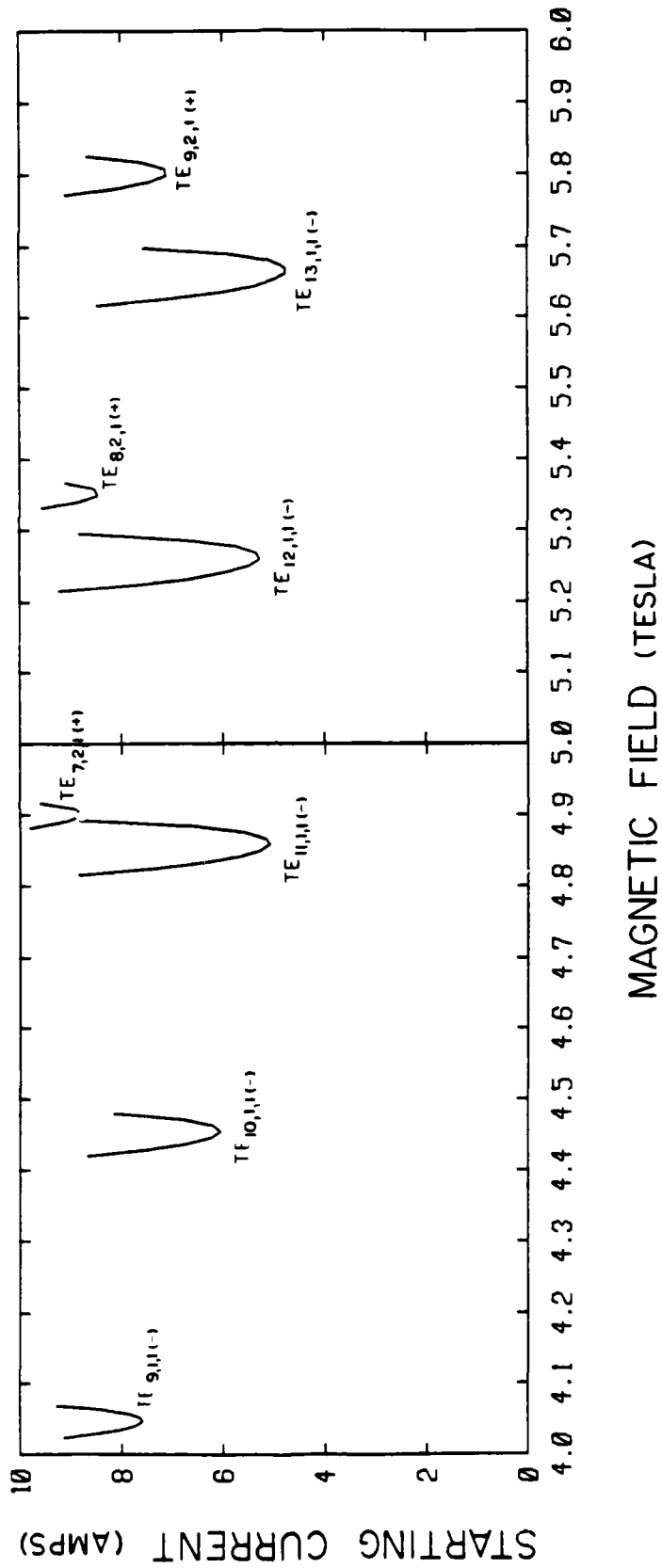


Fig 2.3b — $\omega \approx 2\omega_c$ Linear Code Plot of the Whispering Gallery Cavity Mode Spectrum



about 4.35 tesla. The $TE_{4,4,1(-)}$ lies within the $TE_{4,4,1(+)}$ excitation range at a higher I_{sT} , and should not be experimentally evident. This consideration is applicable to a limited extent between adjacent modes, although mode enhancement or suppression by adjacent modes was not considered in the single mode analysis presented here. Likely examples of this phenomenon are the $TE_{6,3,1(-)}$ and the $TE_{6,3,1(+)}$ which are the unlabelled lines lying within the $TE_{9,2,1(-)}$ excitation zone at about 4.17 tesla. As a first approximation, the $TE_{6,3,1}$ mode would not be expected to appear, though it is shown above threshold on Figure 2.2a.

The whispering gallery plot shown in Figure 2.3b again shows the reduced mode excitation spectrum. The seven modes predicted to be above threshold by the Gaponov calculations are shown as well as the $TE_{7,2,1(+)}$. The discrepancies between the starting current values in the figure and the values in Table 2.2b are accounted for by the parameter averaging procedure which was used to produce computer plots of I_{sT} for all the modes on the same graph.

The mode excitation calculations presented are the most useful aspects of the linear theory. However, theoretical predictions of efficiency and output power require the nonlinear theory applicable beyond the $\eta \sim \xi^2$ regime.

2.3 The Nonlinear Theory of the Gyrotron

Gyrotron operation at optimum detuning and current is generally well beyond the limits of applicability for the linear analysis. Realistic estimates of output power depend on a nonlinear theory.

The slow time scale analysis is based on the work of Soviet theorists. The general derivation is outlined by Flyagin in [48], although the formulation appeared

earlier in [7]. The theory leads to two dimensionless coupled differential equations relating the particle dynamics and the electromagnetic field. The equation describing the electron motion in a combined RF and static magnetic field in the weakly relativistic limit is credited to Yulpatov in several Soviet papers including [49]. B. Danly of the MIT Plasma Fusion Center rederived the equations in terms of the Soviet parameter definitions. His development is reconstructed in the following subsection.

The difficulties inherent in the nonlinear analysis necessitate a single particle approach. This is equivalent to a delta function for the electron velocity distribution function as discussed in the linear theory. Other restrictions include a weakly relativistic beam, again only retaining the γ in the denominator of the cyclotron frequency. Additionally, space charge effects will be neglected.

— *Derivation of the Slow Time Scale Equations* —

The coordinate system remains the same as for the CAVRF description, with the z -axis aligned with the static magnetic field and the gyrocenter as the origin in the x - y plane. The Lorentz force equation for an electron in the RF and static magnetic field is

$$\frac{d\vec{p}}{dt} = -e \left[\vec{\mathcal{E}} + (\vec{v} \times \vec{B}) \right]. \quad (2.34)$$

This equation is separated into perpendicular and parallel components with respect to the z -axis. Neglecting the RF magnetic field, the \vec{B} in equation (2.34) represents the static magnetic field only. The electric field component $\mathcal{E}_z = 0$ for TE modes,

so the parallel component equation yields $p_{\parallel} = \text{constant}$. The equation describing motion in the transverse plane is

$$\frac{d\vec{p}_{\perp}}{dt} + \omega_c (\vec{p}_{\perp} \times \hat{z}) = -e\vec{\mathcal{E}} \quad (2.35)$$

where \vec{p}_{\perp} is the nonrelativistic perpendicular momentum $m\vec{v}_{\perp}$. The position and momentum vectors may be written in terms of complex variables R and P defined

$$\vec{p}_{\perp} = P - p_{\perp} e^{i\varphi} \quad \text{and} \quad \vec{r} = R = r_{\perp} e^{i(\varphi - \pi/2)} \implies R = -\frac{iP}{m_e\omega_c}. \quad (2.36)$$

The $\pi/2$ phase difference between R and P is representative of the circular motion about the gyrocenter. The perpendicular equation of motion (2.35) is now written

$$\frac{\partial P}{\partial t} - i\omega_c P = -e\vec{\mathcal{E}}. \quad (2.37)$$

The fields must be converted to a complex notation. With the condition of a slowly varying radius along the z -axis condition, the fields are separated into longitudinal and transverse components by $\vec{\mathcal{E}}(x, y, z, t) = \text{Re} [f(z)\vec{E}_s(x, y)e^{i\omega t}]$. For TE modes, the transverse field components (\vec{E}_s) are derivable from the scalar function Ψ_s ,

$$\vec{E}_s = \hat{z} \times \nabla_{\perp} \Psi_s \quad \text{where } \Psi_s \text{ satisfies } \nabla_{\perp}^2 \Psi_s + k_{\perp}^2 \Psi_s = 0 \quad (2.38)$$

The function Ψ_s may be expanded in a Fourier series in terms of an angular variable θ about the axis of gyration.

$$\Psi_s = \sum_{\ell} w_{\ell}(r) e^{-i\ell\theta} \quad (2.39)$$

Using Flyagin's notation, the part of the field moving in synchronism with the electron and therefore interacting the most efficiently is \vec{E}_{synch} which rotates at the n^{th} harmonic of ω_c .

$$\vec{E}_{synch} = \hat{z} \times \nabla_{\perp} \Psi_n \quad (2.40)$$

Here the Ψ_n is given by $\Psi_n = \psi_n e^{-in\theta}$ which may be expressed as

$$\Psi_n = A_n r^n e^{-in\theta} = A_n (R^*)^n . \quad (2.41)$$

The R in the equation above is the complex position coordinate defined in (2.36). The field phase θ measured from the x -axis may coincide with an arbitrary initial electron phase $\varphi = \pi/2$ because there will be an ensemble average over φ in the efficiency determination. The complex form of the equation (2.38) combined with equation (2.41) yields

$$\vec{E}_{synch} = -i\nabla_{\perp} \Psi_n = -iA_n \nabla (R^*)^n . \quad (2.42)$$

The goal is to find an applicable complex form of $\vec{\mathcal{E}}(x, y, z, t)$ written as $f(z)E'_z e^{i\omega t}$. With $f(z)$ real, E'_z must be chosen to satisfy the following two conditions which leads to the stated result.

$$\left. \begin{array}{l} \vec{\mathcal{E}} \cdot \hat{x} = f(z) \text{Re}(E'_z e^{i\omega t}) \\ \vec{\mathcal{E}} \cdot \hat{y} = f(z) \text{Im}(E'_z e^{i\omega t}) \end{array} \right\} \rightarrow E'_z = \vec{E}_{synch} \cdot \hat{x} = -iA_n n (R^*)^{n-1} \quad (2.43)$$

Writing the position variable R in terms of P by the relation (2.36) and substituting in for \vec{E} on the right side of equation (2.37) produces the equation

$$\frac{\partial P}{\partial t} - i\omega_c P = \frac{ei^n A_n n}{(m_e \omega_c)^{n-1}} (P^{n-1})^* f e^{i\omega t} . \quad (2.44)$$

The complex momentum P may be converted to the slow time scale momentum p by the relation

$$P = pe^{+i(\omega/n)t}. \quad (2.45)$$

Combining this with Flyagin's definition of ξ

$$\xi \equiv \frac{ei^n A_n n}{(m_e \omega_c)^{n-1}} \quad (2.46)$$

yields the slow time scale equation

$$\frac{\partial p}{\partial t} - i \left(\frac{\omega}{n} - \omega_c \right) p = \xi (p^{n-1})^* f. \quad (2.47)$$

The equation is written in dimensionless form by converting to the dependent variable q and the independent variable ζ defined by

$$q \equiv \frac{p}{p^{(o)}} \quad \text{and} \quad \zeta \equiv \frac{\beta_{\perp}^{(o)2} \omega_c^{(o)} z}{2 v_{\parallel}^{(o)}}. \quad (2.48)$$

The dimensionless q represents the momentum normalized to its value at the start of the interaction region. All of the "(o)" superscripts indicate the parameter value prior to the interaction. This is a necessary distinction since γ is changing throughout the cavity. The normalized longitudinal coordinate ζ is related to μ defined in equation (2.27) by $\zeta = (z/L_{\text{eff}})\mu$.

Equation (2.47) in terms of these dimensionless variables is

$$\frac{\partial q}{\partial \zeta} - i \left[\frac{2}{\beta_{\perp}^{(o)2} \omega_c^{(o)}} \left(\frac{\omega}{n} - \omega_c \right) \right] q = i(q^*)^{n-1} \mathcal{F} \quad (2.49)$$

where

$$\mathcal{F} = i\xi |p^{(o)}|^{n-2} \left(\frac{2}{\beta_{\perp}^{(o)2} \omega_c^{(o)}} \right) f. \quad (2.50)$$

The bracketed term on the left side of equation (2.49) may be simplified by the following approximations and the definition of the Soviet detuning parameter Δ . Since p_{\parallel} is constant, $\gamma^{(o)}\beta_{\parallel}^{(o)} = \gamma\beta_{\parallel}$. The weakly relativistic approximation combined with $\omega \approx n\omega_c$ allows

$$\left[\frac{2}{\beta_{\perp}^{(o)2}\omega_c^{(o)}} \left(\frac{\omega}{n} - \omega_c \right) \right] = \Delta + |q|^2 - 1. \quad (2.51)$$

The Δ is a measure of the off resonance condition and is defined explicitly as

$$\Delta \equiv \frac{2}{\beta_{\perp}^{(o)2}} \left(\frac{\omega - n\omega_c^{(o)}}{\omega} \right) \implies \Delta = -\frac{2x}{\mu}. \quad (2.52)$$

The statement after the arrow relates Δ to the detuning parameter x and the normalized cavity length μ introduced previously.

The derivation is now complete to present the Yulpatov equation in the form appearing in [48].

$$\frac{\partial q}{\partial \zeta} + i(\Delta + |q|^2 - 1)q = i(q^*)^{n-1} \mathcal{F} \quad (2.53)$$

This equation describes the electron dynamics during the interaction. To describe the fields, Maxwell's equations may be used to arrive at

$$\frac{d^2 f}{dz^2} + k_{\parallel}^2 f = \frac{i}{N_s} \int dx dy \vec{J}_{\omega} \cdot \vec{E}_s \quad (2.54)$$

where

$$N_s = \frac{\omega}{4\pi} \int dx dy |\Psi_s|^2 \quad \text{and} \quad \vec{J}_{\omega} = \frac{1}{2\pi} \int_0^{2\pi} \vec{J}(t) e^{-i\omega t} d(\omega t). \quad (2.55)$$

Assuming an infinitely thin beam at $r = r_e$, the transverse current density may be written in terms of the charge density $\rho = -I/v_{\parallel}$.

$$\vec{J}_{\perp}(t) = \rho \frac{P}{m_e} \delta(r - r_e) \quad (2.56)$$

This combined with $\vec{E}_s = E'_s$ given in equation (2.43) yields

$$\frac{i}{N_s} \int dx dy \vec{J}_\omega \cdot \vec{E}'_s = \chi \langle P^n e^{-i\omega t} \rangle_{\omega t_0} \quad (2.57)$$

Here the " $\langle \dots \rangle_{\omega t}$ " represents the integral of the bracketed quantity with respect to ωt over a period, divided by 2π . The substitution $t \rightarrow t_0$, where t_0 represents the time that the interaction begins, is permissible because the $v_{||}$ determining ρ is a constant. The χ in equation (2.57) is defined as

$$\chi = i \frac{\rho A_n^2 n \omega_c}{N_s (i m_e \omega_c)^n} \quad (2.58)$$

Equation (2.54) now becomes

$$\frac{d^2 f}{dz^2} + k_{||}^2 f = \chi \langle P^n e^{-i\omega t} \rangle_{\omega t_0} = \chi \langle p^n \rangle_{\omega t_0} \quad (2.59)$$

the last step a result of converting to the slow time scale defined by equation (2.45). All that remains is changing to the normalized variables q and ζ . Omitting the algebra, the resulting equation is

$$\frac{\partial^2 f}{\partial \zeta^2} + \sigma^2 f = I \langle q^n \rangle_{\omega t_0} \quad (2.60)$$

Here the dimensionless current I and σ are normalization factors,

$$\sigma = \frac{2}{\beta^{(0)2}} \frac{k_{||} v}{\omega_c^{(0)}} \quad \text{and} \quad I = \frac{8eIv}{N_s \beta^{(0)2} \omega_c^{(0)3} m_e} n^2 A_n^2 r^{(0)2(n-1)} \quad (2.61)$$

The $r^{(0)}$ in the definition of I is the slow time scale equivalent of R defined in equation (2.36). The primary results of the slow time scale derivation are now restated.

$$\frac{\partial q}{\partial \zeta} + i(\Delta + |q|^2 - 1)q = i(q^*)^{n-1} \mathcal{F} \quad (2.62)$$

$$\frac{\partial^2 f}{\partial \zeta^2} + \sigma^2 f = I \langle q^n \rangle_{wt.} \quad (2.63)$$

These two equations are coupled by the f which is in the definition of \mathcal{F} in the first equation and the explicit appearance of q in the second. Equation (2.63) is the generalization with a source term of expression (2.8) solved for by CAVRF. Since $q(\zeta)$ represents the normalized momentum of the electron as it traverses the resonator, $|q(\zeta_{\text{out}})|^2$ represents the energy lost by the electron at the completion of the interaction. An ensemble average over the input phases of the electrons will produce the perpendicular efficiency by the relation

$$\eta_{\perp} = 1 - \frac{1}{2\pi} \int_0^{2\pi} d\varphi_o |q(\zeta_{\text{out}})|^2 \quad (2.64)$$

where the integration variable φ_o represents the input phase in the boundary condition $q^{(o)} = e^{i\varphi_o}$. The electronic efficiency η_{el} and the output efficiency η are then calculated by equations (2.5) and (2.6).

Application of the Slow Time Scale Theory --

The intractable nature of coupled differential equations requires a numerical analysis, and most theories make further approximations to reduce equations (2.62) and (2.63). A particularly useful approach was formulated by G. S. Nusinovich and R. E. Erm [8]. Their simplification was based on the premise that for high Q cavities, the longitudinal profile function $f(z)$ is fixed by the cavity profile. For most applications, the Gaussian function specified by equation (2.12) will provide the approximation for $f(z)$. In terms of the normalized parameters

$$f(\zeta) = e^{-(2/\mu)^2 \zeta^2} \quad (2.65)$$

This approximation, discussed extensively in deriving the Gaponov equation in Section 2.2, eliminates the consideration of equation (2.63) altogether. The result is a single, first order differential equation which may be integrated numerically.

The equation treated by Nusinovich and Erm was of the same form as (2.62), but differed slightly in the definitions. The exact equation listed in their 1972 paper is

$$\frac{da}{d\zeta} - \frac{i}{n} (\Delta + |a|^2 - 1)a = ia^{n-1} f(\zeta) F . \quad (2.66)$$

The definitions of ζ , μ and Δ remain the same, but the F which appears in the same position as Flyagin's \mathcal{F} from (2.50), is defined by

$$F = \frac{A}{B} \beta^{n-4} \left(\frac{n^{n-1}}{2^n - 2n!} \right) J_{m \pm n}(k_{\perp} r_c) . \quad (2.67)$$

The field equation equivalent to (2.63) is not listed in their paper because they have assumed a Gaussian for $f(\zeta)$, but the normalization leads to a definition of their dimensionless current I_0 , different from the I appearing in Flyagin's analysis.

$$I_0 = 0.24 I (Q \cdot 10^{-3}) \left(\pi \frac{\beta_{\perp}}{\beta} \right)^{2(3-n)} \left(\frac{L_{\text{eff}}}{\lambda} \right)^{5-2n} \left(\frac{n^n}{2^n n!} \right)^2 G \quad (2.68)$$

The G is the same beam interaction term defined by equation (2.28) which appears in the Gaponov linear theory equation. The expression for I_0 is dimensionless for a beam current I in amps.

The results of the work by Nusinovich and Erm were plots of η_{\perp} and optimum detuning Δ_{opt} over ranges of the parameters F , μ and I_0 . This was accomplished by specifying a value of F , μ and Δ , then integrating equation (2.66) over the range of ζ from $-\frac{\sqrt{3}}{2}\mu$ to $+\frac{\sqrt{3}}{2}\mu$. The parameters were held fixed while the integration

was performed 32 times with separate input phase φ_0 values. This allowed a numerical integration of equation (2.64) and calculation of η_{\perp} . The procedure was repeated varying only the Δ in equation (2.66) until the value of Δ which produced the highest efficiency (Δ_{opt}) was located. By running the algorithm for many values of F and μ , isoefficiency curves and the values of Δ_{opt} were plotted against F and μ . At each value of F , μ , and η_{\perp} corresponding to Δ_{opt} , the value of I_0 was computed by the equation

$$I_0 = F^2 \eta_{\perp}^{-1} \mu^{2(3-n)}, \quad (2.69)$$

which is derived by equating the RF power gain and the power given up by the beam. The generated graphs of η_{\perp} and Δ_{opt} against specific values of I_0 and μ are extremely useful in predicating gyrotron efficiencies at particular operating conditions.

Figure 2.4a is the plot of η_{\perp} and Δ_{opt} as a function of I_0 and μ which resulted from the integrations at the harmonic value of $n = 2$. Figure 2.4b is the same type of graph but differs by the integration length used. A greater extent of the Gaussian profile function is included on the cavity input side in the data represented by Figure 2.4b, by integrating ζ from $-\sqrt{3}\mu$ to $+\frac{\sqrt{3}}{2}\mu$. Both results are credited to Nusinovich and Erm, Figure 2.4a is from their 1972 paper [8], and Figure 2.4b was included in the publication by Gaponov et al. [45]. Both figures have linear scales on the horizontal axis for μ and log scales on the vertical axis for I_0 , but caution should be used in comparing values directly because the relative scales are not the same.

Fig 2.4a — $\omega \approx 2\omega_c$ Isoefficiency Curves
Nusinovich and Erm — 1972

Integration Length of $-\frac{\sqrt{3}}{2}\mu \leq \zeta \leq +\frac{\sqrt{3}}{2}\mu$

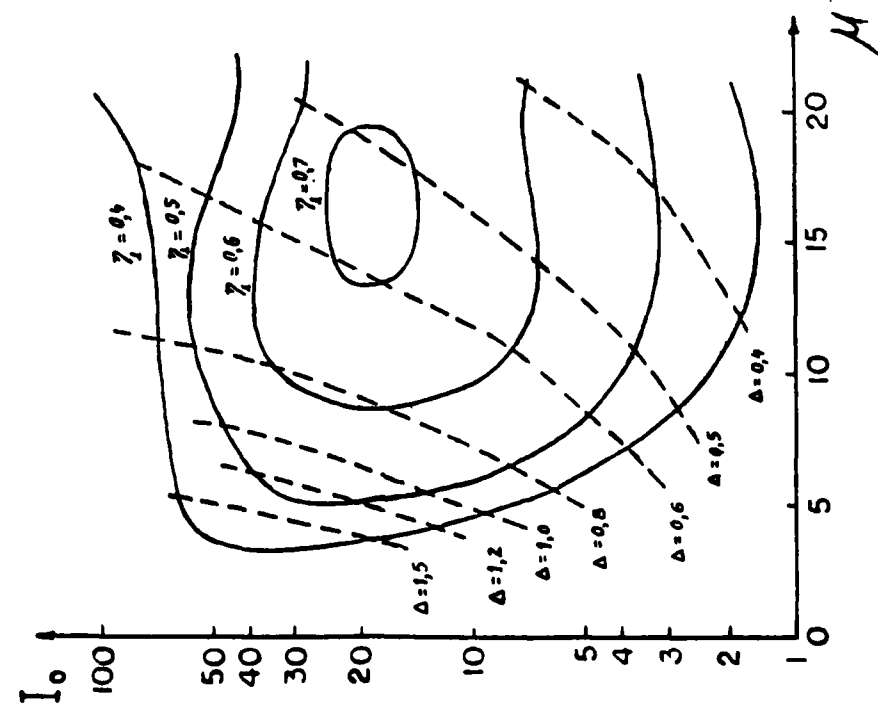
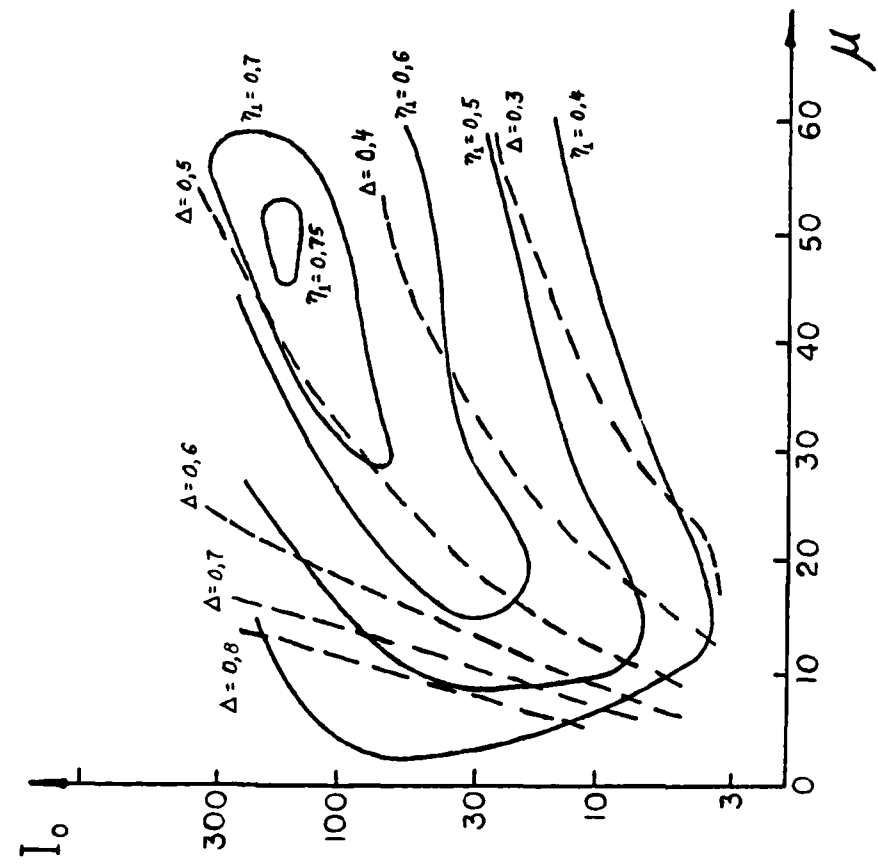


Fig 2.4b — $\omega \approx 2\omega_c$ Isoefficiency Curves
Nusinovich and Erm — 1975

Integration Length of $-\sqrt{3}\mu \leq \zeta \leq +\frac{\sqrt{3}}{2}\mu$



The isoefficiency curves are labelled by their η_{\perp} values. The dashed lines represent the Δ_{opt} value which yielded the given η_{\perp} . The highest efficiency predicted at the second harmonic by Figure 2.4a is 72% corresponding to $I_o \approx 20$ and $\mu \approx 18$. The highest η_{\perp} shown in Figure 2.4b is 76%, but it occurs at $I_o \approx 200$ and $\mu \approx 50$. The higher efficiency in this region by the second graph is a result of the longer field interaction on the input end prebunching the electron beam and enhancing efficiency. However, in gyrotron design considerations, the long cavity lengths described by this large value of μ are unattractive because $Q_D \sim \mu^2$, and the higher overall Q values reduce the output efficiency η by the relationship (2.5).

In practice, the specific operating conditions and cavity length determine I_o and μ which are then used to calculate η_{\perp} and Δ_{opt} from the figures. In the present study, efficiency calculations were made for all of the second harmonic modes predicted to be above threshold by the linear analysis. The results of those calculations are presented in Tables 2.3a - 2.4b. The shorter integration length in Figure 2.3a generated the values presented in the first set of tables. Table 2.3a is for the 0.3,1 cavity and Table 2.3b is the whispering gallery cavity data. The longer integration length represented in Figure 2.3b was used to compute efficiencies in Tables 2.4a and 2.4b.

The values of μ ranged from 15.8 to 21.7 for the modes evaluated in the 0,3,1 cavity. The whispering gallery modes with a shorter L_{eff} , produced μ values from 10.5 to 13.6. The parameter I_o was calculated by equation (2.68) for a beam current of 5 amps. As shown in the tables, the resulting values of I_o ranged from 0.4 to 3.2 in the 0,3,1 cavity and from 0.52 to 0.81 in the whispering gallery

Table 2.3a — 0,3,1 Cavity $\omega \approx 2\omega_c$ Efficiency Calculations

Nusinovich and Erm — 1972

Integration Length of $-\frac{\sqrt{3}}{2}\mu \leq \zeta \leq +\frac{\sqrt{3}}{2}\mu$

<i>MODE</i>	μ	I_c	F	Δ_{opt}	η_{\perp} (%)	η (%)
TE _{1,5,1(+)}	15.79	1.3	0.042	0.31	33	20
TE _{6,3,1(+)}	16.13	1.6	0.047	0.33	37	22
TE _{9,2,1(-)}	16.15	2.5	0.066	0.37	46	26
TE _{4,4,1(+)}	16.72	0.81	0.026	0.18	23	14
TE _{2,5,1(+)}	17.04	1.6	0.045	0.32	37	22
TE _{10,2,1(-)}	17.13	2.5	0.063	0.37	46	25
TE _{0,5,1}	17.15	0.90	0.027	0.19	24	14
TE _{7,3,1(+)}	17.19	1.4	0.041	0.30	35	20
TE _{5,4,1(+)}	17.85	1.5	0.041	0.31	36	21
TE _{11,2,1(-)}	18.10	2.4	0.057	0.35	44	23
TE _{8,3,1(+)}	18.24	1.2	0.034	0.30	33	18
TE _{3,5,1(+)}	18.25	1.4	0.039	0.30	36	21
TE _{6,4,1(+)}	18.97	2.2	0.051	0.34	42	24
TE _{12,2,1(-)}	19.06	2.1	0.049	0.33	42	21
TE _{9,3,1(+)}	19.28	0.99	0.027	0.18	28	15
TE _{4,5,1(+)}	19.44	0.96	0.024	0.25	24	14
TE _{2,6,1(-)}	19.71	0.77	0.021	0.24	24	13
TE _{0,6,1}	19.80	0.40	0.011	0.15	18	9.9
TE _{13,2,1(-)}	20.02	1.7	0.040	0.31	38	19
TE _{7,4,1(-)}	20.07	2.8	0.056	0.35	46	25
TE _{10,3,1(-)}	20.31	0.79	0.024	0.20	30	16
TE _{5,5,1(-)}	20.60	1.7	0.039	0.29	38	21
TE _{3,6,1(-)}	20.94	1.8	0.039	0.29	38	21
TE _{14,2,1(-)}	20.98	1.3	0.032	0.23	34	16
TE _{1,7,1(-)}	21.10	1.7	0.038	0.29	37	20
TE _{8,4,1(+)}	21.16	3.2	0.053	0.35	48	25
TE _{11,3,1(-)}	21.32	1.7	0.037	0.29	38	19
TE _{6,5,1(-)}	21.66	1.8	0.038	0.31	38	21

Table 2.3b — Whispering Gallery Cavity $\omega \approx 2\omega_c$ Efficiency Calculations

Nusinovich and Erm — 1972

Integration Length of $-\frac{\sqrt{3}}{2}\mu \leq \zeta \leq +\frac{\sqrt{3}}{2}\mu$

<i>MODE</i>	μ	I_o	F	Δ_{opt}	η_{\perp} (%)	η (%)
TE_{9,1,1(-)}	10.56	0.81	0.025	0.28	8.5	5.1
TE_{10,1,1(-)}	11.24	0.81	0.027	0.28	12	6.9
TE_{11,1,1(-)}	11.92	0.80	0.028	0.27	13	7.8
TE_{12,1,1(-)}	12.61	0.77	0.026	0.26	14	8.1
TE_{8,2,1(+)}	12.77	0.52	0.0089	0.21	2.4	1.6
TE_{13,1,1(-)}	13.31	0.73	0.024	0.25	14	8.0
TE_{9,2,1(+)}	13.55	0.53	0.012	0.21	4.8	3.1

Table 2.4a — 0,3,1 Cavity $\omega \approx 2\omega_c$ Efficiency Calculations

Nusinovich and Erm — 1975

Integration Length of $-\sqrt{3}\mu \leq \zeta \leq +\frac{\sqrt{3}}{2}\mu$

<i>MODE</i>	μ	I_o	F	Δ_{opt}	η_{\perp} (%)	η (%)
TE _{1,5,1(-)}	15.79	1.3	0.041	0.30	32	19
TE _{6,3,1(+)}	16.13	1.6	0.046	0.31	35	21
TE _{9,2,1(-)}	16.15	2.5	0.064	0.35	43	24
TE _{4,4,1(-)}	16.72	0.81	0.026	0.19	23	14
TE _{2,5,1(-)}	17.04	1.6	0.044	0.30	36	21
TE _{10,2,1(-)}	17.13	2.5	0.061	0.35	43	23
TE _{0,5,1}	17.15	0.90	0.027	0.23	24	14
TE _{7,3,1(-)}	17.19	1.4	0.040	0.29	34	19
TE _{5,4,1(+)}	17.85	1.5	0.040	0.29	34	20
TE _{11,2,1(-)}	18.10	2.4	0.055	0.34	41	22
TE _{8,3,1(-)}	18.24	1.2	0.033	0.25	31	17
TE _{3,5,1(+)}	18.25	1.4	0.038	0.28	34	20
TE _{6,4,1(-)}	18.97	2.2	0.049	0.32	40	22
TE _{12,2,1(-)}	19.06	2.1	0.047	0.31	39	20
TE _{9,3,1(+)}	19.28	0.99	0.028	0.17	30	16
TE _{4,5,1(-)}	19.44	0.96	0.027	0.29	28	16
TE _{2,6,1(-)}	19.71	0.77	0.023	0.19	28	16
TE _{0,6,1}	19.80	0.40	0.016	0.13	26	14
TE _{13,2,1(-)}	20.02	1.7	0.039	0.30	36	18
TE _{7,4,1(+)}	20.07	2.8	0.054	0.33	42	23
TE _{10,3,1(+)}	20.31	0.79	0.023	0.18	28	15
TE _{5,5,1(-)}	20.60	1.7	0.038	0.29	36	19
TE _{3,6,1(-)}	20.94	1.8	0.038	0.28	36	20
TE _{14,2,1(-)}	20.98	1.3	0.031	0.21	32	15
TE _{1,7,1(-)}	21.10	1.7	0.036	0.28	35	19
TE _{8,4,1(+)}	21.16	3.2	0.055	0.33	43	23
TE _{11,3,1(-)}	21.32	1.7	0.036	0.27	35	18
TE _{6,5,1(-)}	21.66	1.8	0.036	0.29	35	19

Table 2.4b — Whispering Gallery Cavity $\omega \approx 2\omega_c$ Efficiency Calculations

Nusinovich and Erm — 1975

Integration Length of $-\sqrt{3}\mu \leq \zeta \leq +\frac{\sqrt{3}}{2}\mu$

<i>MODE</i>	μ	I_o	F	Δ_{opt}	η_{\perp} (%)	η (%)
TE_{9,1,1(-)}	10.56	0.81	0.026	0.28	9.1	5.5
TE_{10,1,1(-)}	11.24	0.81	0.028	0.27	12	7.2
TE_{11,1,1(-)}	11.92	0.80	0.028	0.26	14	8.1
TE_{12,1,1(-)}	12.61	0.77	0.027	0.25	15	8.3
TE_{8,2,1(-)}	12.77	0.52	0.010	0.20	3.1	2.0
TE_{13,1,1(-)}	13.31	0.73	0.025	0.25	15	8.2
TE_{9,2,1(-)}	13.55	0.53	0.013	0.20	6.0	3.8

cavity. From the isoefficiency plots, it is evident that the optimum efficiency at the second harmonic in the $10 \leq \mu \leq 20$ range occurs at values of $I_o \approx 20$. Since $I_o \sim I$, the optimum efficiency would require an order of magnitude increase in beam current.

These low values of I_o which model the experimental investigation require a large degree of interpolation in using the graphs. The problem is most obvious for the $I_o < 1$ situations, which would plot below the horizontal axis in Figures 2.4a and 2.4b. The solution was a computer code developed by B. Danly at the MIT Plasma Fusion Center which solved the differential equation (2.66) in terms of the same parameters defined in (2.67) - (2.69). There are two versions of the code to allow investigation of both integration lengths discussed previously, and 32 steps are included in the integration over input phases. The program reproduces the Nusinovich and Erm results, but is more flexible by allowing investigation over selected ranges of F , μ and I_o , with results available in either tabulated or graphic form. This code produced all of the values of η_{\perp} listed in Tables 2.3a - 2.4b. The last column in each table lists the output efficiency η , related to η_{\perp} by equations (2.5) and (2.6).

The largest value of η_{\perp} listed in Table 2.3a for the 0,3,1 cavity is the $TE_{0,4,1(+)}$ at 48% with the lowest efficiency belonging to the $TE_{0,0,1}$ with $\eta_{\perp} = 18\%$. In contrast, the whispering gallery cavity results for the short integration length show $2.4\% < \eta_{\perp} < 14\%$. This difference in second harmonic mode efficiencies would be expected from the linear results, where the stronger modes in the 0,3,1 cavity had $I_{sT} \approx 0.5$ amps and for the whispering gallery cavity $I_{sT} \approx 3.5$ amps.

Comparison of the results between the two integration lengths reveals that the differences in η_{\perp} are generally limited to less than 3%. Specific trends indicate that the isoefficiency contours are more closely spaced for the shorter integration length producing a greater range in the values of η_{\perp} . The two lengths produce the same results at $\eta_{\perp} \approx 30\%$. For $\eta_{\perp} > 30\%$, the values tabulated in Table 2.3a are greater than those in 2.4a and with $\eta_{\perp} < 30\%$, the opposite is true. The trend is supported by the whispering gallery cavity results which are in the low efficiency regime, consequently the values of η_{\perp} in Table 2.3b are lower than those in 2.4b. This analysis is valid only over the ranges of I_0 and μ covered by the tables. Figures 2.4a and 2.4b show that the relative contour spacing between the short and long integration lengths varies between different regions of I_0 and μ .

As a final consideration of the slow time scale nonlinear theory, it should be mentioned that Fliflet and Read [50] have developed a self-consistent numerical solution to equations equivalent in content to (2.62) and (2.63). By solving the coupled equations with an iterative procedure until a specified tolerance is reached, the resulting solution should yield increased accuracy over the simple assumption of a fixed functional form of $f(z)$. The code was applied to the 0,3,1 cavity TE_{11,2,1(-)} mode in the linear limit, but a large discrepancy between the results and the Gaponov and linear code predictions cast doubt that the program was executing properly at the second harmonic.

-- Fast Time Scale Efficiency Calculations --

In the derivation of equations (2.62) (2.63), a slow time scale momentum variable p was introduced as defined in (2.45). This variable eliminated the change

in momentum due to the cyclotron rotation. Therefore $dp/dt = 0$ in the absence of any interaction with the RF field.

A computer code in use at the MIT Plasma Fusion Center integrates the particle equations of motion in terms of the fast time scale momentum P introduced in equation (2.36). Initially developed by K. R. Chu of the Naval Research Laboratory, the program also differs from the derivation of the slow time scale equations by including the effects of the RF magnetic field. Because the code integrates along the actual particle trajectories with the full interaction of the high frequency fields, it is referred to as a particle integrator. The penalty for the more complete system of equations is the increased computer processing time required.

Chu eliminated the need for the field equation (2.63) by assuming a sinusoidal profile for $f(z)$. This differs from the approach of Nusinovich and Erm who modeled $f(z)$ with a Gaussian. A significant modification of the original fast time scale code was developed by J. Schutkeker of MIT. The new version accepts the actual cold cavity CAVRF field profile as a tabulated function for $f(z)$. The perturbing effect on the fields by the electrons is therefore not included, but the CAVRF profile should provide a more accurate representation for $f(z)$ than either a Gaussian or sinusoidal function.

The particle integrator requires as input a normalized version of the CAVRF output, the detuning parameter x defined in (2.20), and the normalized field strength \hat{E} . In terms of the parameters defined in the Nusinovich and Erm theory,

$$\hat{E} = \frac{F \hat{B} \beta^{1-n}}{J_{m;n}(k r_c)} \left(\frac{2^{n-1} n!}{n^n} \right). \quad (2.70)$$

Here the \tilde{B} is a normalized magnetic field given by $\tilde{B} = \gamma n \omega_{cr} r_0 / c$. The F is defined in equation (2.67) and may be used to relate \tilde{E} to the field amplitude A , with the result $\tilde{E} = 2A/n$.

In execution, the program separately evaluates each input value of x and \tilde{E} . The code uses the CAVRF diffractive Q value and \tilde{E} to compute an output power by $P_{\text{out}} \sim \tilde{E}^2 / Q_D$. The input power required to produce this P_{out} is determined by the η_{el} value from the integration along the electron's trajectory. The final step simply solves for the beam current needed to produce P_{in} at a specified voltage.

The correct value of \tilde{E} at optimum detuning x_{opt} must be found which produces the value of I representing experimental operating conditions. The x_{opt} is optimized with respect to η_{el} for a given value of \tilde{E} . A reasonable estimate of the correct value of \tilde{E} is given by first performing the calculations in the Nusinovich and Erm slow time scale theory, then using the resulting F value in equation (2.70). In a similar manner, x_{opt} is related to Δ_{opt} by

$$x_{\text{opt}} = -\frac{\Delta_{\text{opt}}}{2} \mu. \quad (2.71)$$

These estimates of \tilde{E} and x_{opt} will be accurate only to the extent that the calculated efficiencies between the two theories agree.

As a verification of the accuracy of the particle integrator results at the second harmonic, the code was run in the linear limit for the whispering gallery $\text{TE}_{12,1,1(\cdot)}$ mode. The linear limit was confirmed by inputting several low values of \tilde{E} and checking that $\eta \sim \tilde{E}^2$. The current at these values is equal to I_{LT} . To compare with the Gaponov results, a Gaussian function was used for $f(z)$ instead

of the CAVRF profile function. The only difference between the theories under these conditions should be the consideration of the RF magnetic field by the particle integrator. The agreement was very good, with the Gaponov equation yielding $I_{sT} = 3.3$ amps and the fast time scale code producing an answer of $I_{sT} = 3.45$ amps. Additionally, the Gaussian function for $f(z)$ produced an overall efficiency calculation of $\eta = 7.1\%$ at 5 amps for the same mode. This is close to the slow time scale result of $\eta = 8.1\%$ shown in Table 2.3b.

Efficiencies were evaluated for ten modes in the 0.3.1 cavity using the full capabilities of the fast time scale code with the CAVRF longitudinal field distribution and two separate integration lengths. The values presented in Table 2.5a resulted from using an integration length of $-\frac{\sqrt{3}}{2}\mu \leq \zeta \leq +\frac{\sqrt{3}}{2}\mu$ similar to Nusinovich and Erm 1972. The longer integration length of $-2\sqrt{3}\mu \leq \zeta \leq +2\sqrt{3}\mu$ produced the efficiencies listed in Table 2.5b. Besides the predicted values of η_{el} and η , the corresponding values of \hat{E} and x_{opt} are shown. The results correspond to $V_c = 64.3$ kV and $I = 5$ amps. The long integration length efficiencies were slightly lower than the short length results, but the number of modes evaluated precludes reaching a general conclusion.

Table 2.6 compares the slow time scale and fast time scale results for these ten modes. The particle integrator consistently calculated lower efficiencies than the Nusinovich and Erm theory predictions. The relative differences between the computed values varied between the modes selected. The $TE_{11,2,1(-)}$, $TE_{12,2,1(-)}$ and $TE_{13,2,1(-)}$ showed the best agreement and the largest disagreements were

Table 2.5a — 0,3,1 Cavity $\omega \approx 2\omega_c$ Efficiency Calculations

Fast Time Scale Particle Integrator

Integration Length of $-\frac{\sqrt{3}}{2}\mu \leq \zeta \leq +\frac{\sqrt{3}}{2}\mu$

<i>MODE</i>	\hat{E}	x_{opt}	η_{el} (%)	η (%)
TE_{1,5,1(+)}	0.33	-2.0	18	16
TE_{9,2,1(-)}	0.46	-2.8	27	22
TE_{10,2,1(-)}	0.51	-2.9	27	21
TE_{11,2,1(-)}	0.55	-2.9	26	20
TE_{12,2,1(-)}	0.59	-3.0	25	18
TE_{13,2,1(-)}	0.62	-2.9	24	17
TE_{7,4,1(-)}	0.50	-2.6	19	15
TE_{5,5,1(-)}	0.55	-2.9	22	18
TE_{3,6,1(-)}	0.56	-2.9	22	18
TE_{8,4,1(-)}	0.60	-3.0	23	18

Table 2.5b -- 0,3,1 Cavity $\omega \approx 2\omega_c$ Efficiency Calculations
Fast Time Scale Particle Integrator
 Integration Length of $-2\sqrt{3}\mu \leq \zeta \leq +2\sqrt{3}\mu$

<i>MODE</i>	\hat{E}	x_{opt}	η_{et} (%)	η (%)
TE _{1,5,1} (-)	0.30	- 2.3	16	14
TE _{9,2,1} (-)	0.44	-2.8	25	21
TE _{10,2,1} (-)	0.49	-2.7	26	20
TE _{11,2,1} (-)	0.54	-3.0	25	20
TE _{12,2,1} (-)	0.58	-2.9	25	18
TE _{13,2,1} (-)	0.58	-2.5	21	15
TE _{7,4,1} (+)	0.48	-2.7	18	15
TE _{5,5,1} (-)	0.53	-2.6	22	18
TE _{3,6,1} (-)	0.54	-3.0	21	17
TE _{8,4,1} (-)	0.59	-2.9	23	18

Table 2.6 — 0,3.1 Cavity $\omega \approx 2\omega_c$ Efficiency Calculations Comparison

MODE	EFFICIENCY — η (%)			
	NUSINOVICH and ERM		PARTICLE INTEGRATOR	
	SHORT	LONG	SHORT	LONG
TE_{1.5,1(+)}	20	19	16	14
TE_{9.2,1(-)}	26	24	22	21
TE_{10.2,1(-)}	25	23	21	20
TE_{11.2,1(-)}	23	22	20	20
TE_{12.2,1(-)}	21	20	18	18
TE_{13.2,1(-)}	19	18	17	15
TE_{7.4,1(-)}	25	23	15	15
TE_{5.5,1(-)}	21	19	18	18
TE_{3.6,1(-)}	21	20	18	17
TE_{8.4,1(-)}	25	23	18	18

with the $TE_{1,5,1(+)}$ and the $TE_{7,4,1(+)}$ modes. The particle integrator calculations for the whispering gallery cavity continued the trend of lower efficiencies by predicting all of the modes to be below threshold. Because the fast time scale program agreed reasonably well with the slow time scale theories when input with a Gaussian, the major source of the discrepancy was believed to be the difference in field distribution between the Gaussian and the CAVRF profile.

2.4 $\omega_c \rightarrow 2\omega_c$ Efficiency Scaling

The slow time scale nonlinear theory with the Gaussian approximation for $f(z)$ suggests a method of estimating efficiencies at the second harmonic from the operating parameters at the fundamental. The simplicity of the efficiency determinations using the Nusinovich and Erm plots (Figures 2.4a and 2.4b) is the result of having reduced η_{\perp} to a function of the two parameters I_o and μ . By deriving a scaling law between I_o at the fundamental ($I_{o(n=1)}$) and the second harmonic ($I_{o(n=2)}$) as well as deriving the relationship between $\mu_{(n=1)}$ and $\mu_{(n=2)}$, the graphs may be used to map regions of interest at the fundamental to the second harmonic. This could provide a reasonable estimation of second harmonic efficiencies from a device designed for operation at the fundamental. The following analysis was originally developed by R. J. Temkin at MIT.

The parameters necessary for the scaling approximation are those in equation (2.27) defining μ and equation (2.68) for I_o . The derivation will be kept as general as possible, though some assumptions will be made concerning the operating mode and beam placement. All of the experimentally controlled variables will be held constant.

Using the approximation $\omega \approx n\omega_c \sim nB$, a constant magnetic field value yields $\omega_{(n=2)} \approx 2\omega_{(n=1)} \longrightarrow \lambda_{(n=2)} \approx 0.5\lambda_{(n=1)}$. Neglecting minor differences between the effective cavity lengths results in the expression

$$\left(\frac{L_{\text{eff}}}{\lambda}\right)_{(n=2)} \approx 2 \left(\frac{L_{\text{eff}}}{\lambda}\right)_{(n=1)} \quad (2.72)$$

This relation and cancelling the common factors in equation (2.27) yields the relationship between μ at the fundamental and the second harmonic.

$$\mu_{(n=2)} \approx 2\mu_{(n=1)} \quad (2.73)$$

To determine the scaling law for I_o , the ratio of $I_{o(n=2)}/I_{o(n=1)}$ is formed using equation (2.68). By eliminating the constants and using the substitution (2.72), the following expression is obtained.

$$\frac{I_{o(n=2)}}{I_{o(n=1)}} \approx \frac{2}{\pi^2} \left(\frac{\beta_{\parallel}}{\beta_{\perp}}\right)^2 \left(\frac{\lambda}{L_{\text{eff}}}\right)_{(n=1)}^2 \frac{Q_{(n=2)} G_{(n=2)}}{Q_{(n=1)} G_{(n=1)}} \quad (2.74)$$

To proceed further, an estimation must be made for the ratios of Q and G between harmonics.

For the Q scaling, it will be assumed that the beam placement allows ignoring the whispering gallery modes. From previous descriptions, the 0.3.1 cavity would meet such a condition, but obviously not the whispering gallery cavity. Neglecting the whispering gallery modes permits the approximation $Q \sim Q_D$. The expression for Q_D is given by

$$Q_D \approx 4\pi \left(\frac{L_{\text{eff}}}{\lambda}\right)^2 \frac{1}{1 - |R_1 R_2|} \quad (2.75)$$

where R_1 and R_2 are the reflection coefficients for the ends of the cavity. The $\frac{1}{1-|R_1 R_2|}$ term will generally be slightly larger for the second harmonic, but disregarding this difference, $Q_D \sim \left(\frac{L_{\text{eff}}}{\lambda}\right)^2$ yielding

$$\frac{Q_{(n=2)}}{Q_{(n=1)}} \approx 4. \quad (2.76)$$

The G factor defined in equation (2.28) is obviously mode specific. By assuming that the beam will be in a near optimum location to excite the second harmonic mode, the following coarse simplification can be made for both the $n = 1$ and $n = 2$ modes.

$$\frac{J_{m \pm n}^2(k_{\perp} r_c)}{J_m^2(\nu_{mp})} \approx 1 \quad (2.77)$$

This reduces the G factor scaling to

$$\frac{G_{(n=2)}}{G_{(n=1)}} \approx \frac{[\nu_{mp(n=1)}^2 - m_{(n=1)}^2]}{[\nu_{mp(n=2)}^2 - m_{(n=2)}^2]}. \quad (2.78)$$

Having already disregarded whispering gallery modes, now neglecting other extreme "surface" modes allows the generalization $\nu_{mp}^2 \gg m^2$. The resulting simplification is given by

$$\frac{G_{(n=2)}}{G_{(n=1)}} \approx \frac{\nu_{mp(n=1)}^2}{\nu_{mp(n=2)}^2} \approx \frac{k_{\perp(n=1)}^2}{k_{\perp(n=2)}^2} \approx \frac{\lambda_{(n=2)}^2}{\lambda_{(n=1)}^2} \approx \frac{1}{4}. \quad (2.79)$$

This scaling factor was checked against actual G value ratios computed using the wall and beam radius values applicable to the 0,3,1 cavity. Modes were chosen such that $\nu_{mp(n=2)} \approx 2\nu_{mp(n=1)}$. The results produced a range of $G_{(n=2)} / G_{(n=1)}$ ratios from 0.12 to 0.46. It appears that the scaling is accurate to within a factor of two with the included mode restrictions and beam placement assumptions.

Expressions (2.76) and (2.79) for the Q and G ratios cancel each other when substituted back into equation (2.74). The remaining factors are easily written in terms of $\mu_{(n=1)}$.

$$\frac{2}{\pi^2} \left(\frac{\beta_{\parallel}}{\beta_{\perp}} \right)^2 \left(\frac{\lambda}{L_{\text{eff}}} \right)_{(n=1)}^2 = \frac{2\beta^2}{\mu_{(n=1)}^2} \quad (2.80)$$

The final expression for $I_{o(n=2)}$ in terms of I_o at the fundamental is

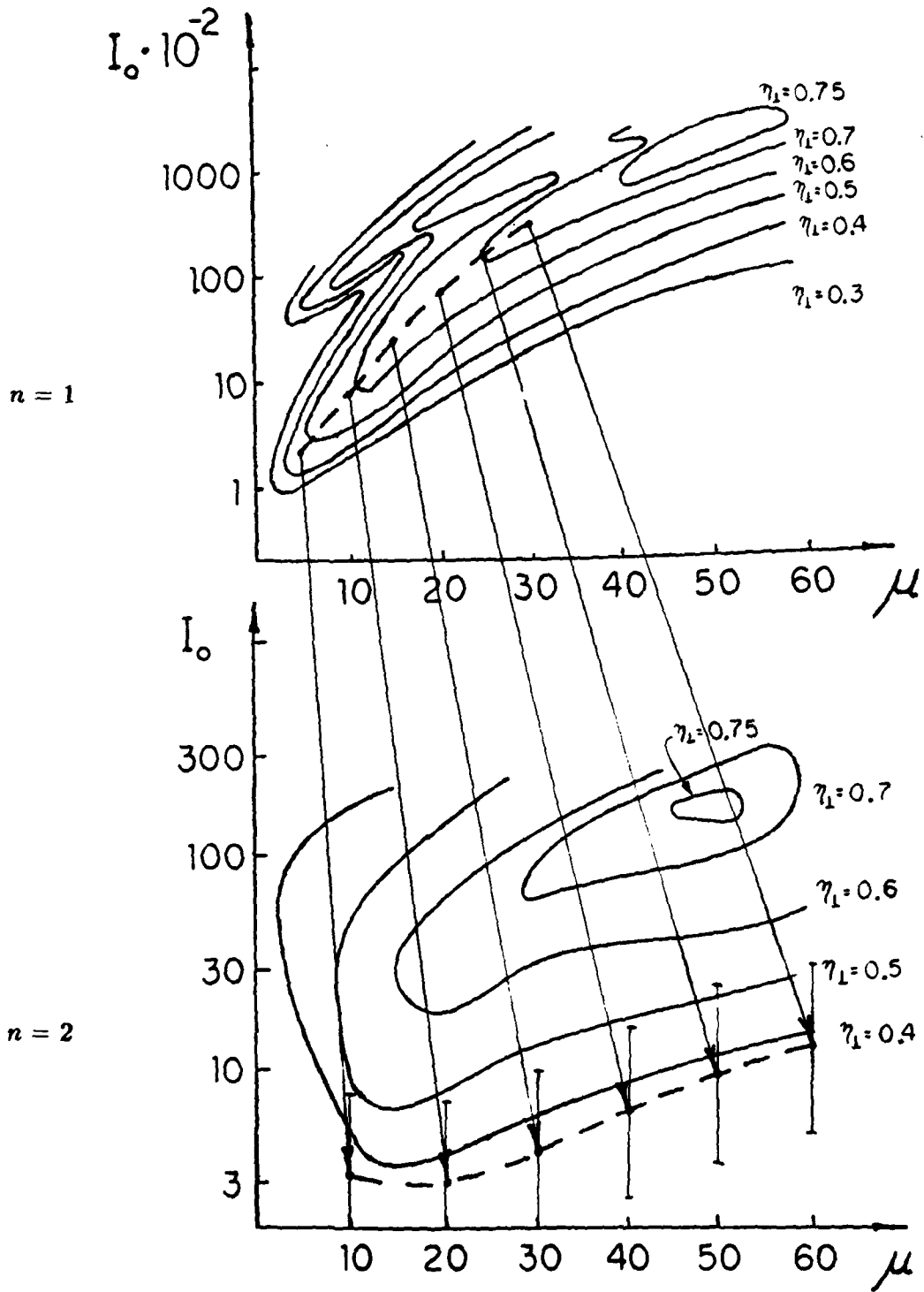
$$I_{o(n=2)} \approx \frac{2\beta^2}{\mu_{(n=1)}^2} I_{o(n=1)}. \quad (2.81)$$

This result should provide a reasonable estimate of $I_{o(n=2)}$ to within a factor of ≈ 2.5 . The expression is not useful in consideration of specific modes, but will provide an order of magnitude view of $I_{o(n=2)}$, and therefore $\eta_{\perp(n=2)}$, for a particular range of I_o and μ at the fundamental.

An example of this scaling is graphically displayed in Figure 2.5. The two graphs in the figure are from Gaponov's paper [45] describing the 1975 Nusinovich and Erm results. The plot at the top is applicable to the fundamental and the bottom graph is for the second harmonic. The horizontal scales are the same between the two diagrams, but the vertical axes of I_o have different log scales.

The dashed line on the $n = 1$ figure follows the first ridge of contours representing I_o optimized with respect to η_{\perp} over that range of μ . This would be a typical range of investigation for design of a gyrotron operating at the fundamental. The long arrows down to the $n = 2$ plot show how specific points on the dashed curve map to the second harmonic by the derived relations (2.81) and (2.73). For this example, $\beta_{\perp} = 0.38$ was used in the calculation of $I_{o(n=2)}$. The dashed line

Fig 2.5 — $\omega_c \rightarrow 2\omega_c$ Efficiency Estimation



on the $n = 2$ diagram is the map of the dashed line above. The vertical bars extending from the mapped points represent the estimated range of error.

An interesting aspect of the example presented is the fairly constant value of η_{\perp} on the second harmonic dashed line. The range of η_{\perp} extended from 45% to 72% at the fundamental, yet the scaled values of I_o and μ at the second harmonic result in $\eta_{\perp} = 38\% \pm 2\%$. Even including the rather large error bars, the scaled values still remain in a high efficiency zone with $25\% < \eta_{\perp} < 50\%$. This would be an area of concern for megawatt, $n = 1$ designed gyrotrons. Such high levels of second harmonic efficiency could damage components or degrade efficiency at the fundamental.

Chapter 3

Description of the Experiment

The primary goal of the experimental investigation was to determine the presence of harmonic emission from the MIT gyrotron. Secondary objectives included frequency measurement for mode identification, starting current determination and output power level measurement.

The MIT gyrotron is described in Section 1.2 of this paper. The 0,3,1 resonator cavity introduced in the same section and discussed throughout Chapter 2 was used exclusively in the experimental investigation. The whispering gallery cavity has undergone initial testing at the fundamental, but the harmonic content has not been studied to date.

This chapter will explain the procedures used in obtaining the experimental results. The first section details the magnetic field scan to detect harmonic emission. Section 3.2 discusses the frequency measurement technique which allowed mode identification. The third section describes the starting current determination and the chapter concludes by explaining the power measurement techniques in Section 3.4.

3.1 — The Magnetic Field Scan to Detect Harmonic Emission

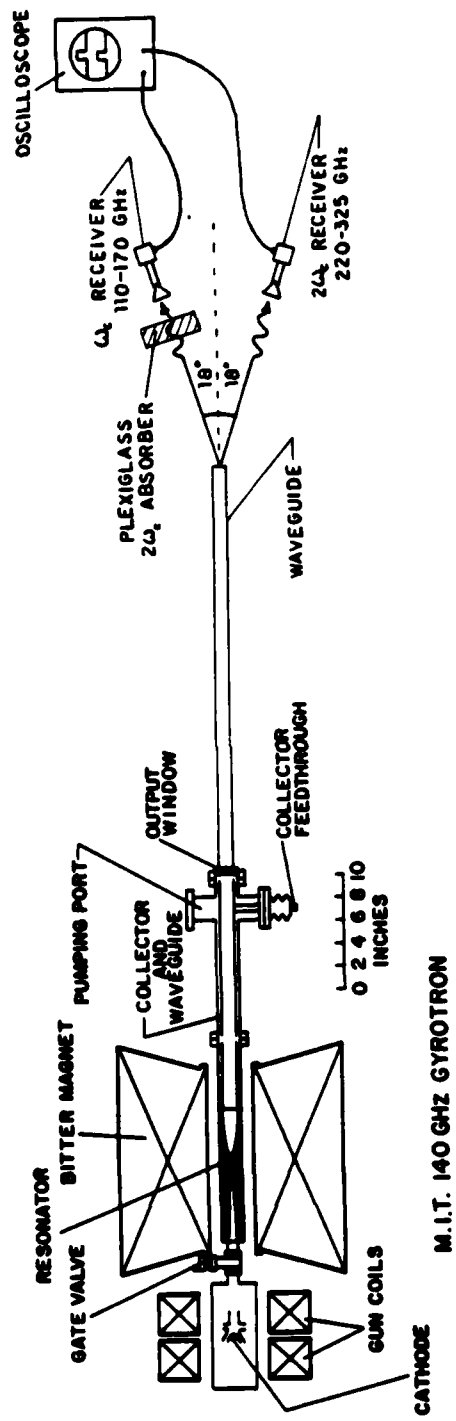
The primary objective of the experimental investigation was fulfilled by a scan over the normal operating magnetic field range to detect the presence of second or higher harmonic modes. The fundamental emission was mapped simultaneously over the same field range to correlate results with the possibility of mode competition between the fundamental and harmonic modes.

Figure 3.1 diagrams the apparatus used during the magnetic field scan. The radiation is coupled out of the gyrotron through one meter of 2.2 cm diameter oversized cylindrical waveguide. The fundamental and second harmonic receivers depicted in the figure were placed in the far field radiation pattern approximately 16 inches from the end of the output waveguide. The receivers were aligned in the same horizontal plane as the waveguide and placed symmetrically at 18° off axis to coincide with the major lobes of the far field pattern.

The second harmonic receiver consisted of a 25 dB gain WR-3 band horn, a one inch section of WR-3 band waveguide, a variable dial attenuator and a video diode for a detector. The operational frequency range for WR-3 band is 220-325 GHz with a cutoff frequency of 172 GHz. The diode was a Baytron model 4-06-005 x wafer in a Baytron 4-06-105A detector mount. The fundamental receiver used a 25 dB gain WR-6 band horn, a dial attenuator, Hughes wavemeter and a Hughes model 47328H-1111 video diode. The WR-6 band has an operational frequency range of 110-170 GHz.

The diodes were chosen to be optimized for the frequency band, but both showed some response in the other's frequency range. Precautions were taken to

Fig 3.1 — Experimental Arrangement for the Magnetic Field Scan



ensure only second harmonic signals entered the $2\omega_c$ diode and the fundamental diode received only fundamental emission. In the first case, the fundamental radiation was below the cutoff frequency for the WR-3 band waveguide and dial attenuator used in the $2\omega_c$ receiver. To prevent the higher harmonic radiation from entering the fundamental receiver, a 2.2 inch thick piece of plexiglass absorber was placed in front of the receiver horn. The attenuation at the fundamental was measured by comparing relative diode signal strengths with and without the plexiglass. The results showed an 8.6 dB reduction in signal at 128 GHz. This is in agreement with the ν^2 scaling of the absorption coefficient which will be discussed in Section 3.4. The success at preventing leakage of the higher frequency $2\omega_c$ radiation was indicated by placing the plexiglass in front of the second harmonic receiver. This resulted in the complete loss of the strongest second harmonic signal at 241 GHz, representing an attenuation of over 27 dB. As a final precaution, both detectors were encased in a layer of Eccosorb material to prevent reflected RF signals from entering the diodes.

The dial attenuator for the second harmonic receiver system was calibrated allowing conversion of dial settings to relative signal loss. The harmonic emission from a Hughes 140 GHz IMPATT device provided the radiation during the calibration. The change in signal strength as a function of dial attenuator setting was recorded. The variable attenuator used in the fundamental receiver system was precalibrated for direct dB readings. Throughout the magnetic field scan, the relative signal strength was determined by adjusting the calibrated dial attenuators to maintain constant diode output voltages. This method was preferred since it

precluded damage or inaccurate readings caused by saturation beyond the linear response region of the diodes.

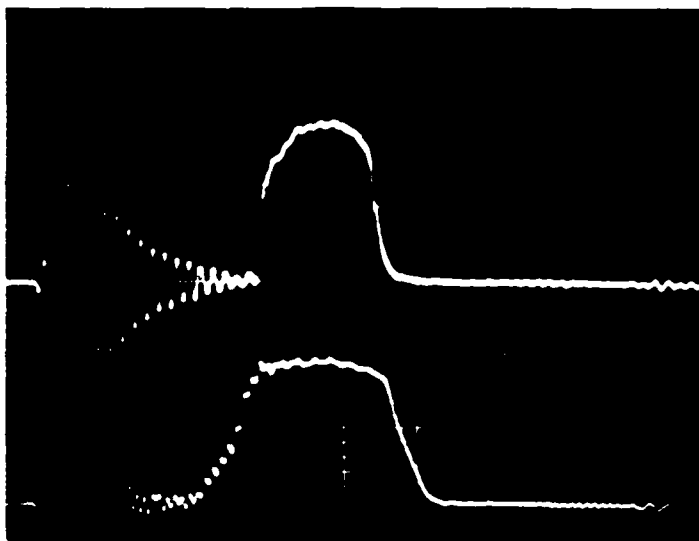
The diode signals were monitored simultaneously on separate channels of a dual trace oscilloscope. Figure 3.2 shows pulse shapes from the second harmonic and fundamental diodes. The 0.8–1.0 μsec pulse lengths indicated in the figure were typical throughout the experimentation. The high frequency noise prior to the pulse is pickup from the high voltage power supply. The repetition rate was 4.16 pulses per second. The cathode voltage $V_c = 64.3$ kV and beam current $I = 5$ amps listed in Figure 3.2 were held constant through the range of magnetic field values.

The magnetic field was scanned from 4.0 to 6.0 tesla. The lower value of 4.0 tesla was chosen to ensure adequate beam quality. The upper limit ensured that the fundamental mode frequencies remained below cutoff for the WR-3 band waveguide used in the $2\omega_c$ receiver. The magnetic field was varied in 0.044 tesla increments. At each point the gun coils were adjusted to optimize the signal from the second harmonic diode. The dial attenuators were varied to keep both diode voltages between 10–40 mV. The measured signal voltage and dial attenuator reading were recorded.

Figure 3.3a graphs the results from the fundamental diode. The $\text{TE}_{2,3,1}$ mode at 5.26 tesla provided the zero dB reference for the relative diode signal plotted on the vertical axis. As noted on the figure, the diode response is frequency dependent. Therefore, the peaks plotted on Figure 3.3a do not provide a reliable measurement of mode intensity. For example, comparable power is obtained in

Fig 3.2 — Fundamental and Second Harmonic Diode Pulse Shapes

I = 5 amps, V_c = 64.3 kV, B = 5.26 tesla



Horizontal Time Scale — 0.5 μ sec/cm

Top Trace — $2\omega_c$ Diode Signal into 280 Ω Terminator

Vertical Scale — 20 mV/cm with 3.3 dB Attenuation

TE_{4,5,1} Mode at 263.31 GHz

Bottom Trace — ω_c Diode Signal into 200 Ω Terminator

Vertical Scale — 10 mV/cm with 44.6 dB Attenuation

TE_{2,3,1} Mode at 137.35 GHz

Fig 3.3a — Fundamental Emission

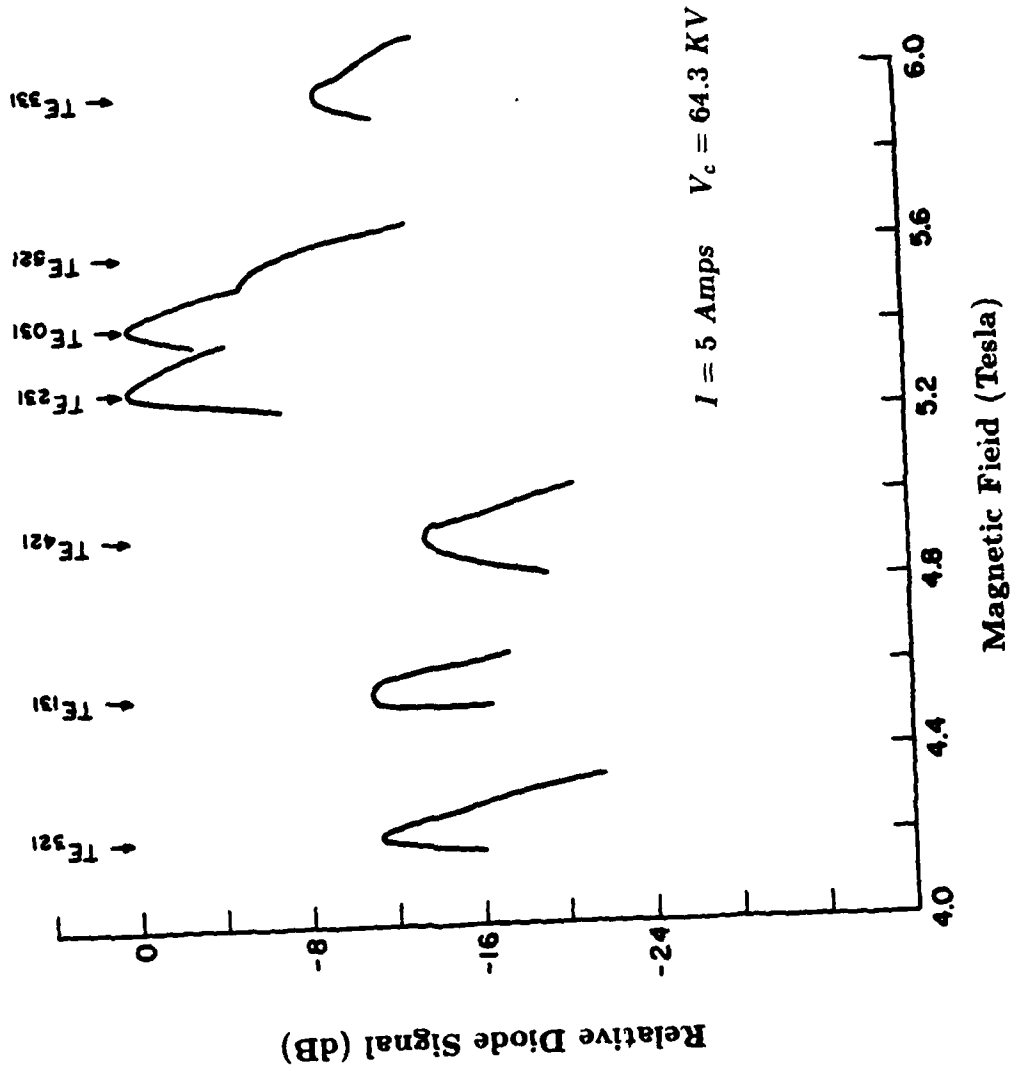
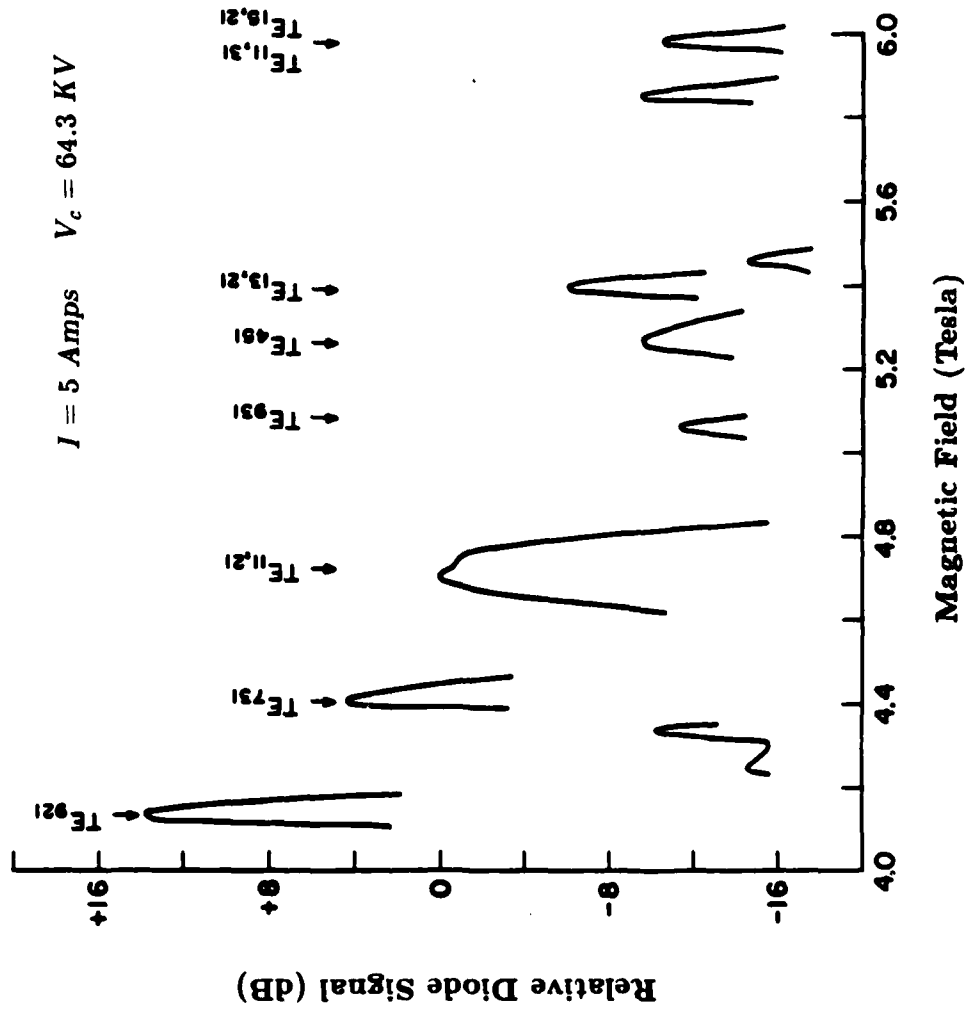


Fig 3.3b — Second Harmonic Emission



Note: Diode Responsivity is Frequency Dependent

the $TE_{0,3,1}$ and $TE_{4,2,1}$ modes, yet the latter yields a significantly lower diode signal. The areas on the graph where there are no peaks correspond to no diode signal with the dial attenuation reduced to zero.

The relative diode signal from the second harmonic receiver is shown in Figure 3.3b. The $TE_{11,2,1}$ mode at 4.70 tesla provided the zero dB reference in this case. The diode response is frequency dependent so conclusions concerning output power should not be drawn by the relative peak heights. This is particularly true of the $TE_{9,2,1}$ and $TE_{7,3,1}$ modes at 4.12 and 4.40 tesla respectively. The $TE_{7,3,1}$ mode at 226 GHz is on the edge of the 220-325 GHz frequency band for the $2\omega_c$ diode. The $TE_{9,2,1}$ mode at 209 GHz is actually out of this frequency range and the diode response characteristics could be quite different from its behavior at 241 GHz for the $TE_{11,2,1}$ mode. The output power measurements using a calorimeter described in Section 3.4 verify the misleading nature of the diode signal by showing the $TE_{11,2,1}$ to be a stronger mode than the $TE_{9,2,1}$. The rest of the peaks plotted above 5.0 tesla in Figure 3.3b are within the operational frequency band of the diode and should provide some measure of relative mode strength.

The modes identified on both Figures 3.3a and 3.3b were determined by frequency measurements. For the more stable signals at the fundamental, the Hughes wavemeter included in the fundamental receiver provided an adequate frequency measurement. However, an harmonic mixing system yielded higher accuracy and was more useful for some of the weaker or more erratic signals. This frequency measurement system is the subject of the next section.

3.2 — Frequency Determination by Harmonic Mixing

A highly accurate and sensitive method of frequency measurement using an harmonic mixing technique was employed during the magnetic field scan to identify specific second harmonic modes. The method had been used previously for real-time spectral analysis of far infrared laser signals [51] and has also been used to measure the bandwidth and frequency pulling of the MIT gyrotron at the fundamental [52].

The components of the mixer system are displayed schematically in Figure 3.4. The RF from the gyrotron is heterodyned in the harmonic mixer with a harmonic of the lower frequency local oscillator (LO). The resultant intermediate frequency (IF) is given by the following equations.

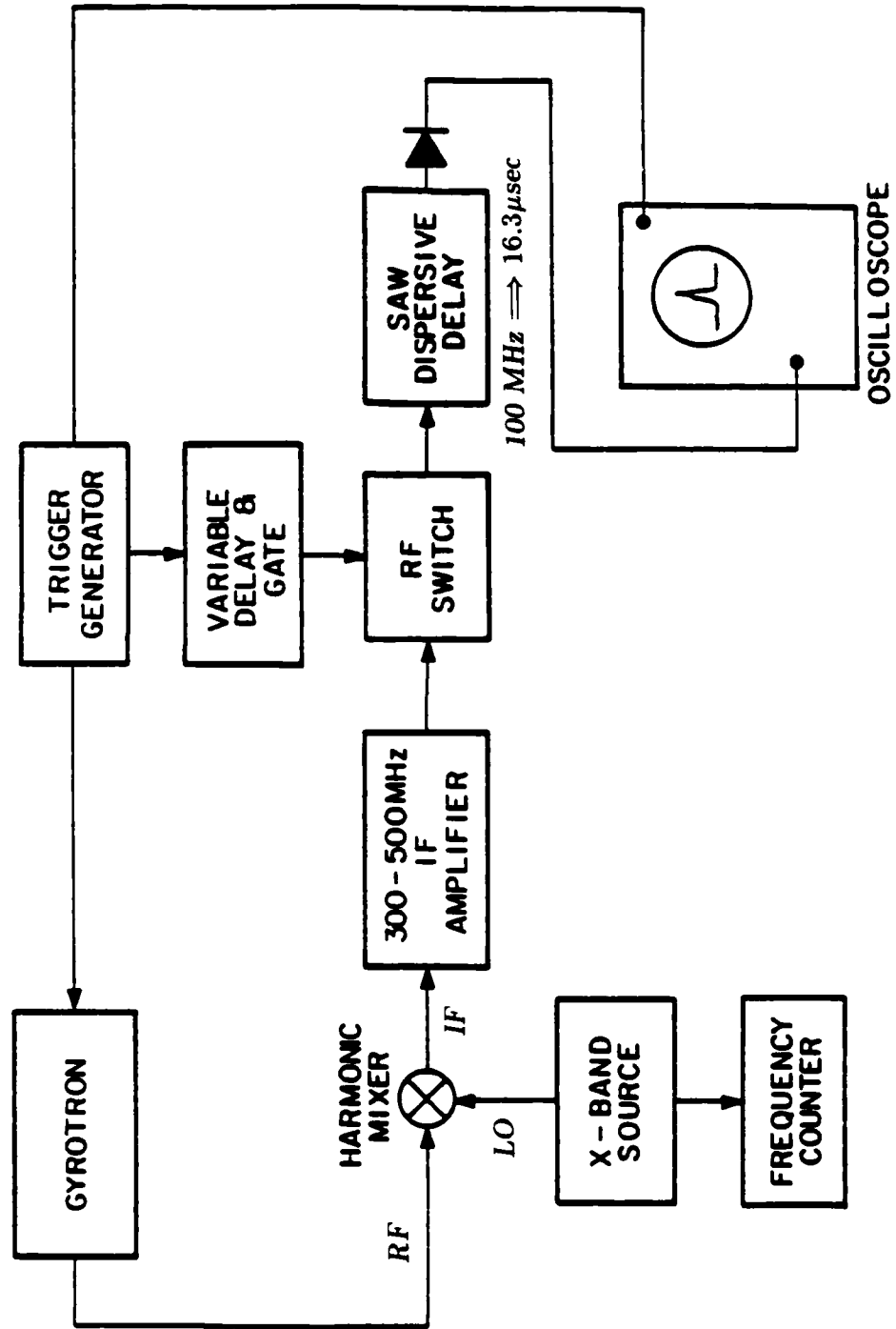
$$\nu_{RF} = n_{LO} \nu_{LO(\text{upper})} - \nu_{IF} \quad (3.1a)$$

$$\nu_{RF} = n_{LO} \nu_{LO(\text{lower})} + \nu_{IF} \quad (3.1b)$$

Here $\nu_{LO(\text{upper})}$ and $\nu_{LO(\text{lower})}$ represent the fundamental LO frequencies corresponding to the upper and lower sidebands. The IF signal is amplified and then processed by a surface acoustic wave (SAW) dispersive delay. This allows the IF frequency to be displayed as a function of time on an oscilloscope.

When a second harmonic frequency measurement was desired, the $2\omega_c$ diode signal was optimized by adjusting the magnetic field and gun coils. The receiver for the harmonic mixing system was positioned in place of the fundamental receiver shown in Figure 3.1 and the plexiglass absorber was removed. The harmonic mixing receiver system consisted of a 25 dB gain WR-3 band horn, a two inch

Fig 3.4 --- Schematic Diagram of the Harmonic Mixer System



section of WR-3 band waveguide, a dial attenuator similar to the one used on the $2\omega_c$ receiver, a waveguide transition from WR-3 to WR-6 and a Hughes model 47448H-1002 harmonic mixer. The WR-3 waveguide prevented the gyrotron's fundamental emission from entering the harmonic mixer. The effect of reflected RF radiation was minimized by a layer of Eccosorb around the mixer.

The LO signal was provided by a YIG tuned Gunn oscillator which produced 20-30 mW of output power in the 12-16 GHz frequency band. The RF frequency range of 200-300 GHz required mixing with high harmonics of the local oscillator, with $15 \leq n_{LO} \leq 20$. The fundamental LO frequency was monitored by an EIP model 548 frequency counter.

The variable gate coupled through an RF switch on Figure 3.4 allowed an adjustable 250-300 nsec segment of the gyrotron pulse to be isolated. The variable delay permitted various portions of the pulse to be gated. For the frequency measurements during the present investigation, the gate was set to a 300 nsec segment coincidental with the flat-top of the gyrotron pulse.

The SAW device was a LiNbO_3 dispersive delay which analyzed IF signals in the 470-370 MHz range by delaying them as a linear function of frequency. The resultant time delays ranged from 4 to 20.3 μsec . By adjusting the horizontal time scale on the oscilloscope to include the total 16.3 μsec dispersive delay, the 100 MHz SAW bandwidth was displayed. In practice, a 2 μsec div time scale was converted to a 12.3 MHz div frequency scale.

Adjustments in the LO frequency resulted in linear changes in the IF frequency by equation (3.1). The time scale on the scope was calibrated by changing

AD-A145 621

HARMONIC EMISSION FROM HIGH POWER GYROTRON OSCILLATORS
(U) AIR FORCE INST OF TECH WRIGHT-PATTERSON AFB OH
J L BYRRLY MAY 84 AFIT/CI/NR-84-43T

272

UNCLASSIFIED

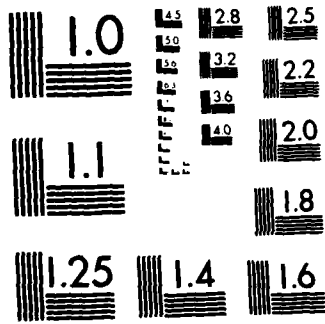
F/G 12/1

NL

END

FILMED

DTIC



MICROCOPY RESOLUTION TEST CHART
NATIONAL BUREAU OF STANDARDS 1963-A

the LO frequency until the displayed IF pulse disappeared symmetrically about the midpoint of the horizontal axis. The pulse disappearance was due to exceeding the 470-370 MHz bandwidth limits on the SAW device, thus the midpoint was known to represent an IF frequency of 420 MHz. Because the higher frequencies received less delay in the SAW, the left side of the scope represented $\nu_{IF} > 420$ MHz and the right side of the scope displayed signals with $\nu_{IF} < 420$ MHz.

The procedure for frequency determination involved scanning the LO frequency until an IF pulse appeared on the scope. The pulse was centered and the LO frequency was recorded. The pulse was identified as an upper or lower sideband by increasing the LO frequency slightly. If the pulse moved right indicating a decrease in IF frequency, it was identified as the lower sideband and the plus sign in equation (3.1b) applied. If the pulse moved left when the LO frequency was increased, it was the upper sideband and the minus sign in equation (3.1a) was appropriate.

The local oscillator harmonic number (n_0) could easily be determined because ν_{IF} was always adjusted such that $\nu_{IF} = 420$ MHz. By locating both upper and lower sideband, n_0 could be calculated by

$$n_0 = \frac{0.81 \text{ GHz}}{P_{\text{upper}} - P_{\text{lower}}} \quad (3.2)$$

At this point, everything on the right side of equations (3.1a) and (3.1b) was determined allowing calculation of the RF frequency by either expression. The instrumental limit on the accuracy of the frequency measurement was approximately 3 MHz.

Table 3.1 Observed Second Harmonic Emission

<i>MODE</i>	<i>PREDICTED FREQUENCY (GHz)</i>	<i>MEASURED FREQUENCY (GHz)</i>	<i>MAGNETIC FIELD (tesla)</i>
TE_{9 2 1}	209.51	209.43	4.13
TE_{7 3 1}	226.52	226.39	4.40
TE_{11 2 1}	241.17	241.02	4.70
TE_{9 3 1}	260.39	260.29	5.09
TE_{4 5 1}	263.01	263.31	5.26
TE_{13 2 1}	272.42	272.21	5.39
TE_{11 3 1}	293.60	294.08	5.98
TE_{15 2 1}	303.35	302.40	5.98

The frequencies measured during the magnetic field scan and the second harmonic modes they represent are shown in Table 3.1. Also listed are the scaled CAVRF frequencies from Table 2.1a and the magnetic field value where the frequency was determined. The agreement between the measured and theoretical frequencies is generally within 0.1%. The $TE_{11,5,1}$ and the $TE_{11,2,1}$ modes, which were in the high magnetic field region, had measured frequencies which differed from the theoretical value by $\pm 0.3\%$. Frequency pulling could account for the differences.

Problems encountered during the frequency measurements ranged from not finding an RF signal on the oscilloscope to finding too many. This generally represented either too little RF entering the mixer or too much, the latter case producing numerous beat frequencies which were usually impossible to analyze. The dial attenuator proved helpful in finding the correct RF signal level when the $2\omega_c$ diode signal was fairly stable. In some cases, several upper and lower sidebands could be matched by pulse shape and amplitude. This was required when multimoding was present, such as the $TE_{11,5,1}$ and $TE_{11,2,1}$ both oscillating at the same magnetic field value of 5.08 tesla.

3.3 Starting Current Determination

The starting current was measured directly for the $TE_{11,2,1}$ mode at 241.02 GHz. The experimental arrangement was exactly the same as for the frequency measurements described in the last section. Since the fundamental diode was not used, one channel of the dual trace oscilloscope was devoted to displaying the

beam current. The other channel displayed the 2_{nd} diode signal and the IF signal from the harmonic mixer system was monitored on another oscilloscope.

The TE₁₁₂ mode was located at 170 tesla and verified by a frequency measurement with the mixer system. One sideband of the IF from the SAW device was monitored during the entire starting current measurement to confirm the continued presence of the mode.

The beam current was gradually reduced and the magnetic field was increased as necessary to optimize the 2_{nd} diode signal. The gun coils were also adjusted at each beam current value to produce the best signal. As discussed in Chapter 2 theory predicts the required increase in magnetic field because the optimum detuning at 1 cm is $\delta \approx 2$ and at the maximum $L \approx 2$. The detuning value δ becoming less negative corresponds to an increase in L .

The procedure of reducing the current and optimizing the trans and gun magnetic fields continued until the mode could no longer be detected by either the second harmonic diode or by the harmonic mixer system. The beam current value was then increasing the mode was recorded as the minimum starting current. For the TE₁₁₂ mode the mode peak value was $I = 102$ A. The ω is predicted by the capacitor equation listed in Table 2.2 as 1000 A.

3.4 Output Power Level Measurements

Accurate determinations of output power in the 200-300 GHz frequency range and kW power regime are difficult due to a lack of suitable diagnostics. Appropriately modified calibrations were used in the present study to measure the output power from the TE₁₁₂ mode at 211.02 GHz and the TE₁₁₁ mode at 209.42

(11). These two second harmonic modes were chosen because they provided a consistently stable $2\omega_0$ diode signal and were present at magnetic field values with minimal fundamental oscillation. The two questions which needed to be resolved during the investigation were how much power is absorbed by the calorimeters at each frequency and how much of the total power is attributable to the second harmonic mode as opposed to simultaneous fundamental oscillation.

The general methodology involved taking repeated calorimeter measurements with varying thicknesses of plexiglass absorber to discriminate between the $2\omega_0$ and ω_0 power levels. Assuming negligible power from frequencies higher than the second, the unknowns are mathematically displayed in the following equations for P' , the total calorimeter measured power without plexiglass and P'' , the total measured power with a plexiglass absorber of thickness x .

$$P' = A_1 P_{\omega_0} + A_2 P_{2\omega_0} \quad (2.2)$$

$$P'' = A_1 P_{\omega_0} (1 - R_1 x) + A_2 P_{2\omega_0} (1 - R_2 x) \quad (2.3)$$

In these equations, P_{ω_0} and $P_{2\omega_0}$ represent the total true power incident in the fundamental and second harmonic modes, respectively. The coefficient A_1 is the percent absorption by the calorimeter at ω_0 , the fundamental frequency, and A_2 is the same parameter at $2\omega_0$, the second harmonic frequency. The R_1 in equation (2.3) is the reflectance of plexiglass at ω_0 incident frequency, and R_2 and R_3 are the plexiglass absorption coefficients at ω_0 and $2\omega_0$. Each of these parameters will be discussed in

detail in subsequent paragraphs. The unknown of interest is P_2 , the true power at the second harmonic. Solving the equations for P_2 yields

$$P_2 = \frac{1}{4} \left[\frac{P_1 - P_2}{1 - \frac{P_1 - P_2}{4P_2}} \right] \quad (2.5)$$

In this expression, P_1 , P_2 , and t are the normalized quantities and k_1 , α_1 , α_2 , and k must be determined for an accurate calculation of P_2 . The parameter k_1 has cancelled out of the equations and does not enter into the solution.

The calculations used in the investigation were done with each of the two circuit models. To increase absorption, an absorption coefficient was used and both have been modified by adding losses of the circuit to the absorption factor. To determine the actual amount of absorption at the second harmonic frequency (the coefficient k_2) both experimental setups were used and the dispersion function in the form $\frac{1}{1 - \frac{P_1 - P_2}{4P_2}}$. The method developed by M. A. A. and H. H. H. H. is a highly accurate method of determining the surface impedance and absorption coefficient at millimeter and submillimeter wavelengths.

The results of the H. H. H. H. analysis were the graphs depicting reflection as a function of frequency shown in Figures 2(a) and 2(b). The loss and gain curves as a function of frequency of the filter in Figure 2(a) and Figure 2(b) represent the reflection of the wave into the absorber. The transmission curve on the bottom of the graph is a plot of the transmission coefficient of the $t = 2$ as discussed in Chapter 2. The reflection plotted on the vertical axis represents the total absolute reflection squared, which is directly applicable to power calculations. The experimental absorption coefficient k_2 is plotted by simply subtracting the gain curve

Fig 2.5a - Dispersion Fourier Transform Spectroscopy Reflectivity Plot
of the 6 inch Brimsted Calculator

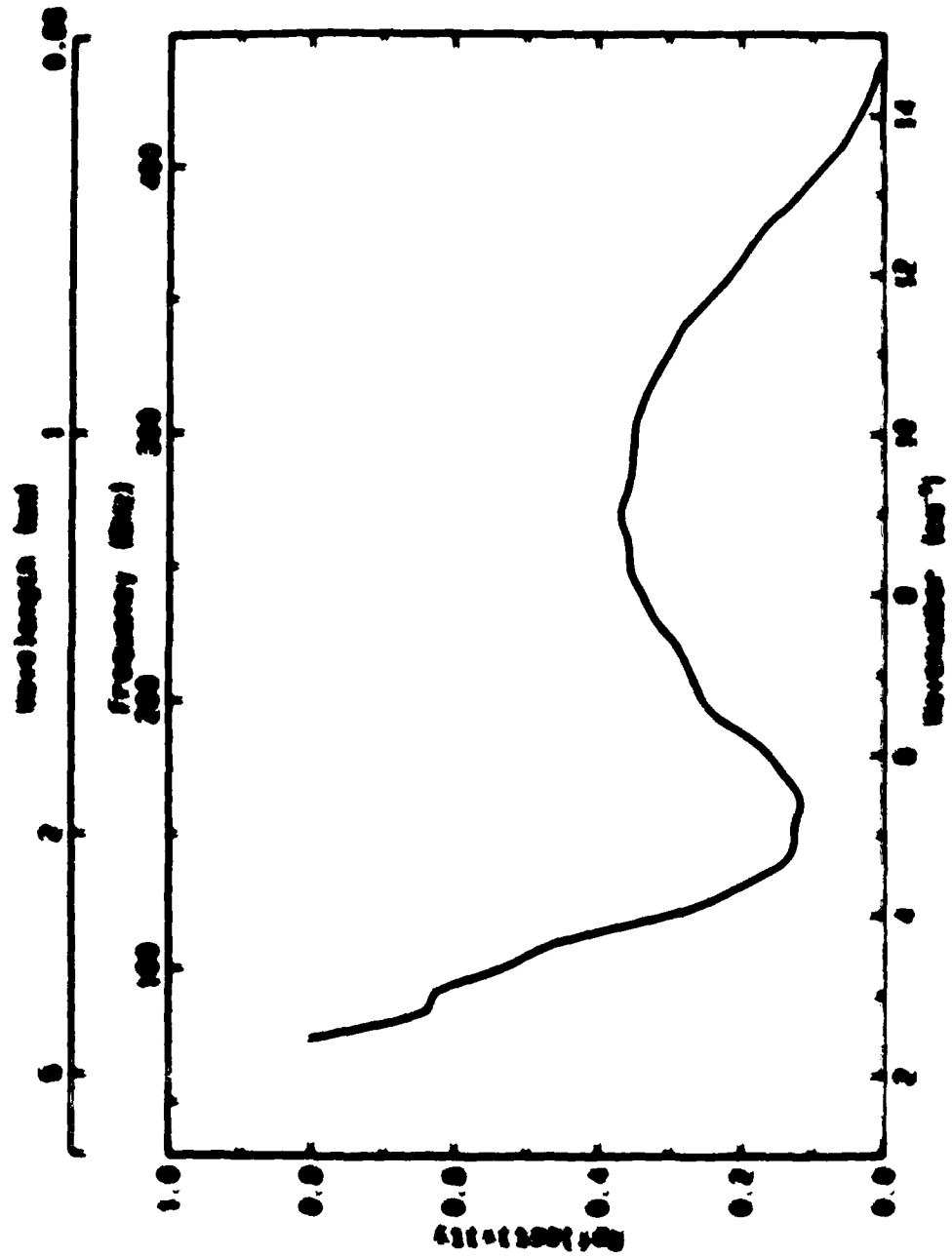
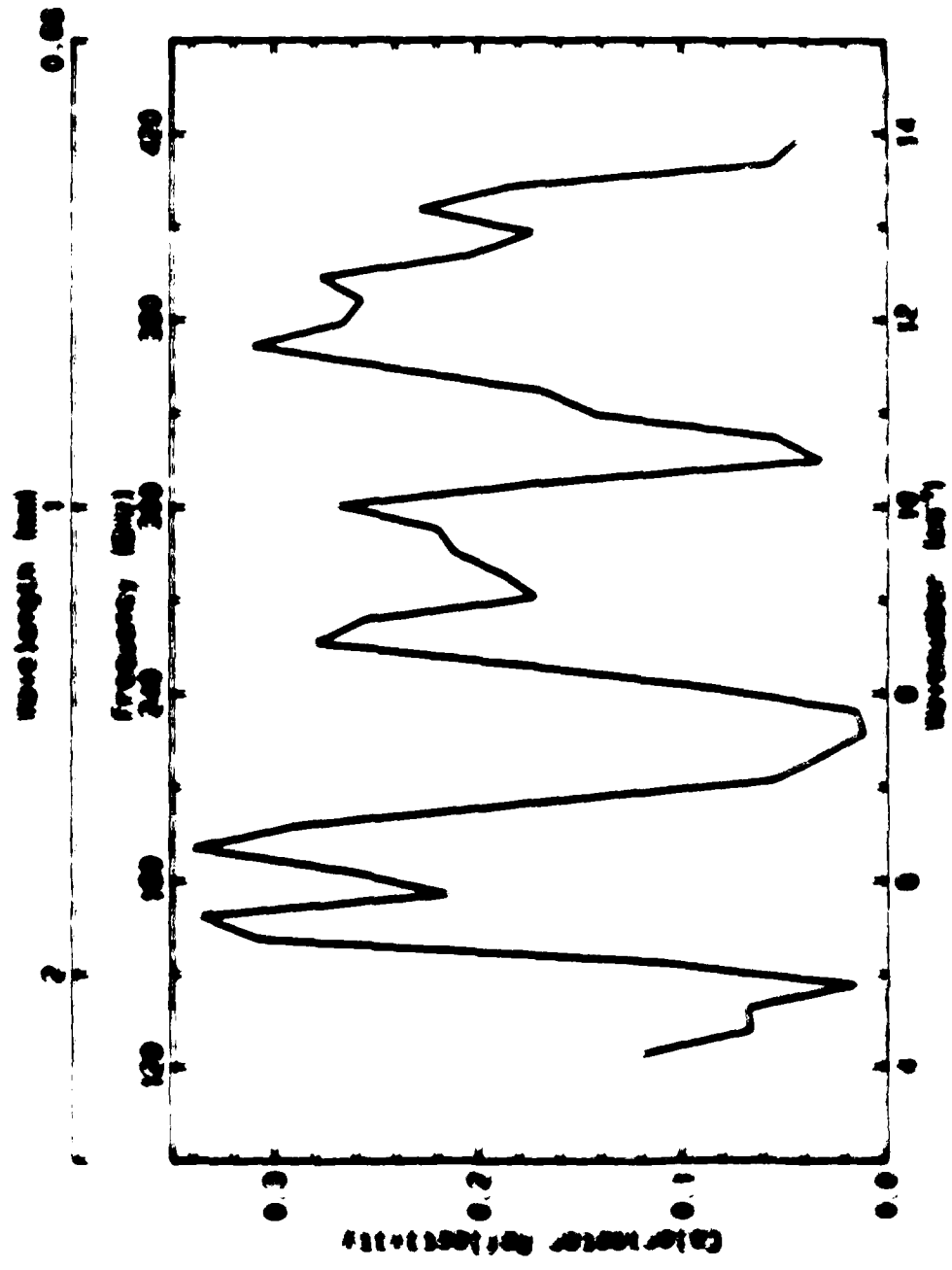


Fig 2.5b Dispersive Fourier Transform Spectroscopy Reflectivity Plot
of the 1 inch Strimber's Calorimeter



of the reflectivity from one. The resulting values from the four such calculations yielded $R_1 = 0.66$ for the 11_{111} at 211 Cells and $R_1 = 0.73$ for the 11_{111} at 209 Cells. The one such calculation was only used to measure power in the 11_{111} mode and it produced an R_1 value of 0.93 at 211 Cells.

The assumption in this calculation of R_1 is that the power which is not reflected is absorbed by the calorimeter. This should be completely valid in the case of the four such calorimeters because in each a thermal backing to the detector face preventing the RF from being re-emitted. This could not be stated with complete certainty for the one such calorimeter because the backing was defective allowing the possibility of some small fraction of the power to not be reflected or absorbed but re-emitted instead. This effect was probably minor as verified by the similarity between the four such solid one half power measurement results. Additionally, any errors in the one such calorimeter data due to this possibility would result in lower than actual power measurement results.

During the power measurements the calorimeters were placed 4 to 6 inches from the end of the antenna boresight. For the one such solid one half power measurement the antenna boresight was 100 inches from the calorimeter. The antenna boresight was 100 inches from the calorimeter. The boresight of the plug allowing the calorimeter to radiate. For the four such calorimeter systems placed 4 to 6 inches from the antenna boresight, some power would be lost from between the calorimeter and antenna boresight. The calculation of the antenna reflection from the plug was represented by R_1 in equation 2.7. It was simplified by assuming the

incidence since the plexiglass face was 90° to the waveguide axis. The expression for K is then given by

$$K = \left(\frac{n^2 - 1}{n^2 + 1} \right)^2 \quad (2.6)$$

where n is the index of refraction. The $(1 - K)^2$ term in equations (2.4) and (2.5) did not have to be substituted for $(1 - K)$ since the fundamental of several reflections because the index of refraction was for consideration considered to be constant over the frequency range considered. The waves is squared since both surface reflections upon entering and exiting the plexiglass must be considered. Using the value of $n = 1.500$ for plexiglass measured by H. H. Wood and W. D. Woodson in the letter to $K = 0.047$ from the previous section using equation (2.6).

The remaining factors required in the determination of R are the plexiglass absorption coefficients α_1 and α_2 . Values were determined here because the absorption coefficients are frequency dependent. However, the dependence is known to generally follow an ω^{-2} relationship for frequencies in the frequency range. This was verified by reading some data from the literature. The values were $\alpha_1 = 0.0004 \text{ cm}^{-1}$ for 10^8 Hz and $\alpha_2 = 0.0001 \text{ cm}^{-1}$ for 10^{10} Hz . The values for α_1 and α_2 were 0.0004 cm^{-1} for 10^8 Hz and 0.0001 cm^{-1} for 10^{10} Hz .

These values were checked experimentally by a method discussed in Section 2. For measuring the α values, a horn of the fundamental mode with the generator and detector were used as separate components as previously mentioned. The signal was then the plexiglass. The two measurements were subtracted to give the signal in the 10^8 Hz and 10^{10} Hz frequency range. The values for α_1

of plexiglass were placed between the source and receiver, and the attenuation was reduced to produce the same double output voltage. The calibration of the dial attenuator converted this to a dB loss which was used to calculate α . The results were in general agreement with the scaled values and the differences did not indicate any trends toward being lower or higher than the predicted value. The variations indicated that absorption in the plexiglass pieces themselves probably accounted for most of the difference between the scaled and measured values.

All of the parameters required to calculate P_{sc} by equation (2.5) were now known with varying degrees of accuracy. The results of the power measurements are presented in Table 1.2 using all parameters used in the calculations. Since the calculation requires average power, the pulse power results were calculated by dividing the P_{sc} value by the pulse length, τ , and the repetition rate of 8.16 Mc. The range in power levels in the test section were produced by inserting a rather large amount of ~ 20 dB of loss which transmitted as described above were generally similar to those of the scaled values for the frequency and incident characteristics. The variation in power level is due to the variation in the amount of range in output power and the variation in the loss coefficient. The present output power was calculated to be approximately 100 mW over the range of loss coefficients in the section.

The results of the calculations are shown in Table 1.2. The power levels of the first two columns are calculated using the loss coefficient and the range in the section. However, the power levels in the range of the absorption coefficient is probably useful to compare the results. The calculated average power is of the same order or greater than the measured value except for the ~ 20 dB loss. The loss coefficient was calculated for the

Table 3.2 Second Harmonic Power Measurements

TE_{11,1,1} Mode 241.02 GHz 1 inch Calorimeter

$$V = 6124V \quad A_1 = 0.93 \quad a_1 = 0.216 \text{ cm}^2 \quad a_2 = 1.27 \text{ cm}^2$$

<i>I</i> (A)	<i>i</i> (power)	<i>P₁</i> (mW)	<i>P₂</i> (mW)	<i>t</i> (cm)	POWER (kW)	RANGE (kW)
6.00	1.0	98	33	3.00	24	23-28
6.00	1.0	112	123	1.68	29	26-30
6.00	1.0	112	13	2.54	28	27-30

TE_{11,1,1} Mode 241.02 GHz 4 inch Calorimeter

$$V = 6124V \quad A_1 = 0.66 \quad a_1 = 0.216 \text{ cm}^2 \quad a_2 = 1.27 \text{ cm}^2$$

<i>I</i> (A)	<i>i</i> (power)	<i>P₁</i> (mW)	<i>P₂</i> (mW)	<i>t</i> (cm)	POWER (kW)	RANGE (kW)
6.00	1.0	55	81	1.91	29	28-40
5.00	0.95	50	80	2.54	20	20-23
6.00	0.95	65	100	1.91	20	20-26

TE_{01,1,1} Mode 209.43 GHz 4 inch Calorimeter

$$V = 11124V \quad A_1 = 0.27 \quad a_1 = 0.212 \text{ cm}^2 \quad a_2 = 0.902 \text{ cm}^2$$

<i>I</i> (A)	<i>i</i> (power)	<i>P₁</i> (mW)	<i>P₂</i> (mW)	<i>t</i> (cm)	POWER (kW)	RANGE (kW)
6.00	1.8	63	150	1.91	15	15-19

of the lack of significant simultaneous fundamental oscillation. For the $TE_{11,2,1}$, the second harmonic power accounted for 90-95% of the total output power. This percentage was slightly lower in the case of the $TE_{9,2,1}$, with 78% attributable to the second harmonic mode.

Considering the range of values listed in Table 3.2, the output power claim of 25-3 kW at 241 GHz in the $TE_{11,2,1}$ is justified. It is this value which appears on Figure 1.1b showing gyrotron performance at harmonics. This result at 6 amps corresponds to an overall efficiency $\eta \approx 6.7\%$. It is unknown if the slightly lower output powers measured at 7 A for the $TE_{11,2,1}$ are due to day-to-day variations in gyrotron performance or a physical effect such as mode suppression at higher current values. The $TE_{9,2,1}$ output power value of ≈ 15 kW translates to an overall efficiency of approximately 3.5%.

Chapter 4

Discussion of the Results

In view of the theoretical calculations concerning the overmoded nature of the 0.3.1 cavity, the most striking aspect of Table 3.1 is the limited number of second harmonic modes that were experimentally identified. Less than one third of the modes predicted to be above threshold by the linear theory results in Chapter 2 were actually observed. Similarly, the efficiencies predicted to be on the order of 23% did not exceed 7%. The primary purpose of this chapter will be to present possible explanations for the lower than theoretical levels of second harmonic emission. A secondary objective will be the consideration of which modes were excited. Although the eight modes which were present were all predicted to be above threshold, they were not the eight with the lowest calculated starting currents or the highest efficiencies. The predominant question is what physical reasons exist which could account for the missing second harmonic modes and lower than expected efficiencies.

Because the theoretical predictions of Chapter 2 considered only the resonator geometry, the problem of radiation loss or absorption at the output window or

in coupling with the output waveguide was not considered. The quartz output window was specifically designed for the 140 GHz radiation of the fundamental. It is unknown exactly how much increased reflection or absorption may be occurring in the window at the higher second harmonic frequencies. Increased reflection would raise the Q and change the theoretical calculations and increased absorption would obviously lower the measured radiation levels.

The guiding center radius r_c and ratio $\beta_{\perp} / \beta_{\parallel}$ are parameters which enter into both the linear and nonlinear theory calculations, yet they were not measured directly in this experiment. The values which were used in the starting current and efficiency calculations were design figures based on electron gun computer simulations and adiabatic theory. As an example of how a reasonable change in these parameters could affect the differences between theory and experiment, equation (2.32) shows that $I_{s\tau} \sim (\beta_{\perp} / \beta_{\parallel})^{-2}$ for the second harmonic. With the design value of $\beta_{\perp} / \beta_{\parallel} = 1.49$, the $TE_{11,2,1}$ mode has a predicted value of $I_{s\tau} = 0.66$ A. However, if the actual ratio of $\beta_{\perp} / \beta_{\parallel} = 2.0$, the change would yield $I_{s\tau} = 0.37$ A which is in much better agreement with the experimentally measured starting current of 0.2 A for the $TE_{11,2,1}$ mode. A consideration of this sort will be analyzed in Section 4.1 concerning the value of the guiding center radius r_c .

This example is a simple illustration of how a change in one parameter value could account for some of the difference between theory and experiment in the starting current for one isolated mode. In general, the increase in $\beta_{\perp} / \beta_{\parallel}$ mentioned would prove counter to the overall observation of lower than predicted levels of second harmonic emission and reduced efficiencies. This chapter will

analyze physical reasons which could explain the general trend. The discussion will focus on two separate phenomena as possible explanations. The first will be beam radius effects including the actual beam placement and the consideration of the finite beam width in calculations. The second topic, which will be discussed in Section 4.2, is the possibility of mode competition between fundamental and second harmonic modes as well as between neighboring second harmonic modes.

4.1 Finite Beam Width Effects

Examination of Table 3.1 listing the observed second harmonic modes reveals a trend in the radial mode index p . With the exception of the $TE_{4,5,1}$, each mode identified had radial mode numbers of $p = 2$ or $p = 3$. The linear theory analysis forecast modes above threshold with $2 \leq p \leq 7$, and predicted the modes with $p = 4$ to have the lowest starting currents. This discrepancy prompted consideration that the beam radius was possibly different from the value used in the theoretical work, or some other interaction was occurring based on the radial thickness of the beam which would suppress the higher order radial modes.

The guiding center radius (r_c) enters into both the linear theory starting current calculations from equation (2.32) and the nonlinear theory calculations of I_{τ} in equation (2.68) by the same G factor defined in equation (2.28). This term represents the efficiency of interaction between the electron beam and the RF fields. It is actually only the numerator of G which measures the strength of interaction by $G \sim J_{m;n}^2(k_c r_c)$, with the denominator representing the mode stored energy. Since $I_{\tau} \sim G^{-1}$ and $I_{\tau} \sim G$, an increase in G lowers the starting currents and increases I_{τ} . This increase in I_{τ} results in an increase in the predicted

value of η throughout the range of physically realizable beam currents in the MIT gyrotron. The discussion in this section will consider the physics which could account for an effective lowering of the G factor, thereby raising the starting currents and reducing the predicted second harmonic emission. Although the focus will be on raising the starting currents, the same arguments will result in lower theoretical efficiencies by the L_{τ} parameter used in the slow time scale theory.

The minimum beam radial thickness is two Larmor radii ($2r_L$). The actual thickness is greater due to the finite size of the electron emitter strip, space charge and other effects. The simplification which allowed determination of G by analytic methods was that the interaction could be represented using an infinitely thin annular beam with radius r_L , so it is reasonable to assume that some physics considerations were lost by discarding the radial beam thickness. For the MIT gyrotron, the electron beam width (thickness) predicted by computer calculations is $3.5 r_L$. Since $r_L = r_0 / 2.0$, it is evident that the beam thickness was changing throughout the experimental magnetic field scan. Using the field values listed in Table 2.2a, the beam widths range from 0.063 cm for the $TE_{1,2,1}$ mode at 4.054 T to 0.042 cm for the $TE_{1,2,1}$ mode at 6.047 T. An average value for the beam width of approximately 0.05 cm represents $\approx 25\%$ of the $r_0 = 0.197$ cm value used in the theoretical calculations.

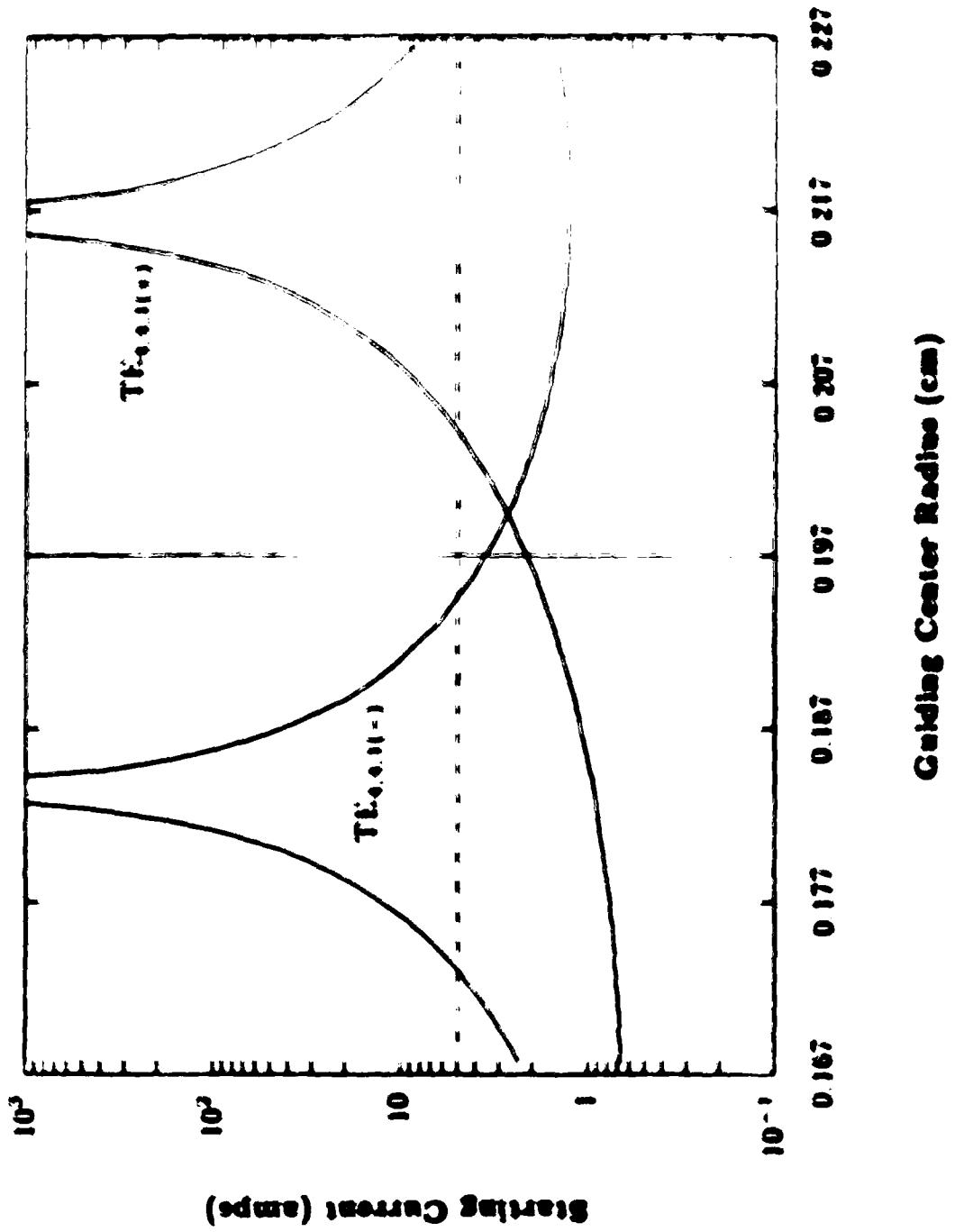
Figure 4.1 is representative of the extent of variation in calculated starting current which would result by using different values of r , within the range of beam thickness. The two modes represented are the two senses of opposite azimuthal rotation for the $TE_{4,4,1}$. The presented values of L_{τ} are valid at $B = 4.356$ T as

listed in Table 2.2a. The beam width at this magnetic field value is 0.050 cm, so the edges of the plotted lines at 0.168 cm and 0.226 cm represent the inner and outer radial edges of the beam. The graph is centered on the value of $r_0 = 0.197$ cm which was used in the starting current and efficiency calculations in Chapter 2. The 2.1 amp value of I_{sc} for the $\text{TE}_{4,4,1}$ at 0.197 cm is the figure listed in Table 2.2a. The dashed horizontal line represents the nominal 5 amp operating current during the experimental investigation.

It appears obvious from Figure 4.1 that very little information concerning the beam interaction is gleaned from a simple calculation of I_{sc} based on the infinitely thin line at 0.197 cm. The plots extending above the graphed limit of $I_{sc} = 1000$ amps are actually infinities caused by the values of r_0 which result in $J_{z,0}^2(k-r_0) = 0$ in the denominator. A minor increase in r_0 of $\approx +0.007$ cm would place the calculated value of I_{sc} above the 5 amp line for the $\text{TE}_{4,4,1}$. The previous discussion concerning the degree of knowledge about the actual value of r_0 is now relevant since minor changes result in such major differences in calculated values of I_{sc} .

The diagram suggested two possible improvements to the value of G to be incorporated into the starting current and efficiency calculations. The first step was simply an attempt at improving the accuracy of the assumed value of r_0 based on the actual experimental magnetic field values. The second approach involved taking the integral average of the G factor over the finite beam width to account for the changes in the interaction strength with different segments of the beam.

Fig 4.1 - TE_{0,0,1} Mode Starting Current as a Function of r .



The adiabatic theory which is used in calculating values of ϵ in the cathode region results in a scaling law based on the value of the magnetic compression which is defined as the ratio of magnetic field value at the anode to its value at the cathode. The guiding center radius r is essentially proportional to the square root of the magnetic compression. Except maintaining the same field value will not change the radius if the compression factor stays constant, but experimentally the gun ions which add to the field in the cathode region were adjusted along the magnetic field axis to improve the ϵ value. The added factor will generally result in changes in the compression factor and therefore ϵ .

Table 1.1 lists the actual magnetic field and gun ion settings recorded during the experiment. Beside the field values the resulting compression and beam radius are presented. The ϵ values listed are close to the 0.197 ϵ value used in Chapter 2 but as evidenced by Figure 1.1 only modest changes seem to be significant for some modes. The general trend evident from the experimental analysis of test and gun ion fields is for increasing compression and gun ion beam radius for the higher field modes. This trend was experimentally observed in Table 2.2a and new values of ϵ were calculated using the same ϵ versus r relationship.

The results of these calculations are shown in Table 1.2. The value of ϵ is listed as well as the resulting change in beam radius. The last two entries in Table 1.2 are related to the ϵ to beam width calculations and will be discussed shortly.

Although it has been shown that a change of less than 0.01 ϵ could result in significant changes in r , this did not appear to be the case for the

Table 2.1. *Adaptation: Theoretical Maximum Number of Individuals per Cell*
for Different and Constant Maintenance Ratios

MAINTENANCE RATIO	THEORETICAL MAXIMUM NUMBER OF INDIVIDUALS PER CELL	THEORETICAL MAXIMUM NUMBER OF INDIVIDUALS PER CELL	THEORETICAL MAXIMUM NUMBER OF INDIVIDUALS PER CELL
1:1	0.10000	27.4	0.274
1:2	0.10000	27.4	0.274
1:3	0.10000	27.4	0.274
1:4	0.10000	27.4	0.274
1:5	0.10000	27.4	0.274
1:6	0.10000	27.4	0.274
1:7	0.10000	27.4	0.274
1:8	0.10000	27.4	0.274
1:9	0.10000	27.4	0.274
1:10	0.10000	27.4	0.274

Table 2.2 Adjusted U.S. County-level Accounting Estimates
Including District System Health Forces

U.S. COUNTY-LEVEL ACCOUNTING ESTIMATES
INCLUDING DISTRICT SYSTEM HEALTH FORCES

STATE	1980	1981	1982	1983	1984	1985
AL	1.20	1.15	1.10	1.05	1.00	0.95
AK	0.00	0.00	0.00	0.00	0.00	0.00
AZ	1.10	1.05	1.00	0.95	0.90	0.85
CA	1.50	1.45	1.40	1.35	1.30	1.25
CO	1.00	0.95	0.90	0.85	0.80	0.75
CT	1.30	1.25	1.20	1.15	1.10	1.05
DC	0.00	0.00	0.00	0.00	0.00	0.00
DE	1.20	1.15	1.10	1.05	1.00	0.95
FL	1.10	1.05	1.00	0.95	0.90	0.85
GA	1.00	0.95	0.90	0.85	0.80	0.75
HI	0.00	0.00	0.00	0.00	0.00	0.00
IA	1.00	0.95	0.90	0.85	0.80	0.75
ID	1.00	0.95	0.90	0.85	0.80	0.75
IL	1.20	1.15	1.10	1.05	1.00	0.95
IN	1.10	1.05	1.00	0.95	0.90	0.85
KS	1.00	0.95	0.90	0.85	0.80	0.75
KY	1.10	1.05	1.00	0.95	0.90	0.85
LA	1.00	0.95	0.90	0.85	0.80	0.75
MA	1.30	1.25	1.20	1.15	1.10	1.05
MD	1.20	1.15	1.10	1.05	1.00	0.95
ME	1.10	1.05	1.00	0.95	0.90	0.85
MI	1.20	1.15	1.10	1.05	1.00	0.95
MN	1.00	0.95	0.90	0.85	0.80	0.75
MO	1.00	0.95	0.90	0.85	0.80	0.75
MS	1.00	0.95	0.90	0.85	0.80	0.75
MT	1.00	0.95	0.90	0.85	0.80	0.75
NC	1.10	1.05	1.00	0.95	0.90	0.85
ND	1.00	0.95	0.90	0.85	0.80	0.75
NH	1.10	1.05	1.00	0.95	0.90	0.85
NJ	1.30	1.25	1.20	1.15	1.10	1.05
NM	1.00	0.95	0.90	0.85	0.80	0.75
NY	1.30	1.25	1.20	1.15	1.10	1.05
OH	1.10	1.05	1.00	0.95	0.90	0.85
OK	1.00	0.95	0.90	0.85	0.80	0.75
OR	1.00	0.95	0.90	0.85	0.80	0.75
PA	1.20	1.15	1.10	1.05	1.00	0.95
RI	1.10	1.05	1.00	0.95	0.90	0.85
SC	1.00	0.95	0.90	0.85	0.80	0.75
SD	1.00	0.95	0.90	0.85	0.80	0.75
TN	1.10	1.05	1.00	0.95	0.90	0.85
TX	1.10	1.05	1.00	0.95	0.90	0.85
UT	1.00	0.95	0.90	0.85	0.80	0.75
VA	1.10	1.05	1.00	0.95	0.90	0.85
VT	1.10	1.05	1.00	0.95	0.90	0.85
WA	1.10	1.05	1.00	0.95	0.90	0.85
WI	1.10	1.05	1.00	0.95	0.90	0.85
WV	1.00	0.95	0.90	0.85	0.80	0.75
WY	1.00	0.95	0.90	0.85	0.80	0.75

NOTE: Percent with H

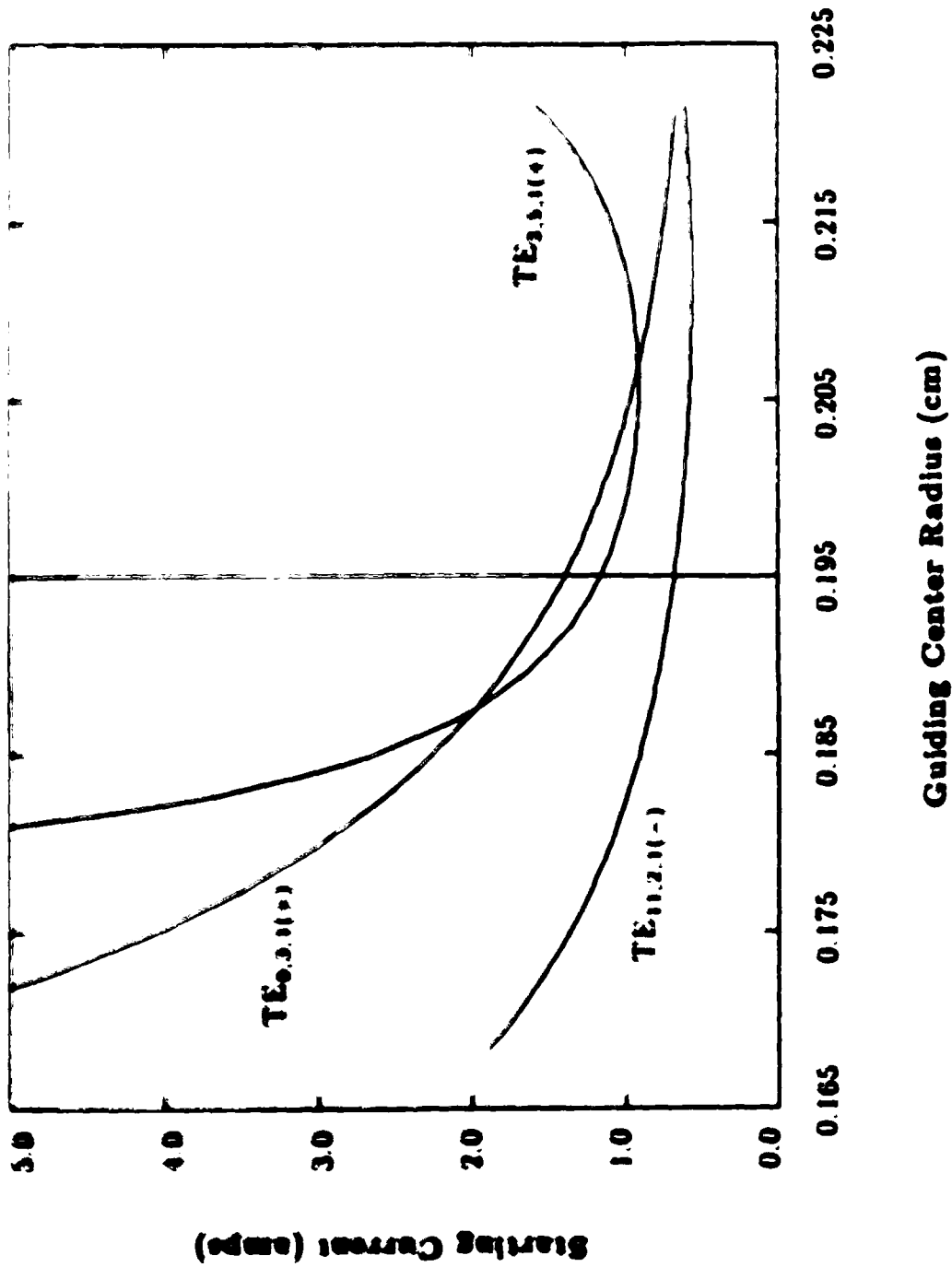
* Value was derived approximately

...the The

...the possibility of

...the

Fig. 0.3 Plot of β for the $TE_{0,2,0}(-)$, $TE_{0,2,0}(+)$, and $TE_{2,2,0}(+)$ Modes



it can be seen in the figure that the $TE_{2,3(1)}$ has a lower starting current value at $r = 0.195$ cm than the $TE_{4,5(1)}$. However, considering the full extent of the beam thickness, the $TE_{4,5(1)}$ should have a better overall interaction and lower starting current because the $TE_{2,3(1)}$ line exceeds the $TE_{4,5(1)}$ line over the greater portion of the beam width. It is apparent that the effect should provide better agreement with experiment by discriminating against higher order radial modes due to the increased number of nulls in the radial field structure for these large p modes.

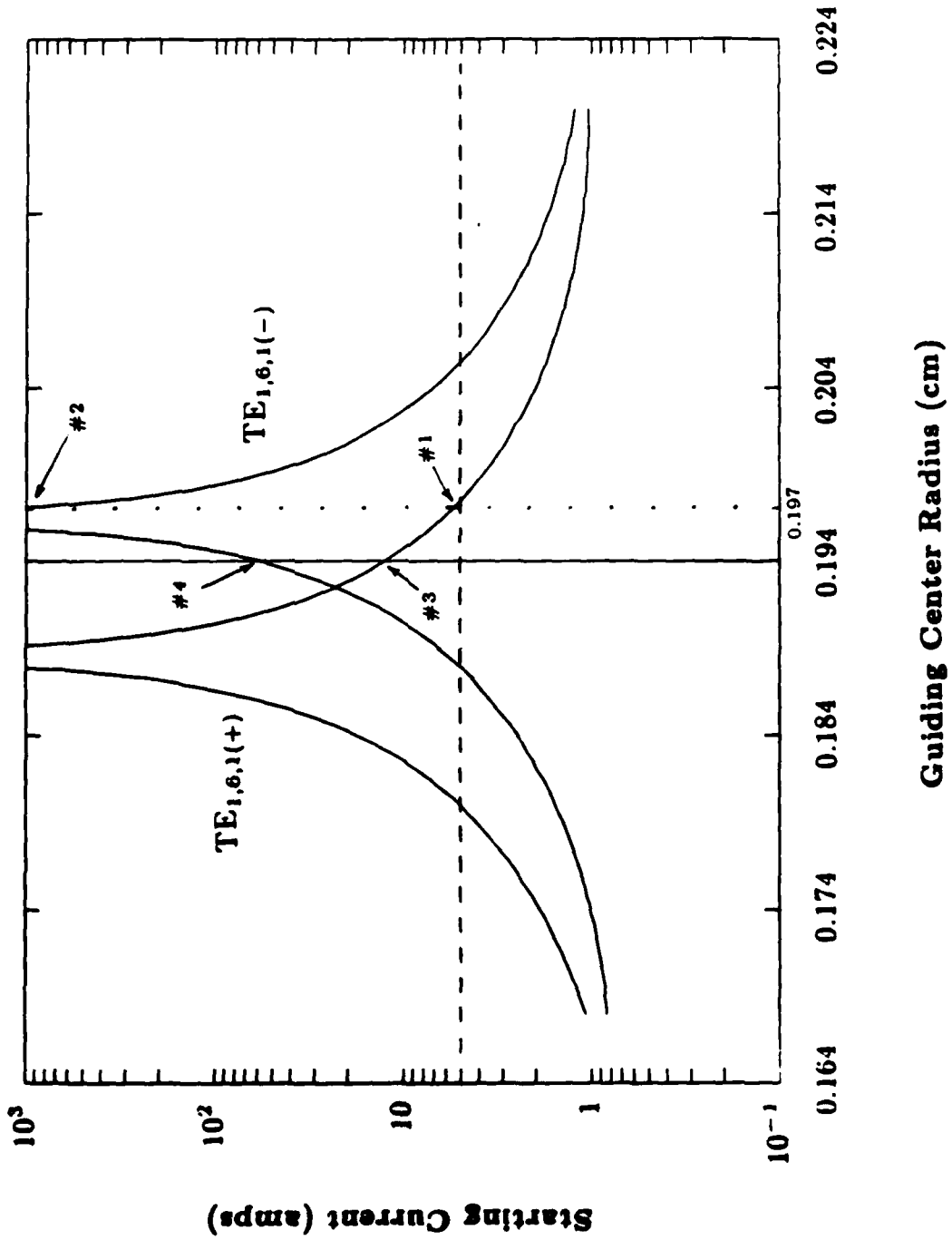
The third column in Table 4.2 lists the results of the starting current calculations using the beam width averaged k_z factor. For each value, the experimentally adjusted k_z listed in the first column was used as the factor used. The beam width was calculated as 2.5λ , based on the magnetic field value for each mode listed in Table 2.2a. The last column in Table 4.2 shows the difference between the I_{sc} values listed in the two previous columns as a percentage of the "theoretical" beam result in column two.

The averaging effect discussed qualitatively in relation to the graphed differences between the $TE_{2,3(1)}$ and the $TE_{4,5(1)}$ modes in Figure 4.2 are verified by the numbers in Table 4.2. The beam width factor lowered the theoretical starting current for the $TE_{2,3(1)}$ by 21% and raised the starting current for the $TE_{4,5(1)}$ by 22%. The $TE_{2,3(1)}$ has a lower starting current than the $TE_{4,5(1)}$ when calculated in this manner, which is the opposite of the "theoretical" beam results.

This limited apparent success is marred by the overall result that the finite beam thickness factor did not eliminate any modes by increasing their theoretical starting currents over the 5 amp experimental operating current. It actually added the $TE_{1,0,1}$ mode to the list of those predicted to be above threshold. In simple terms, the beam width averaging increased the starting current for the low starting current modes, but decreased I_s for the high starting current modes. The range of values of $0.11 \text{ A} < I_s < 2900 \text{ A}$ for the infinitely thin beam calculations was compressed to $0.48 \text{ A} < I_s < 310 \text{ A}$ with the beam width factor. Additionally, the factor did not always preferentially lower starting currents of the low radial modes and raise I_s for the higher order modes, as evidenced by the 96% reduction in I_s for the $TE_{1,1,1}$. This mode will serve as a useful summary for the beam radius considerations of this section and provide some insight into the apparent failings.

Figure 4.3 depicts the predicted starting current for the $TE_{1,0,1}$ modes at 1921 T. The left and right edges of the curves represent the inner and outer radial edges of the 3.5 σ_e beamwidth at this magnetic field value. The initial calculation of I_s for this mode in Chapter 2 produced $I_s = 56 \text{ A}$ for the $TE_{1,0,1}$. This value was based on a "thin" beam with $r_b = 0.197 \text{ cm}$ and is identified on Figure 4.3 with the =1. The starting current of the $TE_{1,0,1}$ at this value of r_b is $\approx 1000 \text{ A}$, indicated by the =2 on the graph. The improved estimate of $r_b = 0.191 \text{ cm}$ still showed the $TE_{1,0,1}$ as the lower starting current mode, but the value had more than doubled to $I_s = 13 \text{ A}$ which is depicted by the =3. The reduction in r_b from 0.197 cm to 0.191 cm resulted in I_s for the $TE_{1,0,1}$ mode increasing from

Fig 4.3 — $TE_{1,6,1}$ Mode Starting Current as a Function of r_c



1000 A $\rightarrow \infty$, then decreasing back down to the value of $I_{c\tau} = 56$ A, shown by the #4 in the diagram. Finally, the beam width averaged starting current values showed the two modes approximately equal with $I_{c\tau} = 2.3$ A for the $TE_{1,6,1(-)}$ and $I_{c\tau} = 2.2$ A for the $TE_{1,6,1(+)}$. Although the central region of the beam interacts very weakly with the fields as evidenced by the high "thin" beam $I_{c\tau}$ values, the inner and outer edges of the beam are positioned to interact favorably, thus bringing the full beam width averaged starting current down to ≈ 2.2 A.

Since the two curves for the rotating modes are almost symmetric about the central value of $r_c = 0.194$ cm, it is reasonable to assume that their interaction with the fields over the full beam width would be similar. The beam width averaged starting current calculations support this, whereas the delta function view of the beam radius yields orders of magnitude differences in the predicted starting currents for the two senses of rotation. It is felt that the averaged values are more physically realistic, even though the $TE_{1,6,1}$ mode was not observed experimentally. The lack of mode excitation is probably due to phenomena unrelated to beam radius effects.

A possibility not considered in the theoretical calculations is that there may be standing wave structures in the cavity as opposed to the rotating waves assumed for the nonazimuthally symmetric modes. This would lower the predicted interaction because of electromagnetic field nulls in the azimuthal direction which do not exist if the wave is rotating. Experimental measurements of the far field pattern indicate that there are rotating modes, but this does not preclude the possibility of standing wave modes.

Although possible improvements to the averaging technique, such as including a spatial distribution function for the electrons, might yield minor improvements, the limited success at predicting experimental results suggests consideration of different explanations. The degree of success of the finite beam width considerations is limited to the range of applicability for the theories covered in Chapter 2. These were single mode analyses, so the failure of the beam width corrections to account for the experimental observations is possibly due to the failure of the theory itself, if multimoding or mode competition effects were present. These possibilities are discussed in the following section.

4.2 Mode Competition

Theoretical analyses of multimoding and mode competition in gyrotrons have been conducted previously, such as the investigations by G. S. Nusinovich [55] and Kreischer et al. [56]. These studies have shown that the phenomena can have significant impact on the mode oscillation characteristics of gyrotrons. Nusinovich cites three primary manifestations of multimoding, these being mode suppression, mode enhancement and mode locking. Of the three, mode suppression is the dominant effect for modes which have close oscillation frequencies. This is characterized by an actively oscillating mode limiting the oscillation of nearby modes which might otherwise be above threshold. The predictions of these events are clearly outside the realm of the theories presented in Chapter 2. In a similar manner, the existence of mode competition effects could severely reduce the accuracy of the calculations based on those theories.

The study by Kreischer and coworkers cited above, included an experimental investigation of multimoding at the fundamental with the same 0.3.1 cavity used in this study. There were large areas of mode overlap which were predicted by theory and supported by the experimental results. Additionally, the fact that the $TE_{0,2,1}$ mode never fully achieved the high efficiencies otherwise predicted was attributable to its oscillation zone overlap with the $TE_{2,3,1}$ mode.

In the present study, the diode signal traces such as those shown in Figure 3.2, confirm the existence of multimode oscillation between fundamental and second harmonic modes. Additionally, the simultaneous frequency measurement of the $TE_{11,3,1}$ and $TE_{15,2,1}$ modes at the same magnetic field value, is a clear example of multimoding between second harmonic modes. The existence of this multimode oscillation points to the possibility of mode suppression or enhancement between fundamental and second harmonic modes, or between separate second harmonic modes.

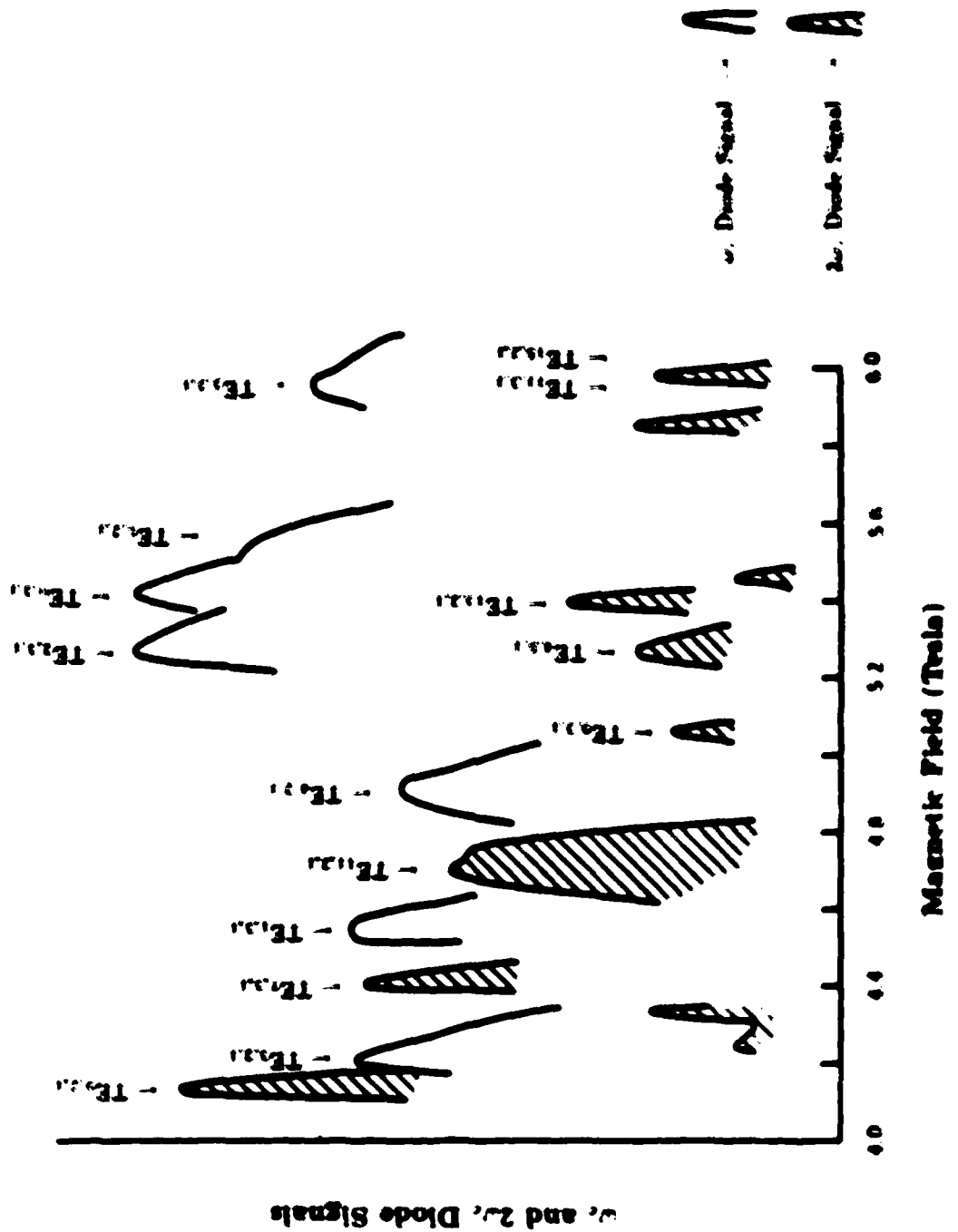
The mode competition theory developed by Nusinovich is valid for arbitrary harmonics, but analytic methods for applying the theory have only been developed at the fundamental with some simplifying assumptions, such as a uniform distribution for the axial field profile. Quantative methods are therefore not available for a detailed analysis of the effects of multimoding at the second harmonic or mode competition between fundamental and second harmonic modes. However, qualitative arguments will be presented as well as the experimental evidence.

In a magnetic field region which supports both fundamental and second harmonic modes, the fundamental will generally begin oscillation prior to the second

harmonic because it has higher gain, a lower starting current and a wider excitation range. This has been experimentally confirmed. An example of this phenomenon is shown in Figure 3.2, where the fundamental $TE_{2,3,1}$ diode signal turns on earlier and has a longer pulse length than the second harmonic $TE_{4,5,1}$ mode. Although the second harmonic mode may still oscillate, the established fundamental mode will tend to deplete the available electrons which might otherwise exchange energy with the second harmonic. The result would be reduced efficiency and output power at the second harmonic from that which would be predicted in the absence of the fundamental mode.

The experimental results of this study appear to support this idea, in particular the case of the fundamental suppressing the second harmonic emission. Figure 4.4 reproduces the magnetic field scan diode signal plots from Figures 3.3a and 3.3b. Both ω_c and $2\omega_c$ diode signals are shown on the same graph, so the vertical scale has been eliminated to avoid misleading estimates of relative mode strength. As mentioned in Chapter 3, relatively few conclusions may be drawn concerning output power by the diode signal even from the same diode, yet the $TE_{11,2,1}$, $TE_{12,2,1}$ and $TE_{7,2,1}$ modes provided the most consistently stable diode signals at the second harmonic. The higher magnetic field $2\omega_c$ modes, $TE_{2,2,1}$ through the $TE_{13,2,1}$, were generally characterized by erratic, low level diode signals, present over a much more limited range of magnetic field and gun coil settings. As seen in Figure 4.4, these high magnetic field, low level $2\omega_c$ modes occur at the same field values as significant levels of fundamental radiation, in particular the $TE_{2,2,1}$, $TE_{3,2,1}$ and $TE_{5,2,1}$ modes. By contrast, the consistently stable $TE_{11,2,1}$,

Fig 4.4 - $\omega_c \approx 2\omega_0$ Mode Competition



Note: Peak height is not indicative of output power level.

$TE_{0,2,1}$ and $TE_{7,5,1}$ modes oscillate in gaps in the measured fundamental spectrum. This general behavior could be predicted based on the mode suppression analysis of the previous paragraph. The magnetic field region above 5.0 T shows a number of $2\omega_c$ modes above threshold on Figure 2.3a which were not observed experimentally. The dominant fundamental oscillation in this high field region could explain the number of missing second harmonic modes.

An argument similar to the one offered previously concerning the inability of the $TE_{0,2,1}$ to reach the high efficiency zone due to mode switching to the $TE_{7,5,1}$ could apply to the $TE_{11,2,1}$. Perhaps the magnetic field detuning required to achieve the 23% efficiency predicted by theory is unachievable because the $TE_{0,2,1}$ shown on Figure 4.4 suppresses the $TE_{11,2,1}$ at those field values.

The comparison of ω_c and $2\omega_c$ diode signals shown here allows consideration of mode competition between fundamental and second harmonic modes. A more difficult phenomenon to consider is the possibility of mode competition between neighboring second harmonic modes. The observed multimoding mentioned previously and the overlapping mode spectrum shown in Figure 2.3a certainly allow the possibility. The difficulty is the qualitative assessment of mode competition between the fundamental and second harmonic generally prevents attributing specific results to mode competition between second harmonic modes.

One example of where the competition between second harmonic modes might account for a specific experimental observation is the presence of the $TE_{7,5,1}$ in place of the $TE_{1,2,1}$ mode. The $TE_{7,5,1}$ provided a fairly stable $2\omega_c$ signal in a region with limited fundamental oscillation. However, as shown in Figure 2.3a, the

Tl₂O₃ was predicted to be alkali or approximately the water field value, and with a slightly lower starting current and higher efficiency. The fact that the Tl₂O₃ was never observed, even though the indicated substitutional emission might have allowed it, points to the possibility of anode suppression by the Tl₂O₃.

The substitutional and anode suppression phenomena discussed here serve to present the most reasonable explanations for the lower than theoretical levels of second harmonic emission. It is clear that anode suppression studies and a quantitative analysis would be required for more definite conclusions.

Chapter 3

Higher Harmonics

The discussion thus far has been based on the theoretical and experimental considerations of the second harmonic. This chapter is all devoted to the experimental considerations of higher harmonics and efficiency for modes with $v = 2$.

Experimentally no modes at harmonics higher than the second were observed. The second harmonic diode described in Chapter 2 was operated for the 220-125 GHz band. Only third harmonic signals in the low magnetic field region would be within this frequency range. However, it is reasonable to assume that there would be some response to radiation at frequencies of 300 GHz or higher just as the fundamental diode at 100 GHz would show a strong response to the 200 GHz out-of-band second harmonic signal. Additional to the harmonic mixing system used for the frequency measurements identified several harmonic modes at frequencies as high as 300 GHz using harmonics of the local oscillator (LO) up to 20. There was no indication that the mixer would not have responded to much higher frequency signals with $v = 20$ or more.

Table 2.3. *U.S. Shipping Lines - 1960*

Line	Flag	Home Port	Q1	Q2	Q3
Alcoa	U.S.	New York	1000000	1000000	1000000
Alcoa	U.S.	New York	1000000	1000000	1000000
Alcoa	U.S.	New York	1000000	1000000	1000000
Alcoa	U.S.	New York	1000000	1000000	1000000
Alcoa	U.S.	New York	1000000	1000000	1000000
Alcoa	U.S.	New York	1000000	1000000	1000000
Alcoa	U.S.	New York	1000000	1000000	1000000
Alcoa	U.S.	New York	1000000	1000000	1000000
Alcoa	U.S.	New York	1000000	1000000	1000000

Table 3.2 0.3.1 Cavity $v = 1$, Starting Currents

Model	v (MHz)	Distance	Q_1	Q_2	I_{s1} (amps)
TE _{10,10}	15.15	1.55	22700	25400	140
TE _{10,10}	15.16	1.56	23000	26000	14
TE _{10,10}	15.17	1.57	23300	26300	12
TE _{10,10}	15.18	1.58	23600	26600	12
TE _{10,10}	15.19	1.59	23900	26900	10
TE _{10,10}	15.20	1.60	24200	27200	13
TE _{10,10}	15.21	1.61	24500	27500	21
TE _{10,10}	15.22	1.62	24800	27800	230
TE _{10,10}	15.23	1.63	25100	28100	70
TE _{10,10}	15.24	1.64	25400	28400	2700000
TE _{10,10}	15.25	1.65	25700	28700	54
TE _{10,10}	15.26	1.66	26000	29000	67
TE _{10,10}	15.27	1.67	26300	29300	20

magnetic field range, slightly more than one half of all possible third harmonic modes would be oscillating at five amps and 64.3 kV beam voltage.

The fourth harmonic results listed in Table 5.2 show no modes above threshold at five amps beam current. The minimum starting currents in this case are on the order of 5.4 A. The lack of any predicted oscillation at the fourth harmonic eliminated the need for consideration of modes with $n = 4$.

Efficiencies were calculated for the third harmonic modes predicted to be above threshold using the slow time scale nonlinear theory described in Chapter 2. Specifically, the short integration length of $\frac{1}{2} \mu$ to $\frac{3}{2} \mu$ was used. This nonlinear theory generally predicted the highest efficiencies when compared with the long integration lengths and the fast time scale theories also used in Chapter 2. The results of the third harmonic efficiency calculations are presented in Table 5.3 for $V = 64.3$ kV and $I = 5$ A.

The third harmonic perpendicular efficiencies (η_{\perp}) were surprisingly high for the modes considered. As seen in the table, 21% η_{\perp} = 11%. However, the low ohmic Q factors relative to the diffractive Q 's for the $n = 3$ modes significantly reduced the output efficiencies to the 10% η_{\perp} = 5% range. Obviously no efficiencies could be calculated for fourth harmonic modes at five amps since they were all below threshold, however the efficiency was calculated for the TE_{14,0,10} at 7 amps using the same slow time scale theory. The predicted value of η_{\perp} was 6.0% resulting in an overall efficiency $\eta = 3.3\%$.

**Table 8.3 0.3.1 Cavity - 8.3. Efficiency Calculations
Nusimovich and Erm 1972**

MODE	Integral Length of $\frac{1}{\lambda} \mu$			
	μ	$l \cdot 10^3$	η (%)	η (%)
TE _{10,1}	25.20	9.862	17	77
TE _{11,1}	25.25	6.295	12	54
TE _{10,2}	26.02	10.52	20	95
TE _{2,1}	26.12	6.095	12	57
TE _{10,3}	26.16	10.71	21	88

The lack of any observed third harmonic emission is probably due to mode suppression considerations as discussed in the previous chapter. Both the fundamental and second harmonic modes have higher gain and should suppress the third harmonic oscillation. The modes listed in the Tables 5.1-5.3 should occur at ≈ 4.8 T, but this coincides with the second harmonic $TE_{11,2,1}$ mode. As seen in Figure 4.1, there are no magnetic field regions between 4.0-6.0 tesla where there is neither fundamental nor second harmonic emission, thereby making third harmonic oscillation unlikely. The results in Tables 5.1-5.3 based on the single mode analysis did not consider these mode competition possibilities.

Chapter 6

Conclusions and Recommendations

The present study has confirmed the existence of second harmonic emission from a high power, high frequency gyrotron designed for the fundamental. The second harmonic radiation was within the high efficiency zone, resulting in approximately 25 kW of output power at 241 GHz. The linear and nonlinear theories which were applied indicate that efficient second harmonic emission will be the general result rather than the exception in overmoded, high power gyrotrons. Future megawatt power level gyrotrons, designed for operation at the fundamental, will have to consider the effects of this harmonic oscillation or develop methods for suppressing these modes.

The harmonic emission observed in this investigation was identifiable as cavity modes. That is, each mode frequency $\omega \approx 2\omega_0$ could be predicted based on the scaling of the Bessel function zero, ν_{mp} . The distinction here is between these cavity modes and parametric effects which have recently been identified in the radiation from a 28 GHz, cw Varian gyrotron to be used for ECRH on the TARA tandem mirror experiment at MIT. These latter, parametric effects

are characterized by a second harmonic frequency measured as exactly twice the frequency of an oscillating fundamental mode. Experimental work is continuing to investigate this phenomenon, and separate physics issues are involved than with the cavity modes found in the gyrotron used for this study.

6.1 — Summary and Further Conclusions

The theoretical investigation separately considered two different resonator cavities. The 0.3.1 cavity was designed for scaling up to megawatt power levels and cw applications. The relatively small beam radius to wall radius ratio naturally yielded a dense mode structure, with the possibility of 36 second harmonic modes between 4.0 and 6.0 tesla. The whispering gallery cavity was designed for reduced mode competition at the fundamental, and the larger beam to wall radius ratio allowed a relatively sparse spectrum, with only half the possible $2\omega_c$ modes as the 0.3.1 cavity over the same magnetic field range. For both cavities, the CAVRF computer code predicted the 4.0-6.0 tesla second harmonic mode frequencies to be in the 203-303 GHz range.

A linear analysis determined the threshold of oscillation conditions for the $2\omega_c$ modes in both cavities. The second harmonic spectrum of the 0.3.1 cavity was predicted to be heavily overmoded, with 28 of the 36 possible modes in the 4.0-6.0 tesla range having starting currents of less than five amps. The whispering gallery cavity calculations showed a greatly reduced mode spectrum, with only seven modes predicted to be above threshold at a beam current of five amps. Similarly, the minimum theoretical starting currents were lower for the 0.3.1 cavity, with

$I_{sT} \approx 0.5$ A. as opposed to the whispering gallery resonator which had a minimum $I_{sT} \approx 3.5$ A.

The nonlinear theory was employed for efficiency calculations for all the second harmonic modes predicted to be above threshold by the linear analysis. A slow time scale formulation allowed efficiency calculations from computer generated graphs, based on the assumption of a Gaussian longitudinal field profile. Application of the slow time scale theory only required calculating the normalized operating current I_o and normalized cavity length μ . The second harmonic modes predicted to be above threshold in the 0.3.1 cavity had total efficiencies ranging from 10-25%. The whispering gallery cavity slow time scale theoretical results were in the 5-10% efficiency zone. A fast time scale computer code using the cold cavity CAVRF field profile was also employed for efficiency calculations. The resulting efficiencies were lower than the slow time scale values by 2-10 percentage points for both the 0.3.1 and whispering gallery cavities.

Starting currents and efficiencies were calculated for a limited number of third and fourth harmonic modes using the 0.3.1 cavity. The lowest third harmonic starting currents were approximately 2 A and the fourth harmonic had the lowest values of $I_{sT} \approx 5.4$ A. The results indicated that slightly more than half of the third harmonic modes between 4.0-6.0 tesla should be above threshold at five amps. A very small percentage of the fourth harmonic modes should be excited at that beam current. Output efficiencies for the third harmonic modes were calculated to be in the 5-10% range using the slow time scale nonlinear theory.

The final theoretical analysis was a scaling estimation for second harmonic efficiency based on operating parameters at the fundamental. The slow time scale efficiency plots provided an easy method of mapping regions of interest at the fundamental to the appropriate efficiency zone at the second harmonic. The method supported the quantitative results of the 0.3.1 cavity by predicting high efficiencies at the second harmonic. An example presented for a device optimized at the fundamental showed a remarkably constant, high level of second harmonic efficiency, even to the point where the fundamental efficiency had decreased by approximately 30%. This motivates the concern over harmonic emission for low ohmic loss, low Q , overmoded resonators designed for fundamental operation.

The experimental investigation was designed to confirm the predicted existence of the harmonic emission and provide some test of the theoretical calculations for the 0.3.1 cavity. A magnetic field scan over the 4.0-6.0 tesla range at 64.3 kV and with 5 amps of beam current was conducted, using video diodes to detect both fundamental and second harmonic emission. Eight $2\omega_0$ modes were identified by an harmonic mixing frequency measurement system, with the frequencies generally within 0.1% of the predicted CAVRI values. This mixing system proved to be invaluable due to its accuracy and ability to measure low-level, erratic signals.

The starting current measured for the $TE_{11,2,1}$ mode was 0.2 A, which was a factor of three lower than the theoretical value, and of the same order as I_{τ} for fundamental modes. Power measurements of the $TE_{11,2,1}$ and $TE_{0,2,1}$ modes were

performed using calorimeters. The reflectivity of the calorimeters at these frequencies was analyzed using dispersive Fourier transform spectroscopy, and power discrimination between the fundamental and second harmonic was accomplished by using various thicknesses of plexiglass absorber. The results revealed the $TE_{11,2,1}$ mode producing ≈ 25 kW of output power at 241 GHz, with the $TE_{9,2,1}$ emitting ≈ 15 kW at 209 GHz. These results represent the highest output powers at high frequency (> 100 GHz) detected in a gyrotron operating at harmonics above the fundamental.

The detection of second harmonic emission and the power levels achieved represent the most significant aspects of this study. However, less than one third of the $\omega \approx 2\omega_c$ modes predicted to be excited were observed and the measured efficiencies were a factor of three lower than the theoretical values. Additionally, no higher harmonic ($n > 2$) modes were observed although a number of third harmonic modes were predicted to be above threshold. Two possible explanations for this difference were investigated. The first considered the possibility that a correction accounting for the full finite electron beam width, and incorporated in the starting current and efficiency calculations, could effectively lower the theoretical second harmonic emission toward the experimentally measured values. Although it was felt that this correction was physically more realistic than the infinitely thin beam calculations, it did not succeed in predicting lower emission levels at the second harmonic.

The second consideration was that mode suppression could account for the decreased second harmonic mode spectrum and power levels. Multimoding was

experimentally verified between fundamental and second harmonic modes, as well as between separate second harmonic modes. The quantitative theory is only adequately developed for interaction between fundamental modes, but qualitative theoretical considerations support the view that an established fundamental mode will tend to prevent oscillation at 2ω . The experimental results contributed to this conclusion by showing the strongest second harmonic modes oscillating in gaps in the fundamental spectrum. It was difficult to estimate the degree of mode suppression caused by one second harmonic mode on another, but the overmoded nature of the cavity and observed $2\omega \leftrightarrow 2\omega$ multimoding definitely allowed the possibility of this type of competition. The qualitative assessment based on the experimental evidence was that the fundamental suppression of the second harmonic modes was the dominant effect.

6.2 Recommendations for Further Study

The investigation suggests there remains a great deal of experimental and theoretical analysis which could be done concerning the harmonic emission from high power gyrotrons designed for the fundamental. The experimental examination of the harmonic content of the whispering gallery cavity to compare with calculations already cited in this study would provide an obvious first step.

For the theoretical aspects, the most useful efforts would be toward increasing the immediate applicability of the mode competition theory to include $\omega_1 \leftrightarrow 2\omega_1$ and $2\omega_1 \leftrightarrow 2\omega_2$ effects. This difficult prospect would yield the immediate benefit of quantitatively testing the suppression which was qualitatively theorized in this analysis.

Finally, increased diagnostics at higher frequencies would allow a more thorough investigation at the third or higher harmonics. As shown in Chapter 5, the single mode analysis still allows reasonable efficiencies at $\omega = 3\omega_0$, but an extended mode competition theory would probably lower expectations significantly. As with the present study, an experimental investigation could confirm or deny the theoretical predictions as well as raise additional questions.

References

- 1 V. V. Alibekov, G. A. Babrovskii, V. I. Poznyak, K. A. Razumova, V. A. Sannikov, V. A. Sokolov and A. V. Shmatov, *Soviet Journal of Plasma Physics*, **2** (1976) 212
- 2 R. Q. Twiss, "Radiation transfer and the possibility of negative absorption in radio astronomy," *Australian Journal of Physics*, **11** (Dec. 1958) 564-579
- 3 J. Schenkel, "Stimulated emission of radiation by relativistic electrons in a magnetic field," *Physical Review Letters*, **2** (June 15, 1959) 501-505
- 4 V. V. Gaponov, "Interaction of attachment electron beams with electrostatic helix waves in transmissiom tubes," *Izv. VUZ Radiofizika*, **2** (1959) 450-462
- 5 J. E. Hirschfeld and J. M. Wachtel, "Electron cyclotron maser," *Physical Review Letters*, **12** (May 11, 1964) 522-526
- 6 V. V. Gaponov, V. I. Gal'denberg, M. I. Petelin and V. K. Yulpatov, "A device for excitation and electron wave generation," *Copyright No. 227931 with priority of Mat. 21, 1967, Official Bulletin KDDO of SMI USSR*, No. 11 (1976) 290
- 7 V. V. Gaponov, M. I. Petelin and V. K. Yulpatov, "The induced radiation of excited classical oscillators and its use in high-frequency electronics," *Radiophysics and Quantum Electronics*, **10** (1967) 794-813
- 8 G. S. Nusimovich and R. E. Elm, "Efficiency of a CRM resonator with a longitudinal Gaussian distribution of high frequency fields," *Elektronika i Tekhnika, ser. 1, Elektronika SVCh*, **8** (1972) 55-60
- 9 H. R. Jory, S. Evans, J. Moran, J. Shively, D. Stone and G. Thomas, *IEDM Technical Digest* (Dec. 1990) 301
- 10 H. R. Jory, R. Herz, S. Evans, K. Feich, L. Fox, H. Huey, J. Shively and S. Spang, *IEDM Technical Digest* (Dec. 1993) (to be published)
- 11 J. Tancredi et al., *U.S.D.O.E. Publication CONF-820654, Gyrotron user-developer meeting* (Jul. 1982) 73
- 12 P. Boulanger, P. Charbit, G. Faillon, E. Kammerer and G. Moutier, "Development of gyrotrons at Thomson-CSF," *International Journal of Electronics*, **53**, No. 6 (1982) 523-531.
- 13 T. Kageyama, I. Tsuchiya, Y. Takahashi and H. Sato, *IEDM Technical Digest* (Dec. 1993) (to be published).
- 14 K. Sugimori, K. Fujita, Y. Terumichi, S. Tanaka and T. Idehara, "22-70 GHz gyrotron development," *International Journal of Electronics*, **53**, No. 6 (1982) 533-538.

- 15 V. S. Stetsko. *Proc. Ninth All-Union Conference on Vacuum Tubes and Plasma Physics, Leningrad* 2 (1979) 267.
- 16 V. A. Anisimov, V. A. Il'gus, V. A. Kapustin, V. I. Gol'denshteyn, M. I. Petelin, V. G. L'vov and V. K. Yulpatov. *Irradiated Plasmas* 10 (1974) 265.
- 17 V. I. Zolotarev, T. B. Pankratova, M. I. Petelin and V. A. Il'gus. "Millimeter and submillimeter-wave gyrotrons." *Radio Engineering and Electronic Physics* 19 (May 1974) 103-107.
- 18 V. A. Il'gus and G. S. Smerzhinskii. "Powerful gyrotrons for the structure and strength." *International Journal of Infrared and Millimeter Waves* (1982) (to be published).
- 19 V. Carmel, R. H. Chou, M. Reed, V. K. Kapustin, D. Diabate, R. Serfaty, J. S. Levine and V. I. Gol'denshteyn. "Regulation of a stable and highly efficient gyrotube for controlled fusion research." *Physical Review Letters* 30 (October 10, 1982) 117-119.
- 20 K. E. Kravich, J. H. Schuckler, R. J. Temkin and W. J. Mulligan. "High efficiency operation of a 100-GHz pulsed gyrotron." *Conference Digest, Eighth International Conference on Infrared and Millimeter Waves, Miami Beach, Florida* (Dec. 1982) W1-1.
- 21 D. V. Kiselev, G. S. Kostylev, V. G. Novitsky, M. I. Petelin and S. Ye. Tsirul'nik. "An experimental study of a gyrotron operating at the second harmonic of the cyclotron frequency with optimized distribution of the high-frequency field." *Radio Engineering and Electronic Physics* 19 (Apr. 1974) 97-100.
- 22 V. I. Zapevalov, S. V. Malugin and S. E. Tsirul'nik. *Abstracts Reports of the Ninth All-Union Conference on Microwave Electronics, Kiev* 1 (1979) 100.
- 23 V. I. Zapevalov, S. V. Malugin and I. A. Sushakov. *Conference Digest, Reports of the Ninth All-Union Conference on Microwave Electronics, Kiev* 1 (Sept. 1981) 194.
- 24 J. D. Silverstein, R. M. Cornwell and M. I. Reed. "New millimeter wave radiation from a gyrotron." *International Journal of Electronics* 33 No. 6 (1982) 529-536.
- 25 Guo He-Zong, Chen Zeng-Guo, Zhang Shi-Chang and Wu De-Shun. "The study of a TE₂ mode gyrotron operating at the second harmonic of the cyclotron frequency." *International Journal of Electronics* 31 (1981) 465.
- 26 J. L. Beverly, B. G. Dault, K. E. Kravich, P. Wochodzinichow, W. J. Mulligan and R. J. Temkin. "Harmonic emission from high frequency gyrotrons." *Conference Digest, Eighth International Conference on Infrared and Millimeter Waves, Miami Beach, Florida* (Dec. 1982) Th1-5.

- 27 R. J. Temkin, R. L. Kirschner, W. J. Mulligan, P. Marate and H. H. Petterman. 'A 100 kW 100 GHz pulsed gyatron.' *International Journal of Infrared and Millimeter Waves*, 2, No. 1 (1982) 127-137
- 28 R. Fick, D. Stone, H. Jody, H. Castro, C. Wendell, R. J. Temkin, and R. L. Kirschner. 'Design and operation of megawatt gyrotron guide for a 100 GHz gyatron.' *IEEE Technical Digest* 34-3 (1982) 262
- 29 J. L. Blackfield. 'A cyclotron radiation source.' *Condenser Digest, English, International Conference on Infrared and Millimeter Waves Miami Beach, Florida (Dec. 1982)* 111-11
- 30 J. L. Blackfield. *International Journal of Infrared and Millimeter Waves*, 2 (1983) 639
- 31 V. V. Litvinov and L. R. Kirschner. 'A new megawatt field gyatron - gyrotrigatron.' *International Journal of Infrared*, 33, No. 6 (1982) 4592-4596
- 32 D. H. McWhorter, V. K. Lukatskiy, J. and H. S. Farkas. 'Operation of a high frequency gyatron.' *Condenser Digest, English, International Conference on Infrared and Millimeter Waves Miami Beach, Florida (Dec. 1982)* 111-3
- 33 C. Hiles and V. H. Rumball. *Electromagnetic Vibrations, Waves, and Radiations, The MIT Press, Cambridge, MA (1977)* 311-315
- 34 C. F. Bueck. 'Cyclotron of electron cyclotron waves on a gyrotron.' *American Journal of Physics*, 30, No. 2 (Mar. 1962) 234-236
- 35 E. S. Weibel. 'Spontaneously growing transverse waves in a plasma due to an anisotropic velocity distribution.' *Physical Review Letters*, 2 (February 1, 1959) 83-84
- 36 R. R. Chu and J. L. Blackfield. 'Comparative study of the wave and particle bunching mechanisms in gyrotrons and in a forward propagator.' *Physical Fluids*, 21, No. 2 (Mar. 1978) 311-314
- 37 J. L. Blackfield, J. R. Densmore and J. M. Wozniak. 'Microwave resonator in operation of milliwatt wave energetic electrons.' *IEEE Journal of Quantum Electronics*, QE-1 (Sept. 1965) 227-235
- 38 V. V. Litvinov and V. K. Lukatskiy. 'Generation of helical electron beams with the electromagnetic field in a waveguide.' *Radio Engineering and Electronic Physics*, 12, No. 1 (Apr. 1967) 362-367
- 39 V. W. Fifer and M. E. Read. 'Use of weakly irregular waveguide theory to calculate eigenfrequencies, Q values, and RF field functions for general millimeter.' *International Journal of Electronics*, 51, No. 1 (1981) 175-184

- 10 S. N. Vlasov, G. M. Zhulin, I. M. Orlova, M. I. Petelin and G. G. Rogacheva. "Irregular waveguides as open resonators." *Radio Engineering and Electronic Physics*, **12**, No. 8 (Aug. 1969) 972-976.
- 11 R. J. Temkin. "Analytic theory of a tapered gyrotron resonator." *International Journal of Infrared and Millimeter Waves*, **2**, No. 4 (1981) 629-650.
- 12 K. R. Chu. "Theory of electron-cyclotron-maser interaction in a cavity at the harmonic frequencies." *Physics of Fluids*, **21**, No. 12 (Dec. 1978) 2354-2364.
- 13 R. J. Temkin, K. E. Kruecher, S. M. Wolfe, D. R. Collin and B. Lax. "High frequency gyrotrons and their applications for Tokamak plasma heating." *Journal of Magnetism and Magnetic Materials*, **11** (1979) 368-371.
- 14 M. I. Petelin and V. K. Yulpatov. "Linear theory of a monotron cyclotron-resonance maser." *Radio Engineering and Electronic Physics*, **18**, No. 2 (Feb. 1975) 212-218.
- 15 V. V. Gagarin, A. I. Ginzburg, D. P. Gritov, T. B. Pankratova, M. I. Petelin and V. A. Evagor. "Experimental investigation of centimeter-band gyrotrons." *Radio Engineering and Electronic Physics*, **18**, No. 2 (Feb. 1975) 201-211.
- 16 K. E. Kruecher and R. J. Temkin. "High-frequency gyrotrons and their application to Tokamak plasma heating." *Infrared and Millimeter Waves, Vol. 7*, K. Hultine, ed., Academic Press, New York (1983) 377-485.
- 17 K. E. Kruecher. "Users manual for Linear, a computer program that calculates the linear characteristics of a gyrotron." *MIT Plasma Fusion Center Report*, Jan. 1982.
- 18 V. A. Evagor, V. V. Gagarin, M. I. Petelin and V. K. Yulpatov. "The gyrotron." *IEEE Transactions on Microwave Theory and Techniques*, **MTT-25**, No. 1, (Jan. 1977) 114-127.
- 19 V. A. Gagarin, V. A. Evagor, A. I. Ginzburg, G. S. Nusinovich, Sh. L. Tsimering, V. R. Tsou and S. N. Vlasov. "Powerful millimeter-wave gyrotrons." *International Journal of Electronics*, **51**, No. 1 (1981) 277-302.
- 20 V. W. Eifer, M. F. Read, K. R. Chu, and R. Serlex. "A self-consistent field theory for gyrotron oscillators: application to a low Q gyromonotron." *International Journal of Electronics*, **53**, No. 6 (1982) 505-521.
- 21 H. R. Fetterman, P. E. Tannenwald, C. D. Parker, J. Melngailis, R. C. Williamson, P. Wozniakowicz, H. C. Pradlaude and W. J. Mulligan. "Real-time spectral analysis of far infrared laser pulses using a SAW dispersive delay line." *Applied Physics Letters*, **34**, No. 2 (January 15, 1979) 123-125.

- 52 P. Woskoboynikow, K. E. Kreischer, W. J. Mulligan and R. J. Temkin. "Bandwidth and frequency pulling of a 140 GHz gyrotron." *Conference Digest, Eighth International Conference on Infrared and Millimeter Waves, Miami Beach, Florida (Dec. 1983)* W1.4.
- 53 M. N. Afsar and K. J. Button. "Precise millimeter-wave measurements of complex refractive index, complex dielectric permittivity and loss tangent of GaAs, Si, SiO₂, Al₂O₃, BeO, Macor, and Glass." *IEEE Transactions on Microwave Theory and Techniques*, **MTT-31**, No. 2 (Feb. 1983) 217-223.
- 54 W. Culshaw and M. V. Anderson, *Proceedings IEEE, Part B, Suppl. 23*, **100** (1962) 820-826.
- 55 G. S. Nusinovich. "Mode interactions in gyrotrons." *International Journal of Electronics*, **51** No. 4 (1981) 457-474.
- 56 K. E. Kreischer, R. J. Temkin, H. R. Fetterman and W. J. Mulligan. "Multi-mode oscillation and mode competition in high frequency gyrotrons." *IEEE Transactions on Microwave Theory and Techniques* (Dec. 1982) (to be published).